The Acceleration and Transport of Electron Populations in Solar Flares

Duncan James Stackhouse, M.Sci.

Astronomy and Astrophysics Group
School of Physics and Astronomy
Kelvin Building
University of Glasgow
Glasgow, G12 8QQ
Scotland, U.K.

Presented for the degree of
Doctor of Philosophy
The University of Glasgow
September 2016

The work presented here is entirely my own work where explicitly indicated. This thesis has not been submitted anywhere else for another degree or qualification.

29th September 2016

To my Mum, Dad, Thomas, Rebekah, Miriam, Gus and Oschi

Abstract

Solar flares are known to accelerate electrons to high energies, resulting in the movement of these particles throughout the Sun's atmosphere. Although this has been known since the middle of the last century, it is still unknown quite how these particles are accelerated, how they are transported and where the energization takes place. This thesis is concerned with these key questions of solar physics, using a mixture of analytical and numerical modelling in conjunction with the valuable diagnostic tool of the X-rays observed by the Reuven-Ramaty High Energy Solar Spectroscopic Imager (RHESSI). First, imaging spectroscopy with RHESSI is shown, focussing on how to infer to the underlying electron distribution producing the X-ray photons and how this can be used to produce more realistic models. Secondly, a model where the region in which the electrons are accelerated, stopped and emit X-rays is the same is presented, driven specifically by observations of such sources by RHESSI. This admits a steady-state kappa distribution solution and it is shown that the relaxation of an originally thermal Maxwellian population of electrons to this final state proceeds as a wavefront in velocity space. Finally, a model which takes account of recent studies showing the extended nature of the acceleration region within the loops of solar flares is considered. For the first time the intrinsic spatial dependencies of acceleration and transport are explicitly studied, showing the importance of accounting for this in future modelling of solar flares.

Contents

List of Tables

List of Figures

Preface

Chapter 1 provides an introduction to the pertinent topics and theory tackled in this thesis: the particle acceleration and transport processes important in solar flares, the interactions of these particles with the solar plasma, the production of X-ray emission (an important diagnostic of the accelerated particle distribution) and a short review of solar flare X-ray observations using the Reuven Ramaty High Energy Solar Spectroscopic Imager (RHESSI).

Chapter 2 presents the imaging spectroscopy of two flares using RHESSI, further to a more in depth description of how RHESSI produces images and performs spectroscopy. The events studied are chosen for different purposes. Flare 1 is an example of the scenario modelled in Chapter 3, a coronal hard X-ray source where the ambient density is high enough to stop the accelerated electrons in the corona, before they precipitate to the footpoints. Studies of flares such as these have furthermore revealed the acceleration region to be extended and within the loop itself, the effects of which are studied in Chapter 4. The second event considered is an example of the 'standard' flare geometry, with both looptop and footpoint X-ray emission. This flare is chosen due to it being on the limb, thus enabling easy selection and examination of the separate X-ray sources. In addition, the coronal parameters inferred here are used in the numerical model of Chapter 4.

In Chapter 3 a model in which the acceleration of electrons and the region in which they are stopped is essentially cospatial is considered, driven by observations of flares with the morphology of the first flare studied in Chapter 2. This model, with no loss of electrons, is shown to produce a steady-state kappa distribution solution. Kappa

distributions are interesting in a solar flare context as they account for the observed spectral shape with no need for a, possibly artificial, low energy cutoff. Further to this, the relaxation to this form is found to proceed as a 'wavefront' in velocity space. These findings are corroborated by numerical simulations of the governing equation. Of course, the particles cannot be constrained indefinitely, so the solution in the limit of small escape is considered. It is found that this solution is approximately a kappa distribution up to some critical escape velocity, after which escape dominates.

Chapter 4 studies the effect of including the intrinsic spatial dependencies of acceleration and transport when modelling solar flares. While observations have revealed the acceleration region to be extended and within the loop itself, the effects on the resulting electron distribution have yet to be taken account of in the modelling. For the first time a model is presented which *explicitly* deals with the effects of the extended nature of the acceleration region on the acceleration and transport of electrons. Solved numerically, the results are compared to the commonly used leaky-box Fokker-Planck solution showing clearly the differences in resulting spectra. The importance of including these spatial dependencies in future models is shown to be paramount.

Finally, Chapter 5 provides conclusions, discussion and final remarks of the work of the thesis as a whole, where the results are placed in context of present solar flare knowledge. Throughout this thesis CGS units will be used unless otherwise stated.

Acknowledgements

First, I must acknowledge the man who has 'dragged' me (only semi-joking) through these last 4 years. Thank you Eduard P. Kontar.

I must also acknowledge the fact that a lot of this thesis has been published, or will soon be published, and for that I thank my co-authors Gordon Emslie and Nic Bian (as well as Eduard again). I want to thank Brian R. Dennis, both for wonderful insight on RHESSI and for saving me when I hit my head. Alec MacKinnon, for all the times you made me believe I might just be okay at this. Hamish Reid and Paulo Simões, without whom I would never have gotten past a multitude of coding problems. I want to mention you, Dave Wabjwrr and Alex Russell, for making me realise academics weren't scary. I must also thank my internal and external examiners, Declan Diver and Silvia Dalla, for their helpful insights into improvements within the text.

I want to thank my grandparents, Isobel and Frank, Betty and Brian.

For being the Jake to my Finn, the JD to my Turk, the Abed to my Troy, the Charlie to my Mac, the Jon to my Kenny, or vice versa to any depending on the day, I want to express my sincerest gratitude to Jack Carlyle. Thank you Gooch, for being an excellent Gooch. Paul Slevin, who somehow managed to be both the best and worst flatmate one could hope for. Fraser Garrow, Katy Howkins (Scott), Laura Stewart (Carr), Marcus Brown, Leigh Duncan, Sam Burton, Sam White, Grafne Munn, Farman Ali and Andres Vales, for always being there. Thanks for Chon, Oete Levens. For all the RHESSI, thesis and other stuff, Natasha Jeffrey deserves an award.

Boomstards...you know who you are.

Rachael McLauglin and Ethel Folan, for all the hard work on my behalf.

The whole 6th floor deserves something, especially the myriad inhabitants of 604 and 614. Everybody else at NASA GSFC as well. My sports teams: Lokomotiv Glasgow, Meigle CC, Hillhead CC, Rattray Tennis Club, Kelvin Building football groups... Does pool count? Sheena and Gail? You all, in your own way, staved off the madness. The Stevenson building, thanks for teaching me to lift. Everyone who's ever talked, drank, sung, laughed or messed about with me at a conference or summer school, thanks for making me realise physics was great.

Finally, I'd like to reserve a special mention for Alan Harper, without whom I do not think I would have pushed myself this far.

I love you all, thanks.

Table of Symbols

v, $\mathbf{v}$	Particle speed, velocity [cm s^{-1}]
t	Time [s]
x,y,z	Cartesian coordinates [cm]
θ	Angle between velocity and magnetic field vectors
μ	Particle pitch angle ($\mu = \cos\theta$)
v_{te}	Particle thermal speed [cm s^{-1}] (Equation 1.17)
Γ	Collisional parameter [cm^3 s^{-4}] (Equation 1.10)
D_{vv}	Diffusion coefficient in velocity space [cm^2 s^{-3}]
$f(v,x,t)$, $f(\mathbf{v},x,t)$	Particle distribution function (1D [e^- cm^{-4} s], 3D [e^- cm^{-6} s^3])
$\mathbf{B}$	Magnetic field vector [gauss]
$\mathbf{E}$	Electric field vector [statvolt cm^{-1}]
k_{B}	Boltzmann's constant [erg K^{-1}]
T	Temperature [K]
m_e	Electron mass [g]
e	Electron charge [esu]
n_e	Electron plasma density [cm^{-3}]

Chapter 1

Introduction

1.1 The Sun's Atmosphere and Solar Flares

1.1.1 The Solar Atmosphere

The Sun is a G2 type main sequence star. It has an effective temperature of $T_\odot = 5778$ K, a mass, $M_\odot = 1.99 \times 10^{33}$ g, a radius, $R_\odot = 6.96 \times 10^{10}$ cm, and a luminosity, $L_\odot = 3.84 \times 10^{33}$ erg s^{-1} (see e.g. Stix, 2004). Its atmosphere extends outward from the photosphere, through the chromosphere, lower corona, upper corona and eventually the solar wind which extends out to the heliopause, the edge of our solar system. The magnetic field of the Sun, created by its internal motions, controls the movement and energetics of the solar coronal plasma, and as such is seen as the driving force of transient phenomena such as solar flares, coronal mass ejections and filament eruptions. Solar flares, the overall subject of this thesis, are the greatest release of energy in the solar system, producing energies of $10^{31} - 10^{33}$ erg (Emslie et al., 2012). Flares mostly happen within active regions of the Sun, as here the field strength is particularly strong and the magnetic field significantly convoluted. The global puzzle of flares is still highly unresolved, from the large scale magnetic reconnection processes in the active region to the plasma heating occurring, from where the particles are accelerated and the acceleration of the particles themselves to their transport dynamics there are still many unanswered questions. This thesis is concerned with the last two key questions,

the acceleration and transport of solar flare electrons.

The atmosphere of the Sun can be split into three broad constituent parts, the photosphere, the chromosphere and the corona, which eventually transitions into the solar wind at $\sim 3R_{\odot}$. The photosphere is the 'surface' of the sun, that is the layer of atmosphere that is seen without any kind of extra filter. Its temperature ranges from $\sim$ 6000 K to $\sim$ 4000 K at what is known as the temperature minimum region, $T_{\rm min}$. Number densities in the photosphere range from $10^{17} - 10^{15}$ cm^{-3}. The next layer after the temperature minimum region is the chromosphere, where the temperature increases to $\sim$ 10000 K and number densities drop to $\sim 10^{11}$ cm^{-3} at the top boundary with the corona, through a distance of $\sim$ 2000 km. Between the chromosphere and corona is a very thin layer called the transition region where the temperature jumps 2 orders of magnitude and the density drops again. This leaves the corona, which is by far the largest part of the Sun's atmosphere. The corona is governed by the magnetic field, as in general the thermal pressure is much lower than the magnetic pressure here (a low β plasma, see Gary (2001) for a discussion on the variation of the plasma beta in the solar atmosphere). This means that it is highly conductive and controlled by the motions of the magnetic field. The quiet, non-active corona has a temperature of $\sim 1 - 2$ MK with a density of $10^{8} - 10^{9}$ cm^{-3}, the reason for it being so much hotter than the layers of atmosphere below is still an open question (Parnell & De Moortel, 2012). The variation of the electron temperature and density through the solar atmosphere is shown in Figure 1.1. The process behind solar flares is believed to occur in the corona, where there is a release of energy due to reconnection (Sweet, 1969).

1.1.2 Reconnection and Acceleration

Reconnection is the release of stored magnetic energy in the corona (Priest & Forbes, 2000), this results in heating, where the plasma near the reconnecting region generally jumps by an order of magnitude compared to the quiet corona, i.e. $10 - 30$ MK. Furthermore, a portion of released energy (Lin & Hudson (1976) suggested possibly as much as 10 - 50 %, but this is hard to correctly ascertain) results in the acceleration

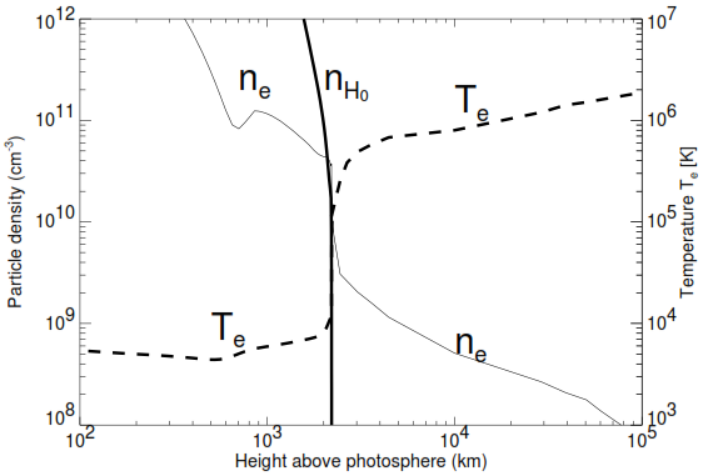

Figure 1.1: The variation of electron density, n_e, hydrogen density, n_{H_0}, and electron temperature, T_e, with height above the photosphere. Figure taken from Aschwanden (2004).

of particles to suprathermal levels, particularly electrons but also protons and heavier ions (see Vilmer et al., 2011, for a recent review). Most flares accelerate particles to the deka-keV range, often to the MeV range and sometimes even to the GeV range (Lin, 2006). This requires an efficient acceleration mechanism which, in a solar flare, could involve DC electric field acceleration, shock acceleration and stochastic acceleration. A review of these methods can be found in Holman et al. (2011). Stochastic acceleration is the favoured method of this thesis, due to the inferred isotropy of the accelerated electron spectrum (Kontar & Brown, 2006) and the fact that in the more realistic DC (Aschwanden, 2002) and shock acceleration models (Jones, 1994) have similarities with the stochastic model. An overview of the three acceleration regimes will be presented later in this chapter (Section 1.2).

As these particles are being accelerated, they will begin to propagate through the atmosphere. Those on open field lines propagate into interplanetary space where they may impact upon the Earth. If the particles are in a region that is closed magnetically then energetic enough electrons will tend make their way to the chromosphere where they are collisionally stopped. In some cases, however, the flaring loop can have an enhanced number density $\sim 10^{11}$ cm^{-3}, possibly due to a process called chromospheric

evaporation, described below. Dense solar loops can cause high energy particles to be stopped in the corona, rather than streaming down towards the lower levels of the solar atmosphere (Jeffrey & Kontar, 2013). This is the subject of the work presented in Chapter 3.

1.1.3 Emission Characteristics of Solar Flares

Solar flares are broadband emitters, producing enhanced emission at wavelengths across the electromagnetic spectrum from radio to X-rays and even gamma-rays in the most high energy events. A flare tends to proceed through three stages, each with certain emissions characteristic within it. First there is the preflare evolution during which there are small scale brightenings in soft X-ray (SXR) and ultraviolet (UV) emission some tens of minutes before the flare. The primary energy release of reconnection occurs during the impulsive phase. This phase lasts from tens of seconds to tens of minutes and is characterized by the emission in hard X-rays (HXRs), gamma-rays, non-thermal (synchrotron) microwaves and white-light continuum emission which are indicative of the strong acceleration of electrons and ions. There are further enhancements in chromospheric line and continuum emission, UV and extreme-UV (EUV) radiation, and bulk plasma upflows in EUV or SXRs at speeds of ~ 100 km s^{-1} coupled with downflows in cooler lines such as Hα (Milligan et al., 2006). Most of this emission is concentrated in the chromosphere. In fact, the dominant radiative energy of a flare, from both thermal and non-thermal particles, occurs in the lower atmosphere (Hudson, 1972), where the emission appears as 'footpoints' in HXR and optical continuum emission and as 'ribbons' in optical line and UV emission, taken to be the chromospheric ends of the magnetic field structure involved in the flare. This is followed by the gradual phase, with its slowly decaying SXR and microwave signatures. Loops and loop arcades appear in SXRs and EUV and appear to grow, filled by chromospheric plasma forced to expand into the corona as the chromosphere is rapidly heated by particles depositing their energy or via thermal conduction, which is known as chromospheric evaporation (Neupert, 1968; Antonucci & Dennis, 1983). Later on, as the corona cools, the loops

and arcades become visible in lower temperature emissions, including EUV and Hα. The gradual phase may last for several hours.

The emission in the paragraph above all occurs within the closed magnetic fields in the lower solar atmosphere. Solar flares also accelerate particles into the solar wind on open field lines. There is evidence for solar energetic particles (SEPs) being accelerated at, or near, the energy release site in flares. Specifically, solar electron events in interplanetary space have a strong association with the metric-decimetric type III radio bursts (see e.g. Lin, 1970) where the high density inferred from the starting frequency of the emission implies the acceleration happens at or near the main energy release site.

The soft X-ray flux present during a flare is used to classify them, specifically that taken by the Geostationary Orbiting Environmental Satellites (GOES) in the 1-8 $\mathring{A}$ flux at 1 AU. There are five broad classes, X-class are the largest, followed in decreasing order by M, C, B and A class flares. There are also subdivisions within the flare classes, via the numbers 1 to 10 (for A to M), such that an M10 class flare has a higher flux than an M5 flare. Each letter stands for a jump in the order of magnitude of flux, an X-class flare has a flux of of order 10^{-4} W m^{-4} (or greater), whereas an M-class flare has a flux an order of magnitude less. X-class flares have no limit on the number associated with them (Fletcher et al., 2011).

X-ray emission in solar flares is produced by bremsstrahlung, either free-free from electrostatic collisions between suprathermal electrons and background particles in the flaring plasma in the case of HXRs (above $\sim$ 10 keV) or from the interactions of particles in a thermal plasma in the case of SXRs. Although X-rays are are only a small portion of the total radiative output during flares (Woods et al., 2006; Kretzschmar, 2011) they offer a valuable diagnostic tool on the accelerated particle distribution. This is because the chromosphere and corona are optically thin to X-radiation and, furthermore, because the emission mostly comes from free-free bremmstrahlung at non-thermal energies. It is thus easier to infer the underlying electron distribution producing the photon spectrum than at other wavelengths where there are multiple emission and absorption mechanisms operating. The advent of spatially resolved HXR imaging with the launch of the Reuven Ramaty High Energy Solar Spectroscopic Im-

ager (RHESSI) in the early 21st century, together with comparison to previous results from Yohkoh, has enabled closer inspection of the electron spectrum (See Chapter 2). In particular, imaging of the coronal looptop source (Xu et al., 2008) has revealed that the acceleration of electrons takes place over a finite, inhomogeneous region of space. This is the subject of Chapter 4.

The remainder of this chapter will discuss acceleration and transport of electrons in solar flares, as well as the emission processes pertinent in the HXR energy range. Finishing with an overview of HXR observations of solar flares.

1.2 Acceleration Processes in Solar Flares

The main aim of this thesis is to examine how the acceleration and transport of electrons in solar flares affects the resulting distribution, and thus photon spectrum, one would expect to obtain. The acceleration that occurs in solar flares can be split in three broad regimes: DC electric field acceleration (Holman, 1985), stochastic acceleration (Petrosian, 2012; Bian et al., 2012) and shock acceleration (Somov & Kosugi, 1997; Tsuneta & Naito, 1998).

The simplest conceptually is electric DC field acceleration but this is hard to apply to solar flares due to the extremely dynamic nature of reconnection (see e.g. Holman, 1985). As the magnetic field during reconnection is constantly changing it would be likely that any current sheets forming would be highly intermittent, both spatially and temporally. Stochastic acceleration (SA) is the net gain of energy due to multiple interactions with waves in a turbulent plasma. Shock acceleration consists of a particular geometry and inhomogeneous boundary that results in the transfer of energy to particles interacting with the shock.

It should be said that in reality there will not be such a clear boundary between the three regimes. The fragmented, inhomogeneous current sheets and magnetic islands of the bursty reconnection mode (Priest, 1985; Aschwanden, 2002) approach the limit of the turbulence required in the stochastic model. Furthermore, many shock acceleration models require multiple crossings of the inhomogeneous boundary in order to produce

efficient acceleration, again approaching the stochastic model due to the diffusive element present here (Jones, 1994).

Further to this, the accelerated electron distribution appears to be isotropic in pitch-angle (Kontar & Brown, 2006) which also favours acceleration by stochastic interactions. This thesis, therefore, presents energization of electrons by stochastic processes. The next two sections will briefly summarise the two other acceleration processes, highlighting where the similarities to SA arise, followed by a third section on SA itself.

1.2.1 Electric DC Field Acceleration

Particle acceleration occurring due to direct current (DC) can be categorised by whether the electric field is sub- or super-Dreicer. The Dreicer field $E_D = k_B T/e\lambda_c$, where λ_c is the collisional mean free path and the other terms are as in the Table of Symbols, being the field strength required to accelerate an electron to its thermal energy over a distance equal to the collisional mean free path. Acceleration can also be categorised by the temporal variability of the field or the magnetic geometry (current sheets, X-points, O-points).

Sub-Dreicer electric field acceleration has been studied in a solar flare context by Holman (1985) and Benka & Holman (1994) and has been shown to fit the velocity distribution of electrons inferred from flares. However, there are problems intrinsic within the model, the major one being the requirement for a large scale electric field the size of the flaring loops. If there were a large Sweet-Parker current sheet ($L \sim 10^9$ cm) this would be unstable to the tearing mode and fragment into magnetic islands in a bursty reconnection mode, which starts to resemble the turbulence required for stochastic acceleration (Kliem, 1994; Miller et al., 1997; Aschwanden, 2002). Furthermore, the observed time of flight delays do not agree with those predicted by models (Aschwanden, 1996). Finally, static electric fields require counter streaming return currents (e.g. opposite to the electron beam) which limits acceleration efficiency (Brown & Melrose, 1977).

Super-Dreicer fields, on the other hand, can produce the observed HXR energies over

much shorter distances, and so seem more suited to a solar flare context. Particles can be accelerated to the required energies in fragmented current sheets or in coalescing magnetic islands as they occur in a bursty reconnection mode. The compactness of the regions in this case does agree with time of flight delays (Aschwanden, 1996). Particle acceleration kinematics in current sheets with super-Dreicer fields can be found in Litvinenko (1996).

DC acceleration can be further categorised by the magnetic field topology, with acceleration near magnetic X-points having been discussed extensively (e.g. Petkaki & MacKinnon, 1997; Hannah et al., 2002; Petkaki & MacKinnon, 2007), or near magnetic O-points or magnetic islands, as discussed by Furth et al. (1963); Spicer (1977), which form naturally due to the tearing instability although the second case would likely require a preaccelerated seed population (possibly by a sub-Dreicer current sheet). Particle acceleration in three-dimensional reconnecting current sheets has been studied by Litvinenko (1996); Zharkova & Gordovskyy (2005); Wood & Neukirch (2005). Recent models have furthermore used more complicated magnetic topologies, involving more advanced MHD models of fan and spine reconnection (Priest & Titov, 1996), with particle acceleration in the presence of spine reconnection studied in Dalla & Browning (2005, 2006) and fan reconnection dealt with in Dalla & Browning (2008).

Of course, any model which relies on a static electric field cannot be considered a realistic one in a solar flare due to their highly dynamic nature. During a flare, electric DC fields are likely to be created by a number of dynamic processes. This includes: (1) Betatron acceleration; which has been applied to solar flares by Brown & Hoyng (1975), where the research was driven by quasiperiodic time structures in HXRs. An example of betatron acceleration is magnetic pumping. (2) Field aligned electric potential drops; such as the model in Tsuneta (1995), where fast reconnection outflows interact with flare loops that are enhanced by chromospheric evaporation resulting in strong shear flows at the interface of the soft X-ray loop and potential drops of $\sim$ 100 keV. (3) Coalescence and X-point collapse; such as that in Kliem et al. (2000), demonstrating that tearing and coalescence in the bursty reconnection mode can modulate particle acceleration on the timescales observed in solar flares.

1.2.2 Shock Acceleration

Ever since shocks have been shown, in a simple configuration, to produce power-law spectra (see e.g. Cargill, 1991) they have been used to explain a variety of astrophysical phenomena. A shock forms in the presence of a discontinuous boundary. Such boundaries are ubiquitous in an astrophysical context, whether at the expanding spherical front of a supernova, the bow shocks of planetary magnetic fields or coronal mass ejections. It would seem natural for the relaxing magnetic fields after reconnection to offer a prime opportunity for such boundaries to occur. Observations of type II radio bursts confirm the presence of shocks in solar flares (Holman & Pesses, 1983) but the particles producing this radiation are streaming out into the solar wind. It would make sense for the magnetic reconnection process to cause standing fast-mode and slow-mode shocks downwards as well as outwards, but at present there is only indirect evidence for this type of downward shock (see e.g. Sui & Holman, 2003).

A shock is a discontinuity that travels faster than the sound (or fast/slow magnetosonic) speed of the ambient medium. Particle acceleration by shock waves can either proceed via a single interaction with the shock (shock-drift acceleration, Fermi, 1949) or by multiple interactions with the shock (diffusive shock acceleration, Anastasiadis & Vlahos, 1991, 1994). Fermi (1949) explained the acceleration of cosmic rays by reflections on moving magnetic clouds. This is valid when a particle encounters a moving boundary with a higher magnetic field, as magnetic mirroring then takes effect. If the electrons only encounter the shock once, then the energy gain is limited by the ratio of the magnetic field up- and downstream of the shock. Higher energies can be obtained if there exists a trapping region upstream of the shock, so that particles get mirrored more than once gaining energy each time. Shock-drift acceleration is most efficient in the presence of a near perpendicular shock (fast shock) but the small angle in this case means that only a few particles ($< 1\%$) can be accelerated (Wu, 1984). This may be too restrictive a regime in a solar flare context, as mentioned by Miller et al. (1997), but is well suited to acceleration in the Earth's bow shock (Jokipii, 1966) and radio type II bursts (Holman & Pesses, 1983). It has been shown, via recent studies by

Warmuth et al. (2009); Park et al. (2012); Vandas & Karlický (2016), that shock-drift acceleration in the presence of a termination shock (fast magneto-sonic shock) in solar flares can reproduce the observed electon spectra up to $\sim$ 100 keV. Furthermore, if the particles were pre-accelerated to $\sim$ 100 keV and injected into the shock, shock-drift acceleration can produce gamma-ray electrons and ions with energies of 100 MeV (Ellison & Ramaty, 1985; Mann et al., 2006).

The main problem with shock-drift acceleration is the limited energy a particle can gain during a single interaction with the shock. If the acceleration happens in an inhomogeneous medium, so that a particle is scattered multiple times back and forth across the shock front this can result in a much greater energy gain during the many interactions with the shock. The basic concept of Fermi acceleration is that in the presence of multiple scattering centres moving in random directions where particles on average gain more energy than they lose results in a net energy gain. A similar effect can be seen in the presence of multiple shock fronts (Anastasiadis & Vlahos, 1991). In fact, the mathematics governing both stochastic acceleration and diffusive shock acceleration is very similar (as discussed in Jones, 1994). Wave particle interactions in diffusive shocks have been studied by Decker & Vlahos (1986); Decker (1988). Two important problems identified are that diffusive shock acceleration of electrons would require a pre-accelerated population at around $\sim$ 20 keV (Guo et al., 2014), meaning that there would need to be some other mechanism operating first to produce the non-thermal seed particles (the so-called injection problem), and, further, it requires the generation of resonant waves (turbulence) up- and downstream of the shock. This has meant that although often used in studying the acceleration of interplanetary particles it has not often been applied to solar flares (Anastasiadis, 2002). Simulations of ions in diffusive shocks during solar flares has, however, confirmed that they can overcome this injection problem, and produce the required resonant turbulence, meaning they are quickly accelerated to gamma-ray energies Cargill et al. (1988).

In a solar flare context shock acceleration could occur in reconnection outflows (LaRosa et al., 1994, 1996; Somov & Kosugi, 1997; Tsuneta & Naito, 1998; Warmuth et al., 2007, 2009; Park et al., 2012) and chromospheric evaporation fronts (Bai et al., 1983). For a

more thorough description of shock and electric DC field acceleration see Aschwanden (2004, Chapter 11).

1.2.3 Stochastic Acceleration

In this section the favoured acceleration process in this thesis, stochastic acceleration, is presented. Whereas electric field acceleration is inherently a DC process, stochastic acceleration is an AC process. Stochastic acceleration occurs via the magnetic field component of low-frequency magneto-acoustic waves (Miller et al., 1997; Schlickeiser & Miller, 1998; Petrosian et al., 2006; Zharkova et al., 2011), from either plasma wave turbulence (Hamilton & Petrosian, 1992; Pryadko & Petrosian, 1997) or cascading MHD turbulence (Miller et al., 1996). Of course, because of the AC nature of the field, the particles can lose energy as well as gain it in their interactions with the waves. However, some areas of the particle distribution will experience a net energy gain, at the expense of the resonant wave energies, and stochastic acceleration occurs. The theory of wave-particle interactions (Melrose, 1980a,b) can describe the growth of magneto-acoustic waves by the absorption of unstable particle distribution energies and concurrently the stochastic acceleration of particle distributions due to resonance with these waves. As discussed above, in a solar flare context stochastic acceleration avoids some of the large scale electrodynamic issues associated with systematic acceleration regimes (Emslie & Henoux, 1995) with the isotropic nature of the accelerated distribution also suggesting acceleration by stochastic measures (Kontar & Brown, 2006). A sketch of a reconnecting loop producing plasma turbulence is shown in Figure 1.2.

In order to fully describe the interaction of particles with waves in a plasma, the theory of wave-particle interactions must be used. This consists of a pair of coupled equations which describes the changes in the wave photon spectrum, $N(\mathbf{k}, t)$, due to interactions with particles and equivalently the changes in the particle distribution function, $f(\mathbf{v}, t)$ (see Table of Symbols), in reaction to the waves (see e.g. Aschwanden, 2004, Chapter 11),

$$\frac{\partial N(\mathbf{k})}{\partial t} + \mathbf{v}_g(\mathbf{k})\frac{\partial N(\mathbf{k})}{\partial \mathbf{r}} = \Gamma(\mathbf{k}, f[\mathbf{v}])N(\mathbf{k}) - \Gamma_{\rm coll}(\mathbf{k})N(\mathbf{k}), \quad \text{and} \tag{1.1}$$

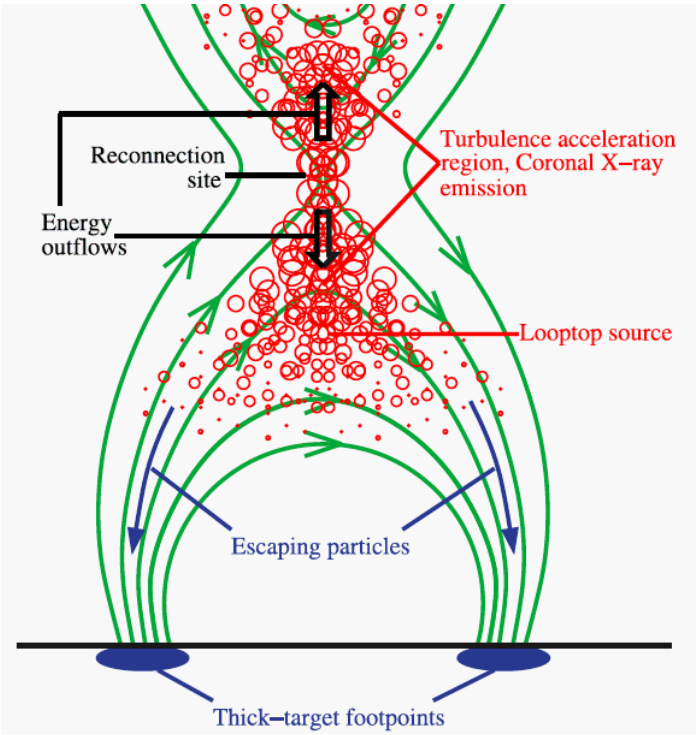

Figure 1.2: A sketch of the stochastic model (e.g. Hamilton & Petrosian, 1992), the green lines show a 'reconnecting' magnetic field and the red circles represent the turbulence. Figure from Liu et al. (2008).

$$\frac{\partial f(\mathbf{v})}{\partial t} + \mathbf{v}\frac{\partial f(\mathbf{v})}{\partial \mathbf{r}} = \frac{\partial}{\partial v_j}\left[D_{ij}(N[\mathbf{k}])\frac{\partial f(\mathbf{v})}{\partial v_i}\right], \tag{1.2}$$

where $N(\mathbf{k})/\hbar\omega$ ($\hbar = h/2\pi$) represents the occupation number of photons in the wave energy range $W(\mathbf{k})$ in $\mathbf{k}$-space, $\mathbf{k}$ being the wavenumber. The position vector is $\mathbf{r}$, $\mathbf{v}_g$ is the group velocity of the emitted waves, $\Gamma(\mathbf{k}, f[\mathbf{v}])$ the wave amplification growth rate, $\Gamma_{\rm coll}(\mathbf{k})$ is the wave damping rate due to collisions and $D_{ij}(N[\mathbf{k}])$ is the diffusion tensor. The coupling between equations (1.1) and (1.2) comes from the wave spectrum growth rate, $\Gamma(\mathbf{k}, f[\mathbf{v}])$, which depends upon the particle distribution and the diffusion tensor, $D_{ij}(N[\mathbf{k}])$, which depends upon the wave spectrum.

The particle distribution (and equivalently the wave spectrum) can therefore only be described fully by the simultaneous solution of these equations. Simultaneous numerical solutions of the one-dimensional, quasilinear form of the above equations of can be found in Hannah & Kontar (2011) and Ratcliffe et al. (2012). To examine the diffusion

of electrons equation (1.1) is neglected. If the particle transport term is also ignored for the moment, then the acceleration of particles is controlled by the quasi-linear diffusion term which characterises the diffusion of wave-resonant particles in velocity space,

$$\frac{\partial f(\mathbf{v})}{\partial t} = \frac{\partial}{\partial v_j}\left[D_{ij}(N[\mathbf{k}])\frac{\partial f(\mathbf{v})}{\partial v_i}\right]. \tag{1.3}$$

The diffusion tensor, $D_{ij}(\mathbf{v})$, includes transitions of the photon distribution, $N(\mathbf{k})$, from momentum $\hbar k_i$ to $\hbar k_j$. The full expression can be found in Melrose (1969).
As the particle is undergoing gyromotion the above equation is best expressed in spherical polar coordinates and so, concentrating on the stochastic acceleration of particles, the diffusion equation is expressed (Petrosian, 2012),

$$\begin{aligned}\frac{\partial f(\mathbf{v},\mu)}{\partial t} = \frac{1}{v^2}\frac{\partial}{\partial v}v^2\left[D_{vv}\frac{\partial f(\mathbf{v},\mu)}{\partial v} + D_{v\mu}\frac{\partial f(\mathbf{v},\mu)}{\partial \mu}\right] \\ + \frac{\partial}{\partial \mu}\left[D_{\mu\mu}\frac{\partial f(\mathbf{v},\mu)}{\partial \mu} + D_{\mu v}\frac{\partial f(\mathbf{v},v)}{\partial v}\right].\end{aligned} \tag{1.4}$$

This equation describes the production of energetic particles from a relatively cool background plasma, thermal or Maxwellian. Here the mean diffusion coefficients are D_{vv}, $D_{\mu\mu}$ and $D_{\mu v} = D_{v\mu}$ and all other terms are as in Table of Symbols. If, as observed (Kontar & Brown, 2006), the distribution is isotropic in pitch angle, the acceleration of electrons is purely controlled by the diffusion in velocity and so,

$$\frac{\partial f(\mathbf{v})}{\partial t} = \frac{1}{v^2}\frac{\partial}{\partial v}v^2 D_{vv}\frac{\partial f}{\partial v}. \tag{1.5}$$

Some form of this equation will be used as the acceleration term within this thesis. This proceeds to change the distribution function on a timescale,

$$\tau_{\rm acc}(v) \sim \frac{v^2}{D_{vv}}, \tag{1.6}$$

so the timescale the acceleration within the system operates on will depend on the exact form of D_{vv}. This timescale in solar flares is of the order 0.1 seconds (Miller et al., 1997). Forms of D_{vv} vary depending on the acceleration method (Bian et al., 2012). SA has a number of advantages over large scale DC electric field acceleration. First, the acceleration occurs on a microscopic scale but averages out over large scales,

this means that there is no problem with return current, which in the DC model require filamentation of the acceleration region (Emslie & Henoux, 1995). Second, gamma-ray energies are easily achieved by SA whereas due to return current losses sub-Dreicer acceleration can only produce energies up to $\sim$ 100 keV (Benka & Holman, 1994). Finally, SA can explain the observed enhancements of heavy-ion abundances in solar flares (Miller & Reames, 1996), for which there exists no explanation in DC field acceleration. In fact, the helical turbulence model of Fleishman & Toptygin (2013) accounts for many of the outstanding questions about particle acceleration in flares, such as the aforementioned ion abundance and the formation of electron beams. The main limitation of SA is the need to presume an ad-hoc injection of the of the necessary plasma or MHD waves (Zharkova et al., 2011).

The observational evidence for SA in flares comes from the changes in loop width with energy, which could signal the presence of magnetic turbulence (Kontar et al., 2011a; Bian et al., 2011). Further to this, the observed soft-hard-soft nature of many flares (Battaglia & Benz, 2007) would naturally be accounted for via SA, where the non-thermal population 'grows' out of the thermal population. In addition, the time constant differential electron flux pivot point (which leads to the soft-hard-soft behaviour) has been used as evidence of SA (Grigis & Benz, 2006).

1.3 Particle Interactions and Transport in the Solar Atmosphere

1.3.1 Coulomb Collisions

In any model of a solar flare collisions will have to play a part, as they are responsible for the emission of HXR photons.

In a fully, or partially, ionised plasma (i.e. the corona or chromosphere) electrons and ions interact via the Coulomb electrostatic force. A moving electron passing another electron or ion will be deflected by an angle θ_D because of the electric field of the other particle. The simplest such scenario is the Lorentz model, where an electron is moving

through a 'sea' of background heavy ions, which are assumed to be stationary. The electrons that are required for charge neutrality are neglected, as the Lorentz model assumes a high atomic number, Z, and hence electron-ion interactions are dominant over electron-electron interactions. The cross section, σ_R, for the small angle scatter of moving electron subject to the Coulomb field of a heavy stationary ion is given by the Rutherford formula (e.g. Lifshitz & Pitaevskii, 1981),

$$\sigma_R = \frac{4\pi Z e^2}{m_e^2 v^4} \int_{b_{\min}}^{b_{\max}} \frac{db}{b}, \tag{1.7}$$

where v denotes the speed of an electron [cm s^{-1}] and the other symbols are as shown in the Table of Symbols. The encounter between electron and ion is characterised by the parameter b (see Figure 1.3) which is the closest distance of approach between the two particles. If the electron is not deflected then,

$$\int_{b_{\min}}^{b_{\max}} \frac{db}{b} = \ln \frac{\lambda_D}{b_{\min}} = \ln \Lambda, \tag{1.8}$$

is defined as the Coulomb logarithm. The role of this is to take account of all possible deflections from $b_{\max} = \lambda_D$ down to $b_{\min}$ where λ_D is the Debye length. In a solar flare context this is taken to be $\ln \Lambda \sim 20$ for the corona (this is the value used in simulations in Chapter 3 and 4) as the plasma here is fully ionised.

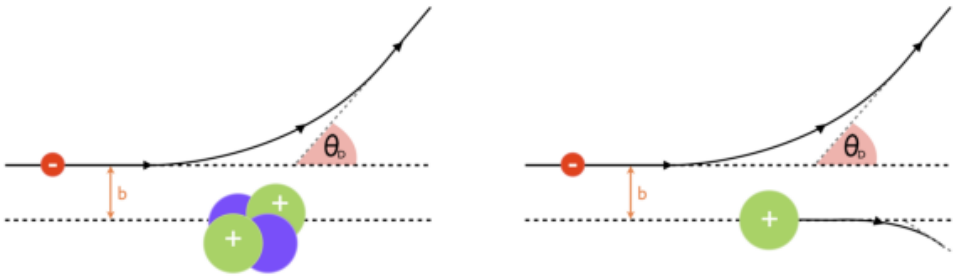

Figure 1.3: *Left Panel* shows an electron being deflected by an ion in the Lorentz model. *Right Panel* shows the general case where both particles are deflected and there is energy and momentum transfer. Figure taken from Jeffrey (2014).

An electron moving with speed v through a field of static heavy ions (of number density n_i [cm^{-3}]) experiences a collisional drag force due to multiple deflections. This causes

the electron to lose energy in the direction of travel on a timescale,

$$\tau_{\rm c} = \frac{1}{n_i v \sigma} = \frac{m_e^2 v^3}{4\pi n_e Z e^2 \ln\Lambda} = \frac{v^3}{\Gamma}, \tag{1.9}$$

where,

$$\Gamma = \frac{4\pi n_e Z e^4 \ln\Lambda}{m_e^2}, \tag{1.10}$$

is the collisional parameter. The collisional deceleration/friction time, $\tau_{\rm c}$, also called the Lorentz collisional time, is the time taken for an electron at speed v to lose all of its energy in the direction of travel. In this model the ions are considered stationary and so there is no exchange of energy during the 'collision.'

The Lorentz model, however, cannot be considered accurate during a solar flare. There will be $e-e$, $e-i$ and $i-i$ collisions. All the particles will be moving and there will be an exchange of energy during every collision. In this case, there are two timescales of interest:

1. The momentum loss time, τ^p, and,
2. The energy exchange time, τ^E.

Physically these two timescales can be thought of as follows. If the background distribution of particles in a solar flare is taken to be Maxwellian then: the momentum loss time is the time taken for a particle's pitch-angle to isotropize in relation to the thermal equilibrium and the energy exchange timescale is the time it takes for the particle to reach an energy equilibrium with the Maxwellian. These timescales differ depending on which particles are interacting, so, for example,

$$\tau^E_{ee} : \tau^E_{ii} : \tau^E_{ei} \sim 1 : \left(\frac{m_i}{m_e}\right)^{1/2} : \left(\frac{m_i}{m_e}\right), \tag{1.11}$$

where m_i [g] is the mass of an ion and the subscripts denote the interaction taking place. So the quickest equilibrium occurs for $e-e$ interactions (Lifshitz & Pitaevskii, 1981). For $e-e$ collisions the energy loss is,

$$\frac{dE}{dt} = -\frac{E}{\tau^E_{ee}} = -\frac{2E}{\tau_{\rm c}} = -\frac{2E\Gamma}{v_e^3} = -\frac{K n_e}{E} v_e, \tag{1.12}$$

where $K = \Gamma m_e^2/2n_e$. Equation (1.12) is often used to describe the energy loss of electrons in solar physics in the *collisional thick-target model* (Sweet, 1969; Brown, 1971). The energy lost by an electron initially at energy E_0 over a distance z is then found by,

$$E^2 = E_0^2 - 2K \int_0^z n(z')dz', \tag{1.13}$$

where the column density is defined,

$$N(z) = \int_0^z n(z')dz'. \tag{1.14}$$

Equations (1.12) and (1.13) are only valid for suprathermal velocities $v \gg v_{\rm te}$. If there was a constant density, n_0, within the target, then $N(z) = n_0 z$, and so a 30 keV electron would be stopped in a distance $\Delta z \sim 0.5''$ in chromospheric densities, $n_0 = 10^{13}$ cm^{-3}. In a overdense coronal loop, such as those studied in Chapter 3, the density might be $n_0 \sim 10^{11}$ cm^{-3} which would result in a stopping distance of $\Delta z = 47''$, which helps to explain observations of HXR events with little or no footpoint emission (Xu et al., 2008; Guo et al., 2012; Jeffrey & Kontar, 2013).

In the presence of collisions, an extra term is added to equation (1.4) that accounts for the energy lost by particles, i.e.

$$\frac{\partial f}{\partial t} \propto \frac{1}{v^2}\frac{\partial}{\partial v} v^2 \dot{v}_{\rm loss} f, \tag{1.15}$$

where $\dot{v}_{\rm loss}$ describes the velocity change rate. In addition, the other terms involving $D_{v\mu}$ and $D_{\mu\mu}$ in equation (1.4) have an effect. If the distribution is assumed isotropic in pitch-angle, and the background electrons are modelled as a heat bath at a constant temperature, T (see Table of Symbols), an assumption valid in a solar flare context (Jeffrey et al., 2014), then the the changes in the isotropic particle distribution, $f(\mathbf{v}, x)$, are described as such,

$$\frac{\partial f}{\partial t} = \frac{1}{v^2}\frac{\partial}{\partial v}\frac{\Gamma(x) v_{\rm te}^2}{v}\frac{\partial f}{\partial v} + \frac{\Gamma(x)}{v^2}\frac{\partial f}{\partial v}, \tag{1.16}$$

where,

$$v_{\rm te} = \sqrt{\frac{k_{\rm B} T}{m_e}}, \tag{1.17}$$

and $\Gamma(x)$ explicitly shows the dependence of the collisional parameter on the electron number density which may depend on space, x. Coulomb collisions have two effects on the evolution of f. The first term after the equality sign in the above equation describes collisional diffusion and proceeds at a timescale,

$$\tau_{\rm diff} \sim \frac{v^5}{\Gamma(x) v_{\rm te}^2}. \tag{1.18}$$

The second effect arises from the last term, that describes collisional deceleration/friction, and proceeds at the Lorentz time,

$$\tau_{\rm c} \sim \frac{v^3}{\Gamma(x)}. \tag{1.19}$$

1.3.2 Particle Transport

The transport of particles from the acceleration region to the chromosphere can be split into two groups: scatter-free (no pitch-angle scattering) and diffusive (pitch-angle scattering). If the process is free-streaming, the electrons are 'tied' to the field lines and they experience negligible losses as they move through the tenuous corona and so deposit most of their energy in the chromosphere. Here they emit X-rays due to $e-i$ bremsstrahlung and energy is lost mostly through $e-e$ coulomb collisions. This is the basis of the commonly adopted 'footpoint' dominated flare scenario (Peterson & Winckler, 1959; Sweet, 1969; Brown, 1971; Melrose, 1980a,b).

There are many observations that support the 'footpoint' picture, for example Battaglia & Kontar (2012) showed that photons of higher energies are emitted lower in the chromosphere, and that the source size decreases with depth consistent with convergence of the guiding field. Furthermore, the growth of loop length with energy as discussed in Xu et al. (2008), Kontar et al. (2011a) and Guo et al. (2012) is consistent with a model where accelerated electrons are streaming along a a relatively constant density loop without significant pitch-angle scattering.

There is mounting evidence, however, that there should be at least some form of pitch-angle scattering within the transport process: first, there is very little evidence of anisotropy in HXR observations Kontar et al. (2011b); second, albedo diagnostics,

such as those in Kontar & Brown (2006); Dickson & Kontar (2013), and stereoscopic measurements (Kane et al., 1998), show little evidence of strong downward beaming; third, the majority of stochastic acceleration models for flares require strong pitch-angle scattering (Sturrock, 1966; Melrose, 1968; Benz & Smith, 1987; Petrosian & Donaghy, 1999; Petrosian et al., 2006; Bian et al., 2012); fourth, the accelerated electrons will propagate in a turbulent or beam generated media.

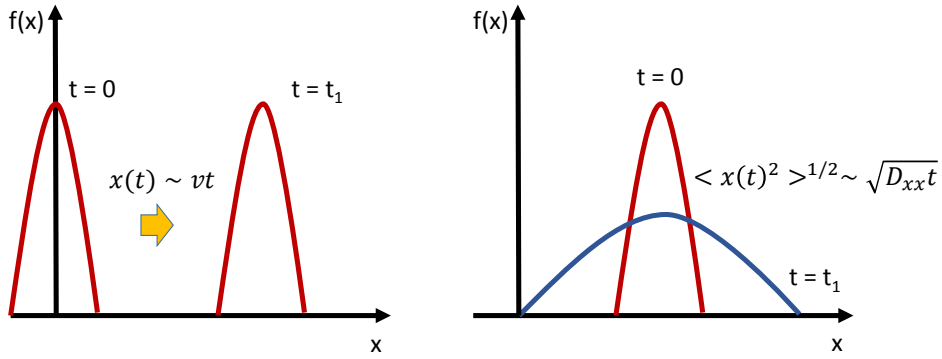

Figure 1.4: *Left Panel* shows scatter free transport in the case where the distribution, f, has constant velocity, v. The distribution is shown at $t = 0$ and at later time, $t = t_1$. *Right Panel* shows diffusive transport parallel to the guiding field, again at times 0 and t_1.

Scatter-Free Transport

Figure 1.4 (left), shows the scatter-free transport case. For a distribution of particles in x-space (all assumed constant velocity here) the act of free-streaming transport will merely move the entire distribution in x-space. If the accelerating currents are field aligned, the electron dynamics can be approximated as 1-dimensional. The acceleration only changes the parallel component of velocity and as such the transport is described by,

$$\frac{\partial f(v,x,t)}{\partial t} = -v\frac{\partial f(v,x,t)}{\partial x}, \tag{1.20}$$

which operates on an associated timescale,

$$\tau_{\rm esc} = \sigma/v, \tag{1.21}$$

where σ [cm] is the size of the acceleration region.

Diffusive Transport

Diffusive transport is shown, for constant velocity, in Figure 1.4 (right panel). Here the change in the distribution between $t = 0$ and $t = t_1$ is purely a diffusion of the distribution in x. In a regime with strong pitch-angle scattering the third term on the right in equation (1.4) becomes important in a transport context. So the transport, in the absence of Coulomb collisions, can be modelled by,

$$\frac{\partial f(\mathbf{v},\mu,x,t)}{\partial t} + \mu v \frac{\partial f(\mathbf{v},\mu,x,t)}{\partial x} = \frac{\partial}{\partial \mu} D_{\mu\mu} \frac{\partial f(\mathbf{v},\mu,x,t)}{\partial \mu}, \tag{1.22}$$

where the movement of the electrons now depends not only on the parallel velocity, v, but also on the particle's pitch-angle, μ. The pitch-angle coefficient is given by,

$$D_{\mu\mu} = D^{(C)}_{\mu\mu} + D^{(T)}_{\mu\mu}, \tag{1.23}$$

consisting of a turbulent, (T), and collisional, (C), part. The collisional diffusion is given by (Karney, 1986),

$$D^{(C)}_{\mu\mu} = \frac{(1+\bar{Z}^2) Kn(x)}{m_{\rm e}^2} \frac{1}{v^3}(1-\mu^2), \tag{1.24}$$

where K is the collisional parameter discussed in the previous Section (1.3.1) and $\bar{Z}^2$ is the mean square atomic number. The factor $(1+\bar{Z}^2)$ takes care of the fact that there are both $e-e$ and $e-i$ collisions. The addition of magnetic fluctuations in the loop, postulated by Galloway et al. (2006) to explain the observed widths of loops observed with the Transition Region and Coronal Explorer (TRACE) and again by Kontar et al. (2011a) and Bian et al. (2011) to explain the observed increase in the width of coronal HXR sources with energy, introduces an extra turbulent term, $D^{(T)}_{\mu\mu}$. The mean free path, parallel to the magnetic field, of a particle undergoing pitch-angle scattering is (e.g. Jokipii, 1966; Schlickeiser, 1989),

$$\lambda \equiv \frac{3v}{8} \int_{-1}^{1} \frac{(1-\mu^2)^2}{D^{(T)}_{\mu\mu}} d\mu. \tag{1.25}$$

The mean free path, λ [cm], could thus have a complicated dependence on energy depending on the spectral energy density of the turbulence.

If pitch-angle scattering is strong enough, i.e. $D_{\mu\mu}^{(T)} \gg 1$, then pitch-angle diffusion leads to a flattening of the distribution in μ over time. That is, there is an isotropization of the distribution, $\partial f/\partial\mu \to 0$. In this limit, the ballistic transport term becomes a spatial diffusion parallel to the field, i.e.

$$\mu v \frac{\partial f}{\partial x} \to -\frac{\partial}{\partial x} D_{\rm xx} \frac{\partial f}{\partial x}, \tag{1.26}$$

where $D_{\rm xx}$ is given by (Jokipii, 1966; Schlickeiser, 1989),

$$D_{\rm xx} = \frac{v^2}{8} \int_{-1}^{1} \frac{(1-\mu^2)^2}{D_{\mu\mu}^{(T)}} d\mu = \frac{\lambda(v) v}{3}. \tag{1.27}$$

In a solar flare context the quantity $D_{\mu\mu}^{(T)}$ is essentially unknown. As such, the mean free path cannot be accurately determined and so the above expression is derived for a constant mean free path in Kontar et al. (2014) and will be used in Chapter 4. The transport is now modelled by a diffusive process,

$$\frac{\partial f(\mathbf{v}, x, t)}{\partial t} = \frac{\partial f}{\partial x} D_{\rm xx} \frac{\partial f(\mathbf{v}, x, t)}{\partial x}, \tag{1.28}$$

where the transport term takes account of the pitch-angle diffusion implicitly. This term has an associated timescale,

$$\tau_{\rm esc} \sim \frac{\sigma^2}{D_{\rm xx}} = \frac{3\sigma^2}{\lambda(v) v}, \tag{1.29}$$

which describes the loss of particles from the acceleration region.

Collisional scattering does produce spatial diffusion of thermal electrons (see discussion of τ^p in Section 1.3.1) but is rather weak when it comes to the transport of non-thermal electrons. This is due to the collisional pitch-angle scattering timescale being approximately the same as the energy loss time (Kontar et al., 2014). So for pitch-angle scattering to be effective it must be shorter than the Coulomb collisional timescale (equation 1.19). The mean free-path must also be small compared to the loop length, i.e. $\lambda \ll L_{\rm loop}$.

The mean free path, λ, will be discussed further in Chapter 4.

1.4 The Effects of Acceleration and Transport

It is important to note that the shape of any distribution forming subject to the above effects, discussed in Sections 1.2, 1.3.1 and 1.3.2, will be dependent on the relative strengths of the terms or, equivalently, the timescales they operate on: acceleration ($\tau_{\rm acc}$, equation 1.6), transport ($\tau_{\rm esc}$, equations 1.21 and 1.29), and collisions ($\tau_{\rm diff}$ and $\tau_{\rm c}$, equations 1.24 and 1.19 respectively).

Thus, with this framework, and with special choices of D_{vv}, the governing equations can be 'tailored' to provide the required electron distribution. In Chapter 3 there is further discussion on how the timescales affect the distribution and in Chapter 4 the velocity dependence of D_{vv} is chosen so as to produce a power-law.

The rest of this chapter will focus on the X-ray emission processes in solar flares, the HXR spectrum being intrinsically linked to the accelerated population of electrons.

1.5 X-ray Emission in Solar Flares

1.5.1 Bremsstrahlung

During a Coulomb collision (Section 1.3.1) there is a small amount of energy emitted by the accelerated electron as a photon. Photons emitted this way are due to the 'braking' of electrons due to the Coulomb electrostatic force and as such are termed *bremmstrahlung* which literally translates as 'braking radiation.' It is by far the greatest contributor to the emission in X-rays during solar flares (Korchak, 1967). A combination of electron-electron and electron-ion bremmstrahlung contributes to the overall radiation from flares but below ~ 300 keV $e-i$ collisions are dominant.

The bremsstrahlung originating from a single electron moving at a non-relativistic velocity produces a total radiated power,

$$P_{\rm rad} = \left(\frac{dE}{dt}\right)_{\rm rad} = \frac{2e^2|\dot{\mathbf{v}}|^2}{3c^2}, \tag{1.30}$$

where $\dot{\mathbf{v}}$ is the electron acceleration and c is the speed of light. This equation is known as Larmor's formula and it gives the energy loss rate of the electron. It must be added

that Larmor's formula is not valid for relativistic electrons. Relativistic effects are ignored here in the interests of illustration. The energy per unit frequency, $dE/d\omega$, emitted the during the time the electron is being accelerated can be found by Parseval's theorem (Longair, 1981),

$$\int_{-\infty}^{\infty} \frac{dE}{dt} dt = \int_{-\infty}^{\infty} \frac{2e^2 |\dot{\mathbf{v}}(\omega)|^2}{3c^2} d\omega = 2 \int_{0}^{\infty} \frac{2e^2 |\dot{\mathbf{v}}(\omega)|^2}{3c^2} d\omega, \tag{1.31}$$

so,

$$I(\omega) = \frac{4e^2}{3c^2} |\dot{\mathbf{v}}(\omega)|^2. \tag{1.32}$$

In a solar flare this will be happening for many electrons at the same time, the general form of the angle-averaged bremsstrahlung flux, $I(\epsilon)$ [photons cm^{-2} s^{-1} keV^{-1}], at the earth ($R = 1$ AU) at a specific time, t, is (Kontar et al., 2011b),

$$I(\epsilon) = \frac{1}{4\pi R^2} \int_{\epsilon}^{\infty} \int_{V} n(\mathbf{r}) F(E, \mathbf{r}) Q(\epsilon, E) dE d^3\mathbf{r}, \tag{1.33}$$

where n [cm^{-3}] is the density of the emitting region, $\mathbf{r}$ is the position on the Sun, V [cm^3] is the emitting volume, $F(E)$ is the electron flux spectrum [electrons cm^{-2} s^{-1} keV^{-1}] and the bremsstrahlung cross-section is $Q(\epsilon, E)$. The full form of the angle averaged $e-i$ bremsstrahlung cross section, $Q(\epsilon, E)$, is shown as equation 3BN of Koch & Motz (1959). Two frequently used analytic approximations in solar physics are the Kramer's cross-section (Kontar et al., 2011b),

$$Q_K = Z^2 \frac{\sigma_0}{\epsilon E}, \tag{1.34}$$

and the more accurate Bethe-Heitler cross section, valid in the non-relativistic limit,

$$Q_{BH} = Q_K \ln \frac{1 + \sqrt{1 - \epsilon/E}}{1 - \sqrt{1 - \epsilon/E}}, \tag{1.35}$$

where $\sigma_0 = (8\alpha/3)(m_e c^2) r_0^2 = 7.9 \times 10^{-25}$ cm^2 keV, $\alpha = 1/137$ is the fine structure constant and $r_0 = 2.82 \times 10^{-13}$ cm is the classical electron radius. Equation (1.33) is an inverse problem, the aim of HXR solar physics is to infer the form of the electron spectrum from the observed photon spectrum. Any form of inferred $F(E)$ is of course dependent on the form of the cross-section used. Both Kramer's and the Bethe-Heitler

cross-sections have been used to infer the electron distributions present in solar flares (Brown, 1971; Brown et al., 2002). Haug (1997) showed that it is important to take relativistic effects into account even at energies as low as ~ 30 keV. The paper presented an analytic form of the Koch & Motz (1959) relativistic Bethe-Heitler cross-section, valid for semi-relativistic energies, and furthermore a more usable form for numerical considerations. It should be noted that in the process of forward-fitting RHESSI spectra performed in this thesis (see Chapter 2) that relativistic effects are taken into account. The fitting routine to the non-thermal spectrum uses the approximation from Haug (1997) together with the multiplicative Elwert correction to the Born approximation (Elwert, 1939). Often the spectrum is sought without spatial information, in this case the spatially integrated form of equation (1.33) can be used,

$$I(\epsilon) = \frac{1}{4\pi R^2} \int_{\epsilon}^{\infty} \langle \bar{n} V \bar{F}(E) \rangle Q(E, \epsilon) dE, \tag{1.36}$$

where $\bar{n} = (1/V) \int_V n(\mathbf{r}) d^3\mathbf{r}$ and $\bar{F}(E) = (1/\bar{n}V) \int_V n(\mathbf{r}) F(E, \mathbf{r}) d^3\mathbf{r}$ is known as the mean electron flux spectrum [electrons cm^{-2} s^{-1} keV^{-1}] (Brown et al., 2003) and has also been called the X-ray emitting electron spectrum (Johns & Lin, 1992). The quantity $\langle \bar{n} V \bar{F}(E) \rangle$ is the density weighted mean electron flux, as $\bar{n}V$ is dimensionless it has the same units as $\bar{F}(E)$. A typical value of $\langle \bar{n} V \bar{F}(E) \rangle$ at 20 keV would be $\sim 10^{55}$ electrons s^{-1} cm^{-2} keV^{-1}.

There are a variety of techniques used to infer $\langle \bar{n} V \bar{F}(E) \rangle$ from the photon spectrum, $I(\epsilon)$. A review of the effectiveness of these techniques is shown in Brown et al. (2006) and this thesis will discuss them further in Chapter 2. Brown et al. (2003) makes the point that $\langle \bar{n} V \bar{F}(E) \rangle$ is the *only* quantity that can be inferred unambiguously, with no additional model assumptions, from the integrated bremsstrahlung emission. It only depends on the form of the bremsstrahlung cross-section chosen. As such, it is the natural middle ground for comparing observations with numerical simulations, as long as the bremsstrahlung cross-section used is the same for both. This thesis will show the $\langle \bar{n} V \bar{F}(E) \rangle$ from two RHESSI HXR events in Chapter 2, which will be used as context for the numerical results of Chapters 3 and 4. These expressions only apply to $e - i$ bremsstrahlung, which is the dominant process at energies less than ~ 300 keV.

Thermal Bremsstrahlung

The emission from a distribution in thermal equilibrium due to bremmstrahlung is called thermal bremsstrahlung. In solar flares, the emission below ~ 30 keV is often best fit with an exponential function that is isothermal in order to obtain an average temperature, T [K], and emission measure, $EM = n^2V$ [cm^{-3}], for the plasma (although due to the extended, and spatially varying, nature of the X-ray sources themselves the actual plasma is bound to have a range of temperatures). The emitting density and volume are given by n [cm^{-3}] and V [cm^3]. The photon flux is given by,

$$I(\epsilon, \mathbf{r}) \propto \frac{n^2(\mathbf{r})V(\mathbf{r})}{\epsilon T^{1/2}(\mathbf{r})} \exp\left(-\frac{\epsilon}{k_{\rm B}T(\mathbf{r})}\right), \tag{1.37}$$

which gives rise to a density weighted mean electron flux for the thermal population (Brown & Emslie, 1988; Battaglia & Kontar, 2013),

$$\langle \bar{n}V\bar{F}(E)\rangle_{\rm th} = EM \frac{2^{3/2}}{(\pi m_{\rm e})^{1/2}} \frac{E}{(k_{\rm B}T)^{3/2}} \, {\rm e}^{-E/k_{\rm B}T}. \tag{1.38}$$

Non-Thermal Bremmstrahlung

In solar physics, the range of electrons at non-thermal energies (above ~ 30 keV) is often best fit by a single or broken power-law (Holman et al., 2003). So in this range of energies the density weighted mean electron flux is also a power-law, i.e.

$$\langle \bar{n}V\bar{F}(E)\rangle_{\rm nth} \propto E^{\delta} \quad \longleftrightarrow \quad I(\epsilon) \propto E^{-\gamma}. \tag{1.39}$$

In the thick-target model of Brown (1971) the spectral index differs from the injected index as $\delta_{\rm thick} = \delta - 2$ and the resulting photon spectrum is $\gamma = \delta + 1$. This would generally be used for dense areas of the atmosphere, i.e. the chromospheric footpoints or an overdense coronal loop.

In this thesis thin-target bremsstrahlung will be used to fit all non-thermal sources to avoid complication because, as mentioned above, the inferred $\langle \bar{n}V\bar{F}(E)\rangle$ will be suitable for the comparison of simulated and observed electron spectra as long as the same bremmstrahlung cross-section is used. In the thin-target model, electrons do not lose

all their energy while moving through the target and $\gamma_{\rm thin} = \delta - 1$. Thus, if the chromospheric footpoints are assumed to be thick-target, and the coronal looptop source is assumed to be thin-target, the spectral index difference would be expected to be 2, if the escaping electron distribution from the looptop is the source of the footpoint emission. Substantial variation from this value has been observed, for example by Battaglia & Benz (2006), which could imply there is some extra trapping mechanism keeping the accelerated electrons in the corona for a longer timescale than free streaming escape. The thin-target density weighted mean electron flux for a single power-law is given by (e.g. Holman et al., 2003, 2011; Simões & Kontar, 2013),

$$\langle \bar{n}V\bar{F}(E)\rangle_{\rm nth} = \langle nVF_0(E)\rangle \frac{\delta - 1}{E_{\rm c}} \left(\frac{E}{E_{\rm c}}\right)^{-\delta}, \; E > E_{\rm c}, \tag{1.40}$$

where $\langle nVF_0(E)\rangle$ [e$^-$ cm^{-2} s^{-1}] is the normalisation flux and $E_{\rm c}$ [keV] is the low energy cutoff.

It should be noted that throughout this thesis the density weighted mean electron flux will also be denoted $\langle nVF(E)\rangle$ without the bars across n and $F(E)$.

1.5.2 X-ray Observations

The temporal evolution of most flares follows a similar pattern as discussed in the introduction (Section 1.1). For X-rays in particular, during the rise, or precursor stage, there is a gradual increase in SXRs and low energy HXRs and the plasma is heated to tens of mega-Kelvin over timescales of minutes. This is followed by the impulsive stage, where there is a fast increase of electrons above 20 keV. This stage only lasts 1-2 minutes and results in a large number of electrons being accelerated to suprathermal levels, the SXR and lower energy HXRs usually peak after the impulsive HXR emission and then start to gradually decrease. The final stage is the gradual decay stage, which encompasses this decrease in X-ray emission and can take hours for some flares, but can be much shorter for others. The timing of each of these phases is different in each event.

The general form of the X- and gamma-ray spectrum encompasses 5 major parts (plus some emission lines), and is mostly caused by bremsstrahlung emission from electron-

ion bremsstrahlung below $\sim$ 300 keV and a mixture of electron-ion and electron-electron bremsstrahlung at energies higher than this (Figure 1.5). The low energy spectrum below $\sim$ 30 keV is often best fit with a single exponential function which gives an average temperature for the flaring plasma, with typical temperatures of $20-30$ MK. Furthermore, there are two emission lines often seen in this part of the X-ray spectrum. One is at 6.7 keV and is due to highly ionised Iron (Fe) and the other at 8.1 keV due to highly ionised Iron and Nickel (Ni) in the corona. These lines are highly sensitive to the temperature and abundance of Iron in the corona and thus serve as useful diagnostic tools (Phillips & Dennis, 2012). The next part is the HXR emission from the non-thermal electron distribution between $\sim 25 - 500$ keV, this is in general best fit by a single or broken power-law and is, for most flares, emitted mainly from the chromosphere, although as mentioned before flares sometimes display HXR emission purely from the coronal source (Jeffrey & Kontar, 2013). Thirdly is the albedo component from Compton backscattered photons from the photosphere (Bai & Ramaty, 1978; Kontar et al., 2006; Jeffrey & Kontar, 2011). Fourth, there is the gamma-ray emission above $\sim$ 500 keV, this part of the spectrum is more complex, combining continuum emission from $e - e$ bremsstrahlung plus line emissions from nuclear reactions. Two prominent emission lines are those at 511 keV due to electron-positron annihilation and one at 2.223 MeV which is the neutron capture line. The fifth part is only seen in rare cases when the spectrum can be observed up to 100 MeV when gamma-ray emission from pion decay may be seen (Ramaty et al., 1979; Vilmer et al., 2011).
The next section will discuss the morphology of solar flares, due to particular features being the drivers of the research in Chapters 3 and 4.

1.5.3 Solar Flare Morphology

A 'typical' solar flare would be expected to have X-ray sources in the corona and chromosphere. Most of the HXR emission is produced in the chromosphere where high energy particles impact on the dense plasma where they are collisionally stopped. For almost all flares, these chromospheric footpoints are observed, consisting mostly of non-

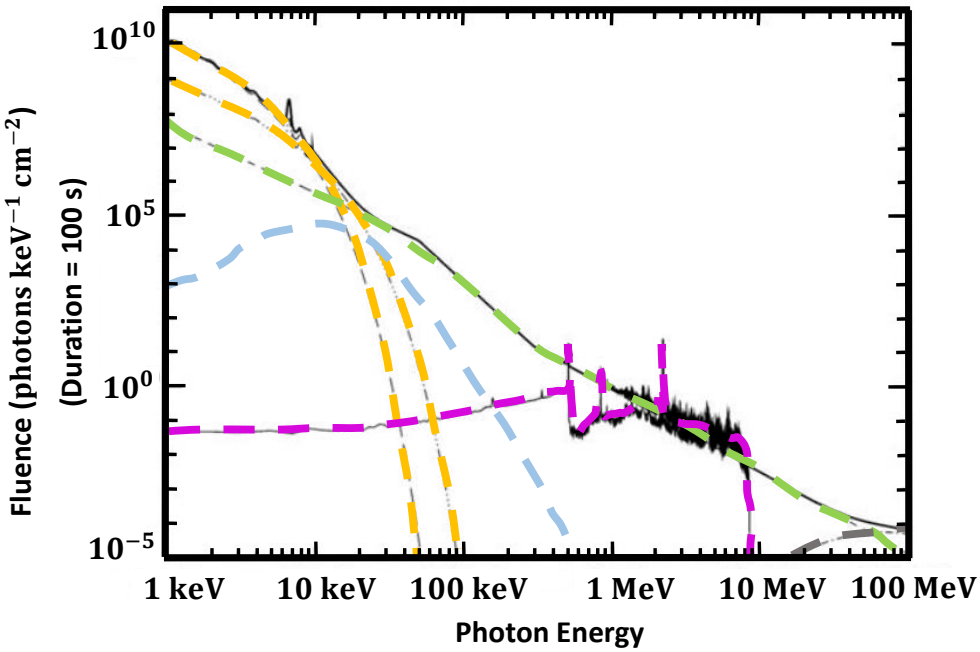

Figure 1.5: Composite RHESSI spectrum. At low energies, less than ~ 25 keV, the superhot flare loop dominates, this is fit in this case by the two isothermal yellow curves on the left. There are two prominent emission lines at 6.7 keV and 8.1 keV. The spectrum between 30 keV to 1 MeV is dominated by bremmstrahlung non-thermal emission (green line). There is also the albedo component (blue line) from Compton backscattered photons. Above 500 keV the gamma-ray spectrum is more complex, with continuum emission from $e - e$ bremmstrahlung and extra line emissions from nuclear interactions (magenta line) and finally the emission from pion decay (grey). Figure taken from Lin et al. (2002) and modified.

thermal emission above $\sim 20 - 30$ keV. The majority of flares are footpoint dominated (Antonucci et al., 1982; Sakao et al., 1996) with most also producing coronal emission that is a mixture of SXR and HXR emission. This is normally a mixture of thermal, thin-target and thick-target bremsstrahlung depending on the specific properties of the coronal flaring region. In most cases this looptop emission can only be observed above the background to around 30 keV, and is assumed to be around the site of the energy release. Flares have been observed with this morphology for a long time, starting with observations from Yohkoh (Kosugi et al., 1991) and continuing with the RHESSI satellite (discussed in Section 1.6 and Chapter 2).

In rare cases, an extra HXR source is observed above the SXR looptop (Masuda et al., 1994), which has been presented as the energy release site. It could be that the current sheet from the reconnection itself is being observed here. One particularly interesting observation of this feature is shown in Sui & Holman (2003). Sometimes the above the looptop source can have very high energies (Krucker & Battaglia, 2014). Observations of these events are rare, however, maybe because they are not a part of every flare's morphology, or perhaps because the resolution of RHESSI is not high enough.

Another rare type of solar flare is the case where the HXR emission is almost entirely confined to the coronal source. These events are often thought of as coronal thick-targets (Veronig & Brown, 2004; Jeffrey & Kontar, 2013) where a high density, $\sim 10^{11}$ cm^{-3}, stops the electrons in the corona before they get the chance to precipitate to the lower atmosphere. These events are important in the context of this thesis, they are the driving force behind the analytic approximations of Chapter 3. Flares such as these give extra information on acceleration after reconnection (Xu et al., 2008), showing that the emission is consistent with an extended acceleration region within the looptop. The extended nature of the acceleration region is the subject of the work in Chapter 4.

There is one very rare type of event for which there exists no coronal emission at all, such as the one studied in Fleishman et al. (2011). In this event electrons are observed above 100 keV but all the emission is confined to the footpoints with a very low temperature. Examples of all these flare morphologies are shown in Figure 1.6.

The length of the coronal source has been shown to vary with energy consistent with a thick-target density within the looptop with densities $\sim 10^{11}$ cm^{-3} (Xu et al., 2008; Guo et al., 2013; Jeffrey & Kontar, 2013). Loop widths have also been observed to increase with energy but this is harder to explain. In a classical sense the electrons should be bound to fieldlines and cross field transport should be negligible. Kontar et al. (2011a) and Bian et al. (2011) suggested that this could be due to magnetic turbulence in the loop. The presence of which is a requirement of the stochastic acceleration model.

During a solar flare, the emission travels outward in all directions, not just directly into the line of sight. Some photons are Compton scattered when they impact on

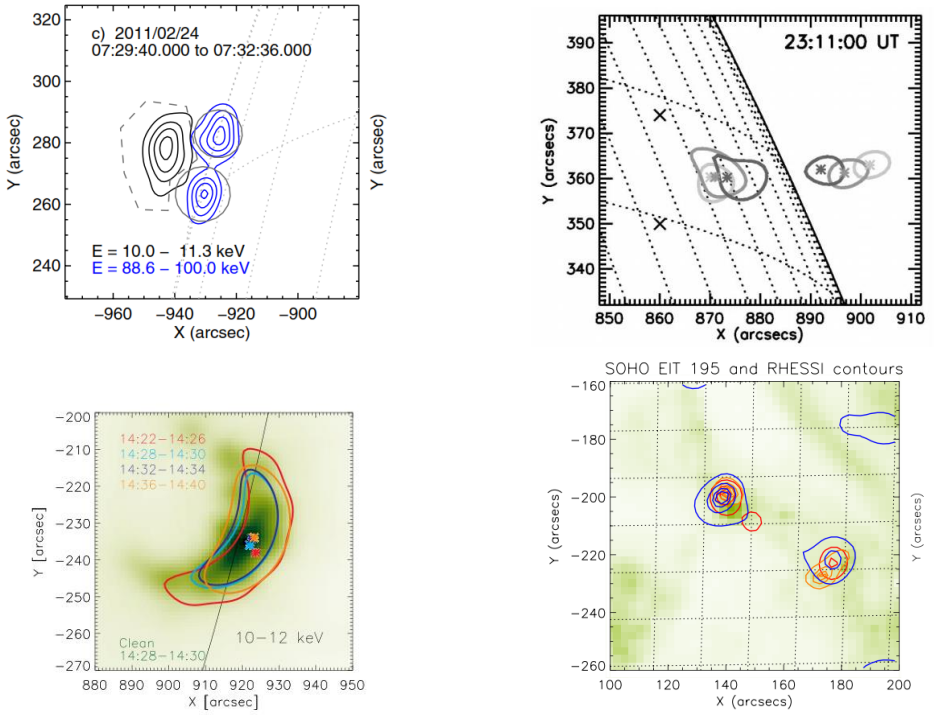

Figure 1.6: *Top Left*; 'Standard' flare geometry, with low energy coronal emission and HXR footpoints, taken from Simões & Kontar (2013). *Top Right*; Flare with above the looptop source, taken from Sui & Holman (2003). *Bottom Left*; Coronal HXR source, figure taken from Jeffrey & Kontar (2013). *Bottom Right*; rare event where only HXR footpoints are observed, figure taken from Fleishman et al. (2011).

the photosphere. This has the effect of a 'bump' in the photon spectrum between $\sim 30 - 50$ keV called the albedo which should be taken account of, especially in full-Sun spectra. The method to account for this is via the Green's function approach of Kontar et al. (2006) which is fully assimilated within the RHESSI spectral analysis software, discussed in the next section and more fully in Chapter 2. Other effects which may need to be accounted for are count pileup on RHESSI detectors (Holman et al., 2011) and wave-particle interactions (Kontar et al., 2011a).

1.6 X-ray Telescopes

Hard X-ray images of solar flares were first conducted via balloon flights such as that in Takakura et al. (1971) via a one dimensional modulation collimator imager. This was followed by the hard X-ray imaging spectrometer (HXIS) (van Beek et al., 1980) on board the Solar Maximum Mission (SMM) which, for the first time, resolved images of footpoint and looptop sources (Hoyng et al., 1981). The Hinotori rotating modulating collimator (RMC) (Tanaka, 1983) introduced rotation modulating collimators as the way to improve spatial resolution of HXRs. The Yohkoh hard X-ray telescope (HXT) (Kosugi et al., 1991) then produced more spatially resolved images, at higher energies, via its RMCs than observed before. The last two missions pioneered the technology that enables RHESSI (Lin et al., 2002), through its nine RMCs, to provide unparalleled resolution of hard X- and gamma-ray photons in space, time and energy.
The driving force for all the work within this thesis are the HXR observations performed by RHESSI. Specifically, dense HXR coronal sources are the driver behind the analytic solution of Chapter 3 and the RHESSI observations of the second flare studied in Chapter 2 provide the input parameters and context to the numerical modelling in Chapter 4. As such, this section is a brief summary of the RHESSI spacecraft.

1.6.1 RHESSI Instrument Overview

The Reuven-Ramaty High Energy Solar Spectroscopic Imager or RHESSI is a NASA-led mission launched in 2002 and still operational today, It observes the full Sun from a low Earth orbit over the energies 3 keV - $\sim$ 17 MeV. It was designed to improve the resolution of X-ray and gamma-ray observations spatially and temporally and to have good energy resolution across the entire range. It consists of 9 cooled germanium detectors at the rear of the spacecraft. In front of these the 9 widely spaced grids at a distance of 1.5 m apart are the RMCs which provide the imaging capabilities. The instrument itself is shown in Figure 1.7. RHESSI has provided spatial resolution not available before, via imaging spectroscopy, discussed in Chapter 2.

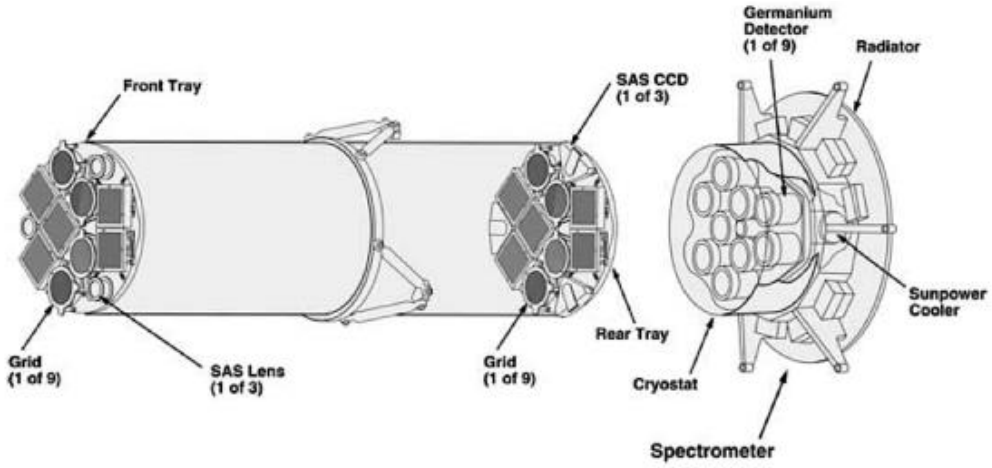

Figure 1.7: The RHESSI instrument, taken from Hurford et al. (2002).

1.6.2 RHESSI Imaging

Due to their high energy X-rays above $\sim$ 1 keV and gamma rays are extraordinarily hard to focus directly. Although the next generation of X-ray imagers, such as *The Nuclear Spectroscopic Telescope Array*, NuSTAR (Harrison et al., 2013; Hannah et al., 2016), and *The Focusing Optics X-ray Solar Imager*, FOXSI (Krucker et al., 2014), are making this a possibility for X-rays below $\sim$ 100 keV. RHESSI, however, needs to make its images via a different technique. It is an indirect Fourier Imager; the spacecraft spins on its axis once every $\sim$ 4 s and during this photons impact upon the RMCs (Hurford et al., 2002). Each incident photon either hits a slit or a slat at one of the RMCs, which either allows or impedes the passage of the photon to the germanium detector, shown in Figure 1.8. This then produces a time modulated signal which depends on the size and position of the source on the Sun (see Chapter 2). If this temporally modulated signal is then stacked per 'roll bin' (fraction of a spacecraft rotation) this gives a set of X-ray visibilities. These visibilities are the two dimensional fourier components of the source in uv-space, given by,

$$V(u,v;\epsilon) = \int_x \int_y I(u,v;\epsilon)\, \mathrm{e}^{2\pi i(xu+yv)}\, dx\, dy, \tag{1.41}$$

the inverse transform of which gives the X-ray image, I, at energy, ϵ, in the xy-plane. The visibilities are represented in uv-space by a series of circles of constant radius

representing the angular resolution of RMC 1-9 with the detectors with less resolution producing smaller circles (e.g. Massone et al., 2009). RMC 1 has the finest grid and RMC 9 has the coarsest grid, with angular resolutions of 2.26" and 183.2" respectively. Each successive RMC has an increase in grid size by a factor $\sqrt{3}$. Doing a two dimensional fourier transform on the time modulated signal produces a back-projection image (Mertz et al., 1986). The straight fourier transform that produces the back-projection image is not ideal though; it gives a poor image with sidelobes. Hence, a number of different algorithms have been developed or modified from radio astronomy in the aim of producing better X-ray images. Some of the most used techniques are CLEAN (Högbom, 1974; Hurford et al., 2002), the Maximum Entropy Method (MEM) (Hurford et al., 2002; Schmahl et al., 2007), Pixon (Pina & Puetter, 1993; Metcalf et al., 1996), uv_smooth (Massone et al., 2009) and forward fitting algorithms such as visibility forward fitting (VisFwdFit) (Hurford et al., 2002; Schmahl et al., 2007). Of these the CLEAN algorithm is used in this thesis, in Chapter 2, chosen due to the best trade off between speed and accuracy. We summarise the five techniques here.

The CLEAN algorithm assumes that the X-ray source is made up of many point sources. CLEAN-ing an image is the process of iteratively finding the highest intensity pixel in the image. At each iteration, once the highest value pixel is found, a chosen proportion of the highest intensity, known as the clean beam width parameter, is convolved with the point spread function (PSF), centered at the highest value pixel and subtracted from the image. This is stopped after a chosen number of iterations, or when the peak flux is negative. The final image is a CLEAN-ed map consisting of the position and amplitude of each chosen pixel convolved with the PSF.

Pixon is a method that has been adapted from the Yohkoh HXT (Metcalf et al., 1996). The algorithm tries to find the simplest model for the image consistent with the data. To do this it uses different sized pixels, or 'pixons', together to try and reproduce the observed modulation patterns and aims for the least number of pixons required to do this. It is generally thought to provide the best photometry but is very slow (can take $\gtrsim$ 1 hour for a 128 by 128 pixel image).

The maximum entropy method differs from Pixon and CLEAN in that it assumes each

pixel on the image is an independent source. The algorithm iteratively searches for that image where the flux in each pixel is constrained by the requirements that the entropy is maximized while maintaining an acceptable χ^2. That is to say that the image is the flattest possible consistent with observations. MEM sometimes suffers from over-resolving images, resulting in too many point-like sources and can have trouble with extended sources (Dennis & Pernak, 2009).

The uv_smooth method uses the fact that the RHESSI RMCs produce Fourier components in a series of circles on the uv-plane. It creates an image by interpolating the visibilities in the uv-plane, followed by reconstructing an image of the source via a fast Fourier transform inversion and reducing the ringing effects (i.e. sidelobes) by imposing a positivity constraint. The second and third steps here are repeated iteratively until a suitable χ^2 criterion is fulfilled.

VisFwdFit starts with the assumption that there are only a limited number of source shapes. The parameters describing each source are then adjusted until the model predicted visibilities provide an acceptable χ^2 fit to the measured visibilities. This offers a fast way of obtaining the source parameters, such as length and width (as well as errors associated with them). Of course, as this is a forward fitting method it relies on the fact that the number and shape of the sources matches reality in order to provide an acceptable fit.

The process of using the CLEAN algorithm will be discussed further in Chapter 2 where the imaging spectroscopy of a flare is undertaken.

1.6.3 RHESSI Spectroscopy

The nine cooled (< 75 K) germanium detectors are what make up the RHESSI spectrometer. Its resolution is less than 1 keV at 3 keV and increases to 5 keV at 5 MeV (Lin et al., 2002). Each detector itself is made up of two segments, front and rear. The front segments can absorb photons up to 250 keV while the rear segments can absorb up to $\sim$ 17 MeV. When photons hit the detectors, they produce a current, which is registered as counts. Thus RHESSI is a count rate spectrometer, the counts are related

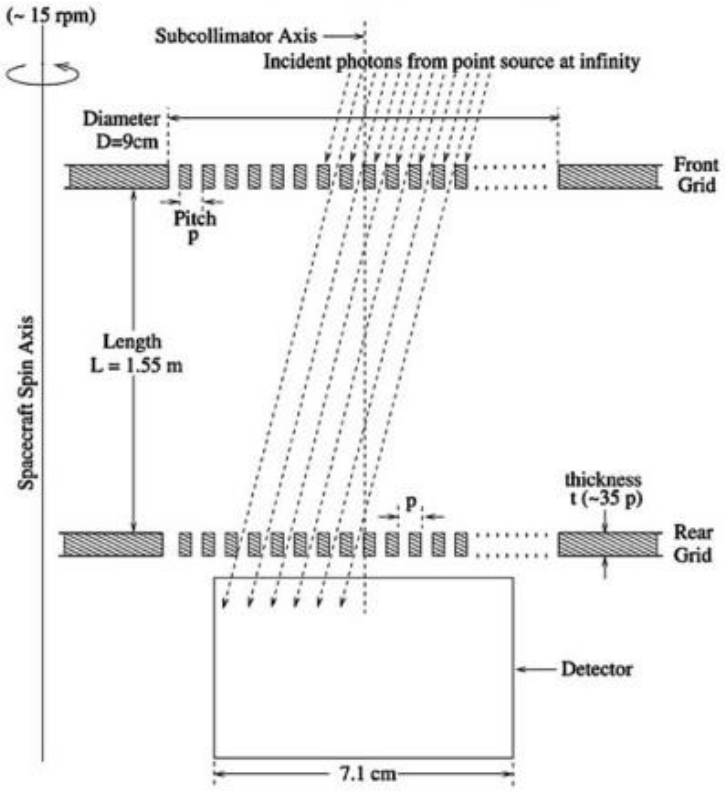

Figure 1.8: How the incident photons are either blocked or allowed through at a given time, depending on their source position. Figure taken from Hurford et al. (2002).

to the X-ray photon spectrum by,

$$\mathbf{C} = \mathbf{B} + \mathbf{SRM}\ \mathbf{I}, \tag{1.42}$$

where **B** is the background counts, **I** is the incident photon rate spectrum, **SRM** is the spectral response matrix and **C** is the count rate spectrum. The spacecraft itself is not shielded and so any contamination from, for example, cosmic-rays needs to be taken account of before spectroscopy is performed. The **SRM** takes account of the many effects that can affect the correct detection of photons. If the effect means that RHESSI cannot detect the photon at the photon's energy then this will be taken into account on the diagonal of the **SRM**, if the effect causes the photon to be detected at an energy other than its own then this contributes to the off-diagonal terms (Smith et al., 2002). Each detector has a pair of 'shutters' (attenuators) in front so as to avoid saturation during high photon count events. There are thus three states: A0; no

shutters, A1; thin-shutters only, and A3; thick and thin shutters. Once the spectrum is obtained it can be analysed in the Object Spectral Executive, OSPEX (see Schwartz et al. (2002) or http://hesperia.gsfc.nasa.gov/rhessidatacenter).

As already mentioned the spectroscopy of two CLEAN images will be shown in the next Chapter (2) together with a more thorough description of imaging and spectroscopy with RHESSI.

Chapter 2

RHESSI Imaging Spectroscopy of Two Flares

Parts of this Chapter can be found in Stackhouse & Kontar (2017)

2.1 Introduction to the Chapter

The HXR observations undertaken by the RHESSI spacecraft from 2002 to the present day are the driving force of the work in this thesis. As mentioned in Lin et al. (2002) the only way to obtain sub arcsecond class images of hard X- and gamma-ray sources is with Fourier type imaging. This was pioneered in the Hinotori rotating modulating collimator (Tanaka, 1983) and Yohkoh Hard X-ray Telescope (HXT) Kosugi et al. (1991). RHESSI provides angular resolutions spaced from 2.3" to $\gtrsim 3$ arcmin allowing sources to be imaged across a large range of spatial scales. In a spacecraft half rotation (2 seconds) the nine RHESSI RMCs measure ~ 1100 Fourier components for a typical source location as compared to 32 Fourier components for the Yohkoh HXT. This means that much more complex flare images can be resolved. Further to this, Yohkoh images were produced with four energy bands, and only up to 100 keV. RHESSI does not transmit a preselected subset of images, the telemetry includes all the information about each detected photon. This means a user can have control of the temporal

resolution, spectral range and resolution, spatial resolution and image quality based on the precise needs of the event studied. In addition, the RHESSI spectrometers provide energy resolution of 1 keV full width half maximum in the hard X-ray energy range (3-100 keV) only achieved before by balloon payloads carrying germanium detectors (Lin & Schwartz, 1987; Smith et al., 2002).

Of particular interest to this thesis are those events in which the HXR emission is confined to the corona, so called thick-target coronal sources (Veronig & Brown, 2004; Jeffrey & Kontar, 2013) due to the fact that the ambient density in the loop is high enough that the electrons are stopped within the corona. This is the particular scenario discussed in the next Chapter (3). Events with this morphology have, in addition, revealed the extended nature of the acceleration region (Xu et al., 2008), the importance of which is studied in Chapter 4. Furthermore, it is possible to gain model parameters from the spectroscopy, or imaging spectroscopy, of solar flares, enabling the use of the inferred temperature, density and acceleration region extent as 'starting' parameters in a numerical model. In this chapter the imaging spectroscopy of two flares illustrating two distinct morphologies of interest in Chapters 3 and 4 is shown.

2.1.1 Past Studies of Solar Flares via RHESSI

The RHESSI spacecraft enabled, for the first time, spatially, temporally and energetically resolved observations of the deka-keV HXR spectrum in solar flares (see Holman et al., 2011; Kontar et al., 2011b, for recent reviews). The imaging spectroscopy capabilities of RHESSI allowed new avenues of investigation, Emslie et al. (2003), Battaglia & Benz (2006) and Petrosian & Chen (2010) used spatially resolved images of looptop and footpoint sources to compare the electron spectrum throughout the HXR source whereas Li & Gan (2005), Liu et al. (2009) and Jeffrey & Kontar (2013) investigated the time dependence of the shape of the looptop sources. Of particular note was the resolution of the acceleration region, showing that to be consistent with observations it must be extended in space (e.g. Xu et al., 2008; Kontar et al., 2011a; Guo et al., 2012).

In an X-ray context the photon spectrum from the looptop has a thermal-like core and a power-law, or broken power-law tail. The footpoint spectrum also has a thermal component, likely with a lower temperature than the looptop source, with a non-thermal tail having a relatively harder spectral index than the coronal spectrum (Emslie et al., 2003; Battaglia & Benz, 2006). The electron spectrum producing this photon spectrum can be inferred by a variety of techniques, forward-fitting (Holman et al., 2003), regularized matrix inversion (Piana et al., 2003; Kontar et al., 2004), or matrix inversion with data-adaptive binning (Johns & Lin, 1992). The strengths and weaknesses of these methods for reproducing features present in the electron spectrum are discussed in Brown et al. (2006). In this thesis forward-fitting is the preferred method. Of course, due to its nature, forward-fitting can only recover features present in the parametric form chosen but close analysis of residuals can inform the user of features not present in the model. The advantage of forward-fitting is that it provides a best-fit electron (or ion) distribution to the the observed HXR spectrum. As such, using this method promptly provides an electron distribution 'ready made' for comparison with numerical and analytical models.

Interestingly, the advent of RHESSI imaging spectroscopy (Hurford et al., 2002) confirmed earlier work using the Yohkoh spacecraft (e.g. Petrosian et al., 2002) that the spectral index difference between looptop and footpoint sources was not 2 as would be expected in the thick-target model (Emslie et al., 2003; Battaglia & Benz, 2006; Saint-Hilaire et al., 2008; Petrosian & Chen, 2010). Furthermore, Kontar et al. (2014) found that the electron rates at the looptop were more than was required to produce the footpoint emission. Introducing an effective turbulent mean free path, λ, parallel to the magnetic field to account for the effect of pitch angle diffusion of particles they found that this should be typically less than the length of a loop and approximately the size of the acceleration region, $10^8 - 10^9$ cm, to be consistent with observations (this will be discussed further in Chapter 4).

The work of Xu et al. (2008) and Jeffrey & Kontar (2013) focussed on the shape of the flaring coronal loops finding that both the length and width of coronal looptop sources increase with energy. The expansion in length is found (Xu et al., 2008; Guo

et al., 2012) to be consistent with an initial extended acceleration region within the loop itself plus an additional length proportional to the photon energy squared. This extra length is due to the higher energy particles moving further along the loop before they interact with the flaring plasma. Kontar et al. (2011a) studied one particular coronal loop, finding that not only did the length increase with energy but furthermore there was an increase in width. The authors, and another study by Bian et al. (2011), suggested that this may be due to magnetic field line diffusion, parallel to the direction of the field, due to magnetic turbulence in the loop. Magnetic turbulence is, of course, a requirement of the stochastic acceleration process studied in this thesis.

Attempts to constrain timescales in stochastic acceleration models (Miller et al., 1997, for a review) using simplifications such as the leaky-box Fokker-Planck approximation by applying it to inferred electron distributions has been attempted by Petrosian & Chen (2010) and Chen & Petrosian (2013). This approximation ignores the essential spatial dependencies of the flaring structure however, and although useful as an illustration, cannot be considered the entire flare picture. The effects of ignoring spatial dependencies on acceleration and transport are discussed in Chapter 4.

The above papers show the myriad possibilities that the spatial resolution of RHESSI enables. The remainder of this chapter will present first a more detailed look at the imaging concept of RHESSI, followed by how it performs spectroscopy, finishing with the imaging spectroscopy of two flares. The events are GOES M-Class limb flares and are chosen due to their application to the following Chapters, 3 and 4. The density weighted mean electron flux is obtained via forward-fitting the photon spectrum and is discussed. Further to this, the fits to the thermal part of the photon spectrum directly provides the temperature and indirectly an estimate of the density and acceleration region extent which are used as the starting parameters of Chapter 4. The calculation of densities from imaging spectroscopy will be explained in this chapter.

2.2 Introduction to RHESSI Imaging

At this point it is instructive to examine how the RHESSI spacecraft makes images, to this end the next few subsections will discuss this before ending with a more detailed description of the CLEAN algorithm. All of the following information can be found on http://hesperia.gsfc.nasa.gov/rhessi3/ and in Hurford et al. (2002).

2.2.1 The RHESSI Imaging Concept

RHESSI makes observations of the X-rays and gamma-rays in space such that they can be used to produce images by a user on the ground. The collimator pairs in front of each detector modulate the incoming flux. To understand how, first consider a point source that emits a constant flux. X-rays are emitted at a steady rate and travel in straight lines in all directions, with only those travelling in the direction of the spacecraft impacting on the grids, and maybe the detector. It is important to note that since RHESSI is far enough away from the Sun, all incident photons can be considered to be parallel.

Consider first a photon emitted exactly upon the spin axis of RHESSI. In this case, the front and rear collimators would be exactly aligned and from the photon's point of view the rear grid would be completely obscured by the front grid. Figure 2.1 shows this scenario, there is no reduction in the visible part of the detector to the photon during the rotation of the spacecraft. In this case, 50% of the light incident on the grid would be detected.

If the source is off axis, however, then the amount of transmission varies from 0% to 50% depending on how the front and rear grids are aligned. Figure 2.2 shows the case for a source that is below the spin axis. In this particular configuration there is 50% transmission when the slits and slats are vertical (rotation= 0) and 0% for when the slits and slats are horizontal (rotation= $\pi/2$).

It is clear that the signal impacting upon the detector will modulate between 0% and $\leq$50% for any source. With the shape of the signal detected depending on the exact position, intensity and size. This is shown in Figure 2.4.

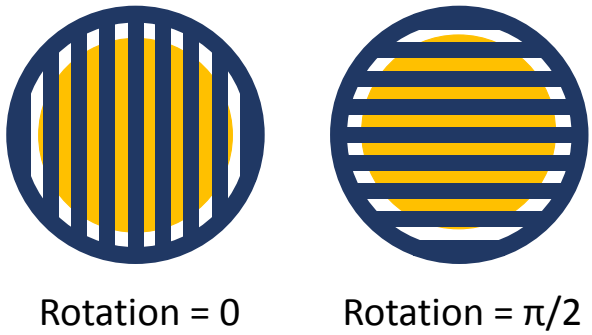

Figure 2.1: The view of an incident photon for the case where it has been emitted along the spin axis of RHESSI. The front grid is shown here in blue and completely obscures the rear grid. The germanium detector is shown as the yellow circle.

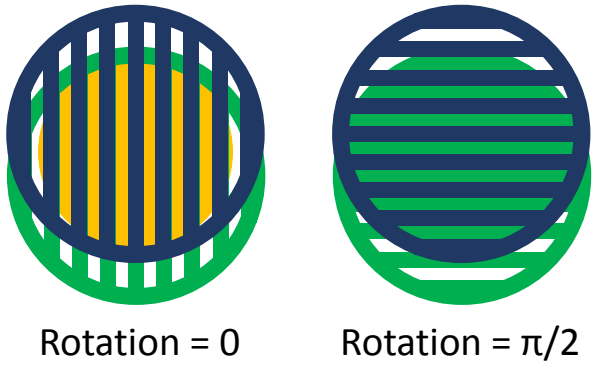

Figure 2.2: The view of an incident photon for the case where it has been emitted below the spin axis of RHESSI. The front grid is shown here in blue and the rear in green. The germanium detector is shown as the yellow circle.

Figure 2.3 shows how a photon detected at a specific point on the detector could have come from a variety of positions. The combination of this information for all RMCs is what enables the reconstruction of an image. Tracing the photons back to the Sun produces a probability map where photons could, and could not, have originated from. This map then rotates with the spacecraft.

For a single source the modulation profile is shown in Figure 2.4 (reproduced from Hurford et al. (2002)). It shows clearly how the modulation pattern changes depending

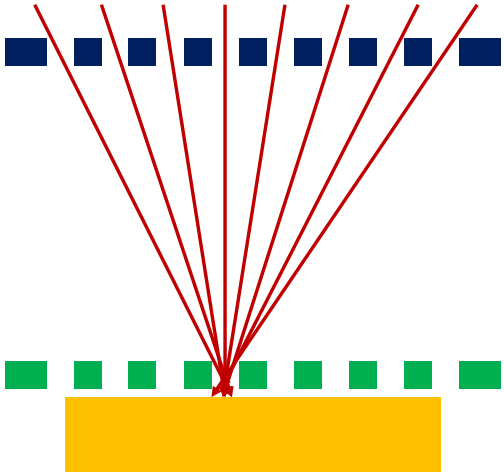

Figure 2.3: Showing the possible origin of a photon incident upon a specific part of a RHESSI detector. The front and rear grids are shown in blue and green and the detector is shown in yellow. The possible photon paths are shown as the red arrows.

on the size, position and intensity of the source. The top panel shows the pattern of a point source, which is off axis and acts as a comparison for the successive figures. The second panel shows a point source, in the same position, but with half the intensity, the modulation pattern is unchanged in time but it's amplitude is halved, this is due to the linear response of the collimator/detector system. The third panel shows the effect of moving the source in azimuth around the rotation axis, the profile is shifted in time but the amplitude is the same. Panel 4 shows what happens when the source is moved further from the spin axis, in this case the modulation cycles per rotation increase. Increasing the size of the source while keeping the same intensity results in a decrease in amplitude but the time modulation remains unchanged, this is shown in panel 5. Panel 6 shows that with a further increase in size, the amplitude of the signal is further decreased.

Of course, real flares will have more complicated shapes than simple point sources. A modulation profile from an unknown source is shown in the last panel. The central task of the RHESSI software is thus the inverse problem of source geometry, given the information of the modulation profiles from the 9 RMCs.

If the background is neglected, the expected counts, $\mathcal{C}$, in the i-th time bin are given

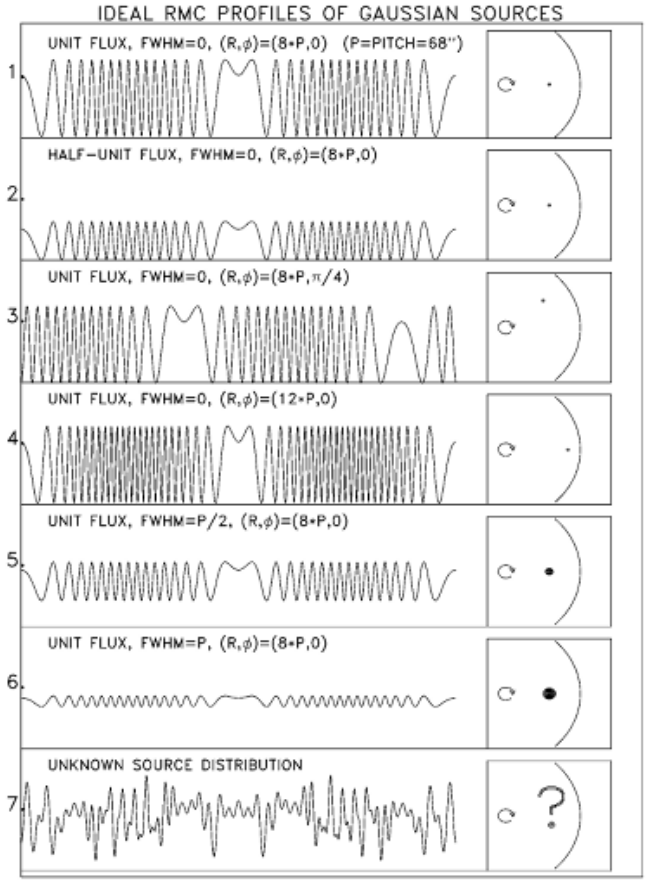

Figure 2.4: Modulation profiles for different source size, intensity and position. Taken from Hurford et al. (2002).

by (Hurford et al., 2002),

$$\mathcal{C}_i = A \sum_m P_{im} F_m \Delta t_i, \tag{2.1}$$

where the flux incident on RHESSI's front grids from pixel m is F_m, P_{im} is the probability of that a photon originating in pixel m and incident on the front grid will be counted in the i-th time bin during interval Δt_i by a detector with area, A. Note that since m is the index of a two-dimensional map, P_{im} is really a numerical 'cube'. Since P_{im} can be calculated from the grid properties and the collimator aspect the inverse problem can be summed up as follows; find the source map, F_m, given a measurement of count rates in each time bin. The relationship between P_{im} and the transmission probability is discussed in detail in Hurford et al. (2002) but is beyond the scope here.

2.2.2 The Modulation Pattern

The two-dimensional modulation pattern characterizes the instantaneous response of the collimator. This can be thought of as a probability map of where a photon observed at a specific time originated on the Sun, it is the i-constant plane of P_{im}. The modulation pattern is fixed in the rotating frame of the spacecraft but the cube P_{im} must be calculated over the non-rotating solar map which is also drifting with respect to the imaging axis. This would require rotating and shifting the modulation pattern at each time before evaluating at each map pixel. If done in a straightforward way this would be far too computationally extensive and require too much storage. Two simplifications reduce this load: the first is that the mapping is done in polar coordinates (switched back to cartesian before use by the user) and the second is the instrument response is calculated in terms of 'universal modulation parameters', described fully in Hurford et al. (2002). By using these techniques the P_{im} 'cube' can be evaluated efficiently and so a map can be reconstructed by inverting the observed modulation profile (equation 2.1) by methods such as CLEAN (Högbom (1974); Hurford et al. (2002) for method, and Battaglia & Benz (2006); Simões & Kontar (2013); Jeffrey & Kontar (2013) for examples of the method applied to solar flares) discussed in the next subsection.

In order to use any of the commonly used imaging algorithms one must first account for the detector livetime (Smith et al., 2002). Particularly, in order to interpret the number of photons, $\mathcal{C}_{im}$, incident on the detector during the i-th time bin the detector livetime, τ_i, must be taken into account (livetime = observation time - deadtime, deadtime being the period after the recording of a photon when the detector is unable to record another) (Smith et al., 2002). After this is done the expected counts, $\mathcal{C}_{im}$, in the i-th time bin from a source with the photon flux, F_m, at map pixel m is given by,

$$\mathcal{C}_{im} = AF_m T_i \tau_i \{1 + \sum_n a_n^i \cos[n(\Phi_{im} - \Psi_n^i)]\}, \tag{2.2}$$

where the subscript n refers to the n-th harmonic and energy dependent subcollimator transmission, T_i, plane offsets, Ψ_n^i, and amplitudes, a_n^i, are evaluated at map center.

As a result of the linearity of the detector and subcollimator response the predicted modulation profile, $\mathcal{C}_i$, for any source is just the sum over $\mathcal{C}_{im}$ for all non-zero pixels.

This predictive principle is used by several of the RHESSI reconstruction algorithms to assess the consistency between the reconstructed image and the observed modulation profiles.

2.2.3 Image Reconstruction

In Chapter 1 Section 1.8 some of the methods for reconstructing images from RHESSI data were mentioned. In this thesis the only method used is the CLEAN algorithm due to: first, it is much faster than Pixon; second, the Maximum Entropy Method can 'over-resolve', i.e. create too many point-like sources and often cannot reconstruct extended sources; third, it is not as restrictive as VisFwdFit which relies on specific source shapes (Gaussian, elliptical) and is limited to one or two sources, and; fourth, uv_smooth produces similar images to CLEAN and is not as widely used, making the cross comparison of the results here more difficult. Further to this, it has been shown that with the correct value of the CLEAN beam width parameter (Dennis & Pernak, 2009) the method produces similar source sizes to the other algorithms. Finally, CLEAN as an algorithm has been used for a long time in radio astronomy (Högbom, 1974) and thus is well understood. As such the CLEAN algorithm is suitable for the analysis required here.

The CLEAN Imaging Algorithm

CLEAN (Högbom, 1974; Hurford et al., 2002; Schmahl et al., 2007; Dennis & Pernak, 2009) is an iterative process which has been adapted for the analysis of RHESSI hard X-rays from radio astronomy. It is based on the assumption that the source being studied can be represented by the superposition of point sources. The basic method postulates that the observed 'dirty map' is a convolution of a set of point sources with the instrument point spread function, PSF, which can be thought of the imager's response of to a delta function source. That is,

$$\mathcal{D} = \mathcal{P} \otimes I_{\text{source}}, \tag{2.3}$$

where $\mathcal{P}$ is the point spread function for one or many subcollimators and/or harmonics, I_{source} is the source distribution and $\mathcal{D}$ is the back-projected 'dirty' map. The symbol $\otimes$ denotes the convolution.

The CLEAN algorithm proceeds iteratively, firstly an image called the residual map is created and is initialized to the back projection map (see Hurford et al., 2002) at a value I_0. The position, (x_j, y_j), of the pixel with the highest flux, F_j, is found and then saved in a 'CLEAN component' table. The point spread function, $\mathcal{P}$, normalized to μF_j (where $\mu \leq 1$ is called the loop gain) is subtracted from the current residual map, I_n, to yield a new one, I_{n+1}. This is repeated until one of three things is achieved: a maximum number of iterations is reached, the residual map contains a peak of negative flux that is greater in value than the largest peak of positive flux, or the observed modulation profile is considered to agree with that from a CLEAN comparison as indicated by a χ^2-test.

The final residual map, I_{final}, in all probability consists mainly of noise, the image information is actually contained in the CLEAN component table where the intensity and position of each peak found during the iterative process are stored. These components are convolved with the CLEAN point spread function, otherwise known as the CLEAN beam width parameter, $\mathcal{P}_{\text{clean}}$, which has a gaussian profile with a full width half maximum that reflects the effective resolution of the subcollimators used in creating the 'dirty' map. The final 'CLEANed' map is given by,

$$I_{\text{clean}} = \sum_j \mathcal{P}(x_j, y_j)\mu F_j + I_{\text{final}}, \tag{2.4}$$

which is purely the sum of the CLEAN components, convolved with the CLEAN beam width parameter. The final residual map, I_{final}, is added which gives the user some idea of the noise in the image, this is not the case for the other possible image reconstruction techniques.

A summary of the other imaging techniques is included in Hurford et al. (2002); Schmahl et al. (2007); Dennis & Pernak (2009) and in Chapter 1 Section 1.8. In the next section a brief review of the RHESSI as a spectrometer will be given.

2.3 Introduction to RHESSI Spectroscopy

Once an image, or alternatively a spectral file for full-Sun analysis, has been obtained the underlying photon producing electron distribution can be inferred. OSPEX (Schwartz et al., 2002) allows the selection of areas within an image file known as regions of interest (ROIs) where the spectrum can then be analysed. This allows detailed analysis of the spectrum throughout a flaring source. For a full-Sun spectrum the emission from the flare is purely energy and time dependent, with no spatial information included. In this thesis forward-fitting (see e.g. Holman et al., 2003) is used to fit the photon spectrum by fitting the expected emission from a specific population of particles rather than purely by some shape of function. This is so as to tell the user something about the particles that produce the emission, rather than purely the best-fit to the shape of it. The rest of this section will discuss the RHESSI spectrometer, focussing on how the photon spectrum is obtained from the observed counts. A more detailed review can be found in Smith et al. (2002) and is summarized here.

2.3.1 The RHESSI Spectrometer

The exact make-up of the germanium detectors, how they are cooled and the spacecraft shielding is discussed in Lin et al. (2002) and Smith et al. (2002) but is beyond the scope here. The combination of the ultrapure, cooled, germanium detectors together with the attenuators (discussed in Chapter 1 Section 1.8) gives RHESSI unprecedented dynamic range across 4 order of magnitude in energy ($\sim$ 3 keV to $\sim$ 17 MeV). The resolution is limited by different effects depending on the range, at energies $\leq$ 200 keV (photons detected in RHESSI's front segments) the width of a spectral line is dominated by noise within the spacecraft electronics and is approximately constant. At energies higher than this there are two sources of noise: the counting statistics of electron-hole pairs in the detector (which scales as the square root of energy) and broadening due to holes or electrons becoming trapped in the crystal (which behaves linearly with energy) (Smith et al., 2002).

RHESSI was not designed to be a low background instrument. The constraints of

being a NASA small explorer mission not allowing the heavy shielding that would have been needed. Furthermore, there was no equatorial orbit available which would have reduced all background components apart from cosmic ray diffusion. This would be due to minimizing cosmic rays incident on the spacecraft and eliminating exposure to the trapped protons in the South Atlantic Anomaly (SAA), which happens several times a day on successive orbits. Solar flares are bright sources however, and so luckily the data is count rate limited and not statistical fluctuations from a background. The primary sources of background are transitions through the SAA, smooth modulations due to changes in the geomagnetic latitude and thus incident cosmic ray flux and occasional precipitation of electrons from the outer radiation belt when RHESSI is at its highest geomagnetic latitudes. Further to this there are instrument anomalies that must be taken account of before the actual photon spectrum is obtained such as: detector dropouts, individual detector anomalies, spectral artifacts and image events. These are all discussed in detail in Smith et al. (2002).

2.3.2 Spectral Data Analysis

As mentioned before, spectral analysis with RHESSI is an inverse problem where the data is the counts per spectrometer channel and the goal is to find the incident photon spectrum that produced it. Figure 2.5 is a flow chart showing the data analysis process which produces the corrected count/photon spectrum. The spectral analysis of this data is achieved in OPSEX (Schwartz et al. (2002) and http://hesperia.gsfc.nasa.gov/rhessidatacenter).

Gain, Livetime and Background Subtraction

The first point of call when producing RHESSI data is to account for gain drift and deadtime. The first of these is made simpler by the linearity of the electronics and the easily identifiable background lines. Deadtime correction starts with the livetime counter in the electronics, corrects for double rejection of piled up events and compensates for data dropouts.

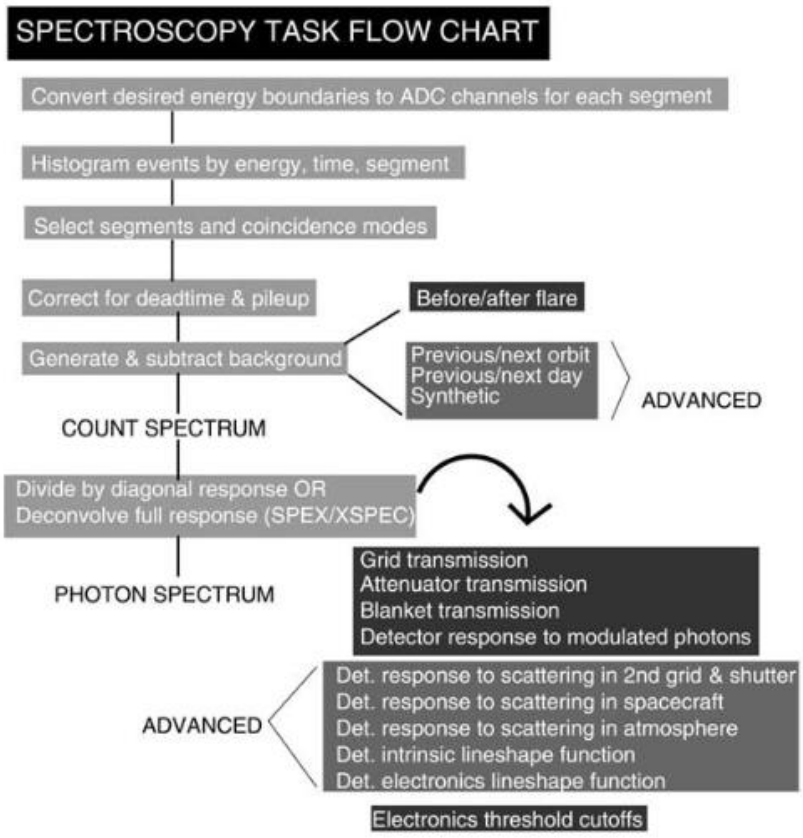

Figure 2.5: Flowchart of spectroscopic analysis with RHESSI data. The features that are highlighted 'advanced' are only needed for a few flares. Where SPEX or XSPEX is shown read as OSPEX. Taken from Smith et al. (2002).

For the case of full-Sun spectra the user then selects and subtracts a background. With imaging spectroscopy there exists no explicit method within OSPEX to calculate background, as the images purely consist of data and error. For full-Sun spectra the background is usually estimated by selecting one or more time ranges before or after the flare. This background is then subtracted from the count rate and is sufficient for most flares. For long duration events this may not be enough as these flares can continue for tens of minutes during which the background can change significantly. Fortunately, OSPEX allows the selection of several intervals before and after which can be joined via polynomial interpolation to provide a more accurate background subtraction for each energy channel. For very few flares neither of these methods are suitable and a more convoluted technique must be used such as, for example, subtracting the background

exactly 1 day before (15 RHESSI orbits).

Spectral Response Matrix

The series of instrumental effects that affect the detection of flare photons on the detectors is the spectral response and is encoded in the spectral response matrix (**SRM**) created during the production of an image or lightcurve. Events that can influence the detection are many, they include:

1. absorption in the constituent parts of the spacecraft, e.g. the grids,
2. Compton scattering into and out of the detectors,
3. Compton scattering from the Earth's atmosphere,
4. noise originating from electronics,
5. degradation in resolution due to radiation damage, and/or,
6. the low energy cutoff imposed by the electronics.

The effects listed above can contribute to both diagonal and off-diagonal terms. As mentioned in Chapter 1 Section 1.6.3, anything affecting the efficiency of detecting a photon at its energy contribute to the diagonal terms of the **SRM** whereas off-diagonal terms result from the photon being observed at a different energy, usually lower.
For the study of flares with no significant emission $\gtrsim$ 100 keV the diagonal terms of the **SRM** can be used alone. This is because the response of the front segments below this energy is dominated by complete absorption and not scattering. Since most spectra are steeply falling the count rate in any energy band is dominated by photopeak (the peak at the actual photon energy) counts up to $\sim$ 100 keV (Smith et al., 2002). If the attenuators are in, and low energies are being studied, or for events with significant emission at high energies the full **SRM** needs to be used. For both events studied in this thesis the full **SRM** is used.
The **SRM** is accounted for during the fitting of the spectrum. The user specifies a model which, as already mentioned, will most likely be the emission from a model

electron distribution together with other corrections to the spectrum, such as pulse pile-up (for a full description see Smith et al., 2002) and photon backscattered albedo from the photosphere (see Figure 1.5). This model is then multiplied by the **SRM** (see equation 1.42) before comparison with the observed photon spectrum to check goodness-of-fit. This is then repeated, varying the free parameters until a best fit is produced.

The spectral response for three different energies of photons is shown in Figure 2.6. At 50 keV the photopeak dominates but the K-shell escape peak is visible. At 350 keV there is a strong Compton continuum, along with small K-shell fluorescence peaks from nearby passive material, such as the tungsten grids. At 2500 keV pair production can occur, there are two narrow lines due to positron annihilation ($\sim$ 511 keV) and the escape of one or two positron annihilation photons from the detector. This shows the importance of correctly accounting for the spectral response when analysing RHESSI spectra.

As mentioned, further discussion of the above section can be found in Lin et al. (2002) and Smith et al. (2002).

2.3.3 Summary of Fit Functions Used

As of March 2015 there are 47 fit functions available for use in OSPEX, the full list can be found on `http://hesperia.gsfc.nasa.gov/ssw/packages/spex/idl/object_spex/fit_model_components.txt`. The 3 fit functions used in the next two sections are summarised here:

1. vth - this fits the optically thin thermal bremsstrahlung (Chapter 1 Section 1.5.1) from a single temperature distribution of electrons to the thermal part of the photon spectrum. The function has three fit parameters: the temperature, kT [keV], the emission measure, EM [cm^{-3}], and the relative abundance of iron, nickel, calcium, sulfur and silicon compared to that in the Chianti database Del Zanna et al. (2015). This last parameter is kept fixed at 1 throughout the fits and the full Chianti database is used, i.e. the fit assumes the Chianti abundances are

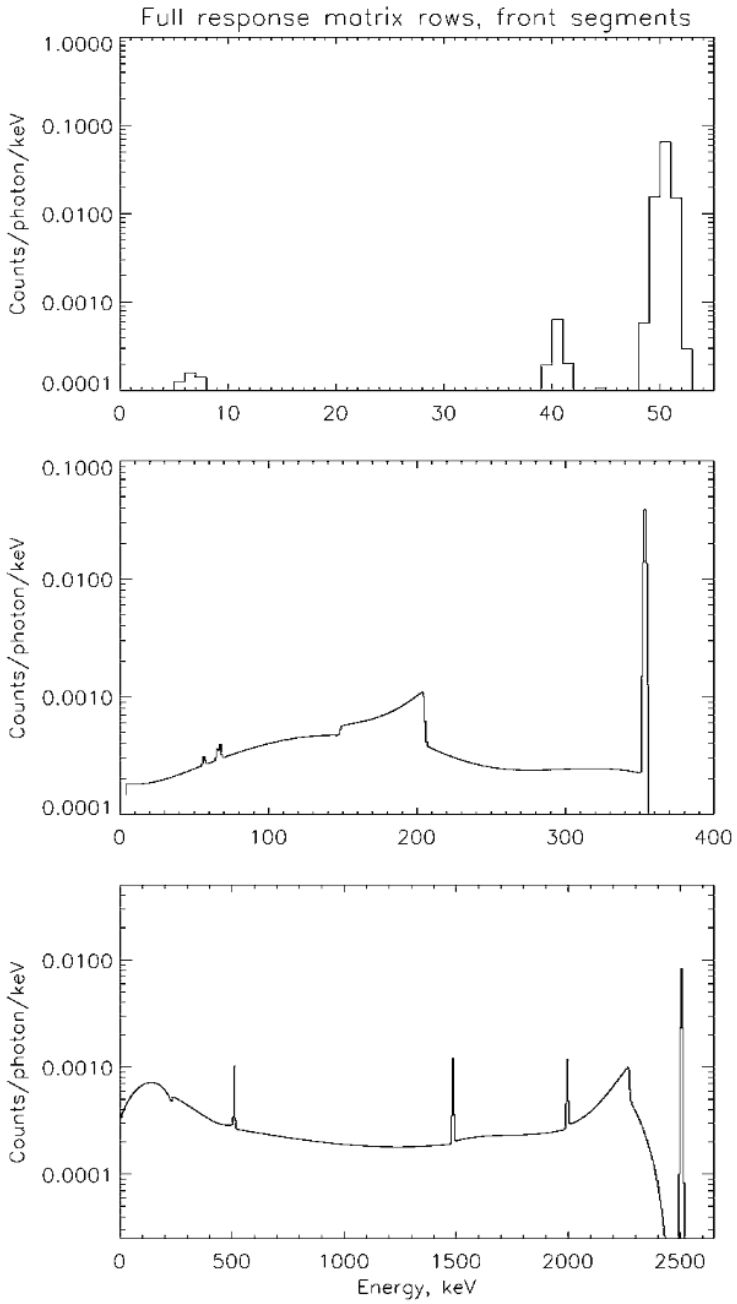

Figure 2.6: The spectral response of RHESSI for three different photon energies. From top to bottom: 50 keV, 350 keV and 2500 keV. Taken from Smith et al. (2002).

correct. The other two parameters are kept free, in order to provide a best-fit to the thermal part of the spectrum.

2. thin2 - this is the updated version of thin and is two to ten times faster than

the original function. It fits the thin-target emission from an isotropic electron flux distribution, $F(E)$ [electrons s^{-1} cm^{-2} keV^{-1}]. The six fitting parameters are: the normalisation flux, $\langle nVF_0 \rangle$ [10^{55} electrons cm^{-2} s^{-1}] (see equation 1.40); the power-law index below the break energy, δ_1; the break energy, E_b [keV]; the power-law index above the break, δ_2; the low energy cutoff, E_c [keV], and; the high energy cutoff, E_h [keV].

In this work a single power-law fit is used, so the break energy and high energy cutoff are fixed at 32000 keV so they do not effect the photon spectrum at the energies observed. The spectral index above the break is kept fixed at a higher value than the expected δ_1 to avoid any effects on the index below the break. The low energy cutoff is set at 20 keV due to the emission being dominated by the thermal component at low energies which does not allow the non-thermal fit to reliably determine it. Thus there are two free parameters, the normalisation flux and the power-law index, which will be used to find a best-fit to the non-thermal part of the spectrum.

3. albedo - this is a pseudo function correcting for the bump in the photon spectrum at around $\sim$ 30 keV due to the Compton backscattered photons from the photosphere (Kontar et al., 2006), as mentioned in Chapter 1 Section 1.5.2. Fit parameters are varied during the application of the **SRM** (see Chapter 1 Section 1.6.3) to correct the model for albedo. The function accounts for the source position and only has one parameter, which is the anisotropy. This ranges from 0 to 1 where 1 is isotropic. The parameter is always kept fixed and is set to 1 during the fits that follow due the the fact the X-ray emitting electron has been shown to most likely be isotropic (Kontar & Brown, 2006; Dickson & Kontar, 2013).

It should be noted that the emission from the footpoints is more often fit by the thick-target bremsstrahlung emission from an electron flux spectrum. There are a few functions in OSPEX to account for this, with the most up to date being thick2_vnorm where most fit parameters are analogous to the parameters in thin2. Fitting throughout with the thin2 function avoids complication however, and as long as the same

bremsstrahlung cross-section is assumed in the numerical or analytic model the results are suitable for comparison.

The next three sections will present the imaging spectroscopy analysis of two flares.

2.4 Chosen Events

The first flare is the well studied 2005 August 23, GOES class M3.0, flare (Xu et al., 2008; Jeffrey & Kontar, 2013) that is unusual in the fact that most of its emission comes from the corona with HXRs observed up to ~ 50 keV and negligible footpoint emission. The reason this is flare chosen is as an example of the scenario in Chapter 3 where an analytical model with cospatial acceleration and collisional losses in a regime with no particle escape is considered. Furthermore, the analysis of this flare, and others, in Xu et al. (2008) found that the emission from this flare was consistent with an extended acceleration region within the loop surrounded by a halo of escaping high energy particles, the effects of which are studied for a 'standard' flare morphology in Chapter 4.

The second flare is the 2011 February 24 flare (studied by Simões & Kontar, 2013, for example). This flare is a good example of the most commonly seen flare morphology (see Section 1.5.3) consisting of a relatively softer and hotter coronal looptop source and relatively cooler and harder footpoint sources. It is an M3.5 class flare and is chosen due to the ease in identifying the looptop and footpoint sources. This flare will provide the initial conditions for the numerical model in Chapter 4.

2.4.1 Imaging Spectroscopy of the 2005 August 23 Flare

Lightcurves

Figure 2.7 shows the corrected and uncorrected count rates per second per detector for the 2005 August 23 flare, from 14:20:00-14:40:00 UT. At the start of the observation the two lowest energy bands, 2-12 and 12-25 keV, are slowly increasing, reaching a peak at around 14:30:00 UT followed by a gradual decrease until the end of the observation.

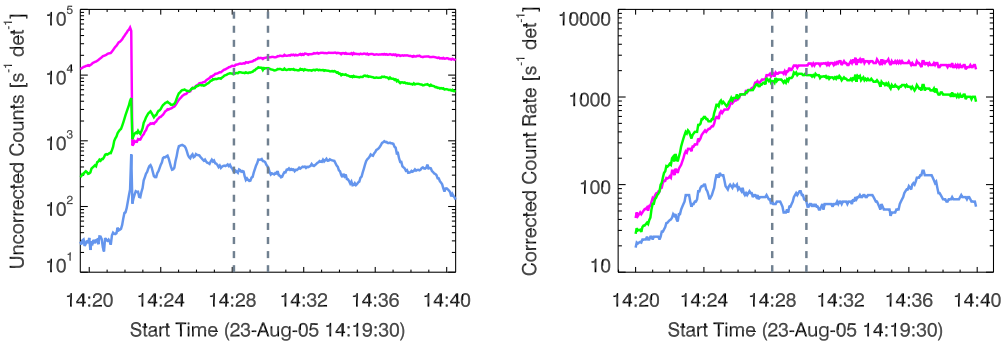

Figure 2.7: Uncorrected (left) and corrected (right) count rate for the 2005 August 23 flare for energy bands: 6-12 keV (magenta), 12-25 keV (green) and 25-50 keV (light blue). The time frame of interest is bounded by the two vertical grey lines. In the uncorrected counts the drop in count rate just after 14:23:00 UT is due to the switch to attenuator state one.

The 25-50 keV counts has repeated peaks throughout the observation. The timescale used for imaging spectroscopy is shown by the grey dash vertical lines. This was chosen as it was the near the peak of the soft X-ray emission, so the loop was visible most clearly across the energy bins used for spectroscopy. Furthermore, it incorporates one of the HXR peaks and it enables cross comparison with the work of Jeffrey & Kontar (2013).

Imaging Spectroscopy

The CLEAN (Högbom, 1974; Hurford et al., 2002) image shown in Figure 2.8 was created using CLEAN beam width parameter of 1.8 as in Jeffrey & Kontar (2013) to enable direct comparison. The loop morphology is clearly seen.

The photon flux fits are shown in Figure 2.9 for each region in Figure 2.8 and for the full-Sun spectrum. For these fits the low energy cutoff is kept fixed at $E_c = 20$ keV for the reasons discussed above in Section 2.3.3. The fit function thin2 is also set to be a single power-law. It is noted that although these fits all have an acceptable χ^2 (see Kontar et al., 2011a), there is some systematic behaviour in the residuals for the fit to region 0 and for the full-Sun spectrum. This could perhaps be offset by allowing the low energy cutoff to be free, allowing a broken power-law, or introducing

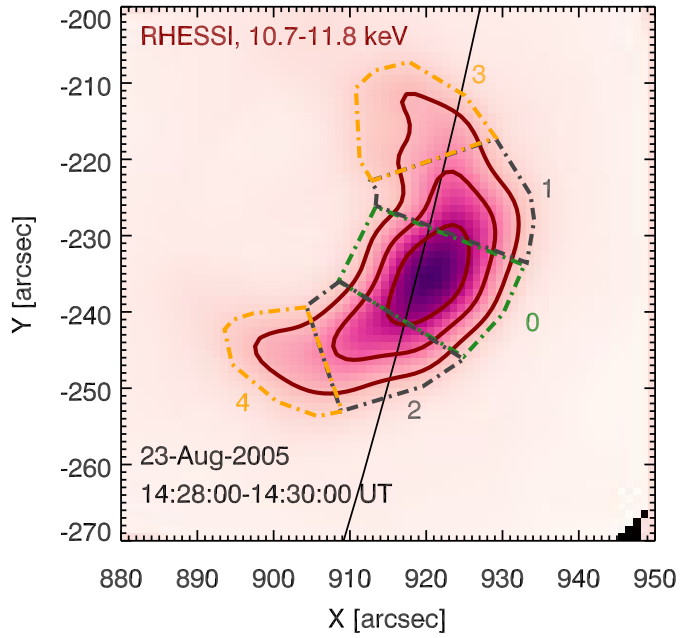

Figure 2.8: CLEAN image of the 2005 August 23 flare. The dot-dash lines show the regions of interest (ROIs) used to produce spectra, labelled 0-4. The red contours show the looptop emission in the $10.7 - 11.8$ keV (30%, 50% and 75%) energy band overplotted over the clean image in the same range.

an albedo correction component (for region 0). The reason for fixed E_c has already been discussed, while a single power-law is chosen as there is not enough non-thermal emission to constrain any break in the power-law form adequately. Furthermore, an albedo component should not have a large effect on the imaging spectroscopy of an above the limb flare.

The low energy part of the spectrum is fit with the emission from an isothermal plasma (vth) which gives an average temperature, $k_B T$, and emission measure, $EM = \bar{n}^2 V$, for the flaring plasma. The thin2 function provides a non-thermal normalisation flux, $\langle nVF_0 \rangle$, and the power-law spectral index, δ. A summary of these results, where the regions have been switched for the distance from the top of the loop (the maximum emission in ROI 0), is shown in Figure 2.10. The spatially integrated fit gives $EM = 0.28 \pm 0.01 \times 10^{49}$ cm^{-3}, $T = 23$ MK, $\langle nVF_0(E) \rangle = 1.28 \pm 0.05 \times 10^{55}$ cm^{-2} s^{-1} and $\delta = 5.36 \pm 0.01$. The volumes used to calculate the densities for each spectral fit are

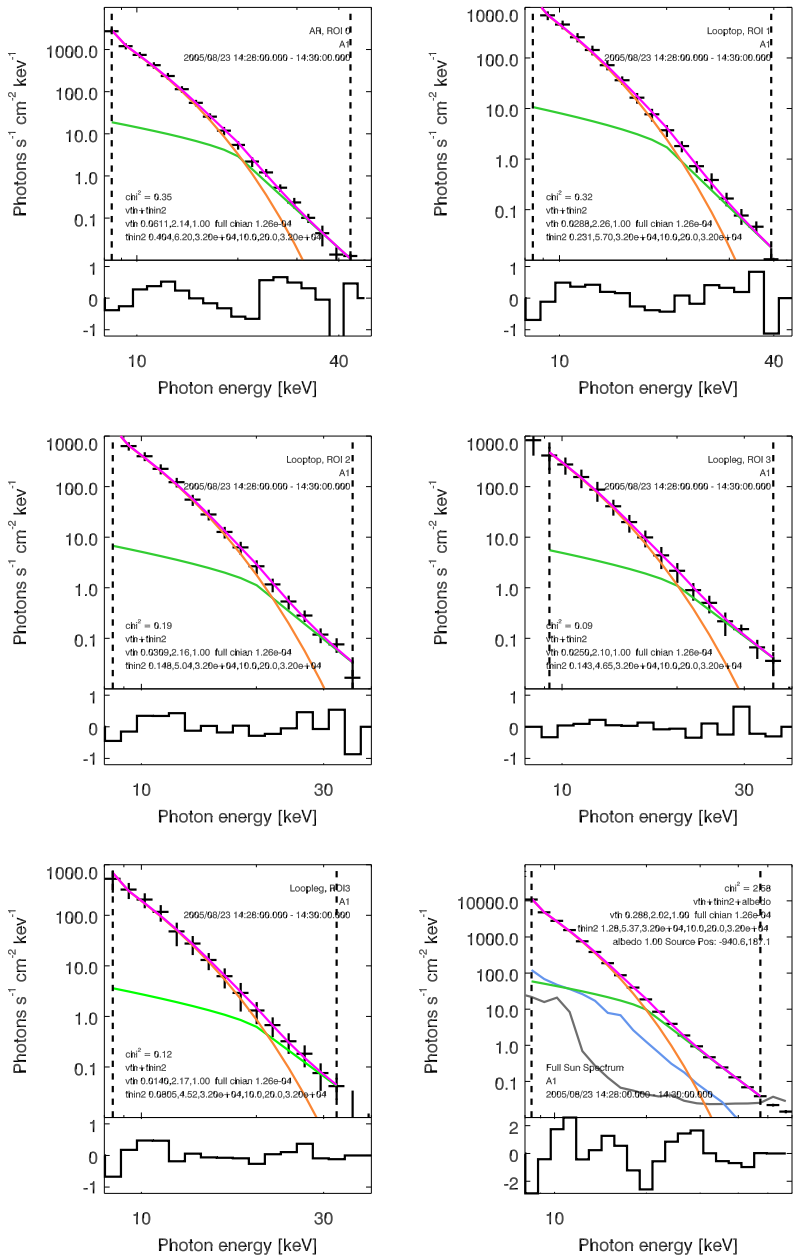

Figure 2.9: Photon X-ray spectra for the 2005 Aug 23 flare from CLEAN image (Figure 2.8) for: *Top Left*; Region 0, *Top Right*; Region 1, *Middle Left*; Region 2, *Middle Right*; Region 3, *Bottom Left*; Region 4, *Bottom Right*; full-Sun spectrum. HXR spectrum is shown as black data points. Fitting result is shown by the magenta line and is composed of a thermal (orange) and thin-target (green) component, with an albedo correction (blue) for the full-Sun spectra. The range fitted for each case is shown by the vertical dashed lines.

shown in the table below (2.1). The density is approximately constant $\sim 2.5\times10^{10}$ cm^{-3}

Region	Thermal Volume [cm^{-3}]
0	6.1×10^{26}
1	5.5×10^{26}
2	5.8×10^{26}
3	8.6×10^{26}
4	5.2×10^{26}
total	3.1×10^{27}

Table 2.1: Thermal volumes, $V_{\rm th}$, used to calculate number densities, n_e.

within errors along the loop which agrees well with the density obtained from the full-Sun spectrum, 3×10^{10} cm^{-3}. There is a slight trend to harder spectrum with distance along the loop but δ is approximately constant within the errors. This is consistent with the findings of Xu et al. (2008) where there is a core acceleration region surrounded by a volume where escaping high energy particles are stopped. This can be seen in the CLEAN image itself (Figure 2.8), with the acceleration region being assumed the intense radiation at the top of the loop surrounded by a more diffuse 'halo' of emission produced by the escaping electrons. Interestingly, the densities obtained here are less than those found by Jeffrey & Kontar (2013) by a factor of 1.5-2. This could be from an overestimation of volume; due to the almost subjective nature of area and length estimations from CLEAN images the area could quite easily be different from that estimated by the VisFwdFit method used in Jeffrey & Kontar (2013). Furthermore, the fits performed by Jeffrey & Kontar (2013) included the Iron and Iron and Nickel emission lines at 6.7 and 8.1 keV, which could affect the fitted temperature and emission measure. In addition, Jeffrey & Kontar (2013) found that a CLEAN beam width parameter of 3 produced areas that agreed more closely with the other imaging algorithms. As mentioned before by Dennis & Pernak (2009), some values of the CLEAN beam width parameter produce areas inconsistent with other imaging algorithms, this can therefore have an effect on inferred volumes and thus

densities.

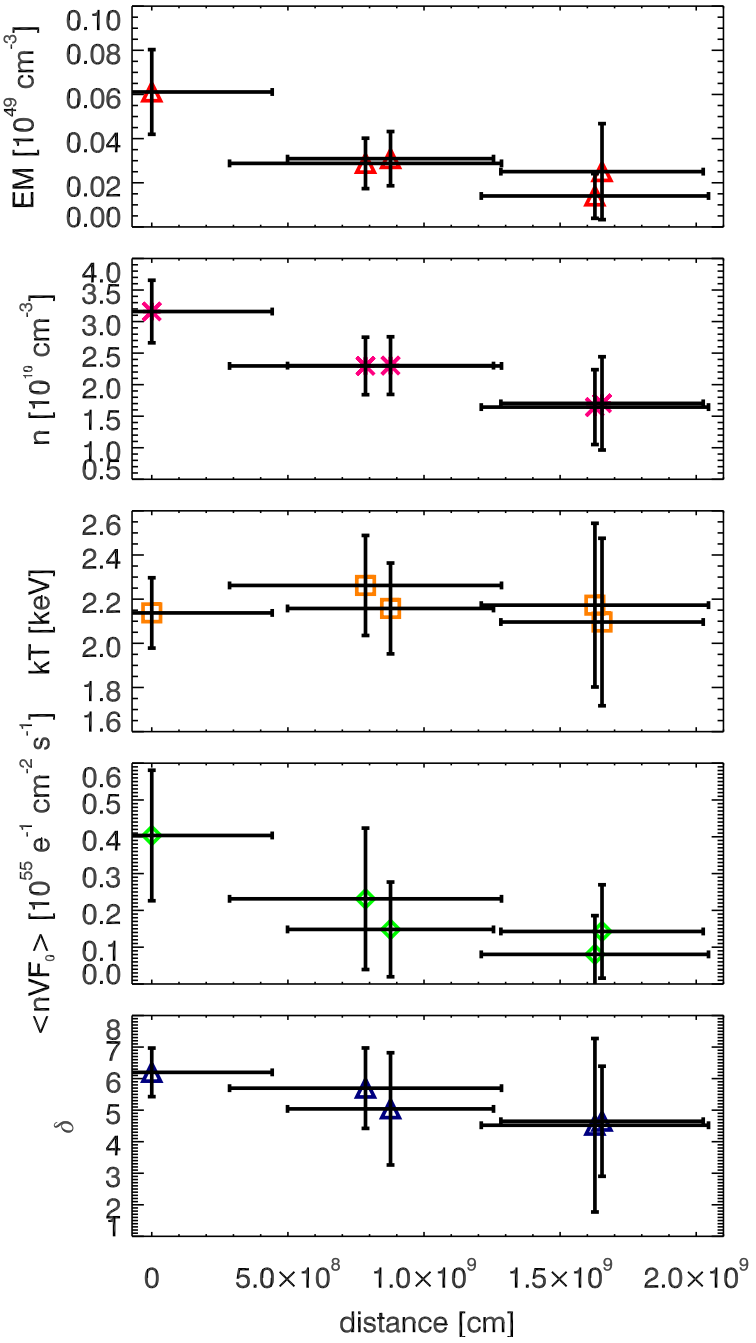

Figure 2.10: Fitting summary for the 2005 August 23 flare. From top to bottom, emission measure [cm^{-3}], density [cm^{-3}], temperature, kT [keV], non-thermal normalisation flux, $\langle nVF_0 \rangle$ [e$^-$ cm^{-2} s^{-2}] and spectral index, δ.

Density Weighted Mean Electron Flux

In Chapter 1 Section 1.5 the density weighted mean electron flux $\langle nVF(E)\rangle$ from thermal and non-thermal populations of electrons was discussed, with equations (1.38) and (1.40) giving the exact expressions. The importance of using the mean electron flux when comparing numerical and observational studies is outlined in Brown et al. (2003). The $\langle nVF(E)\rangle$ for the fitted photon spectrum are shown in Figure 2.11.

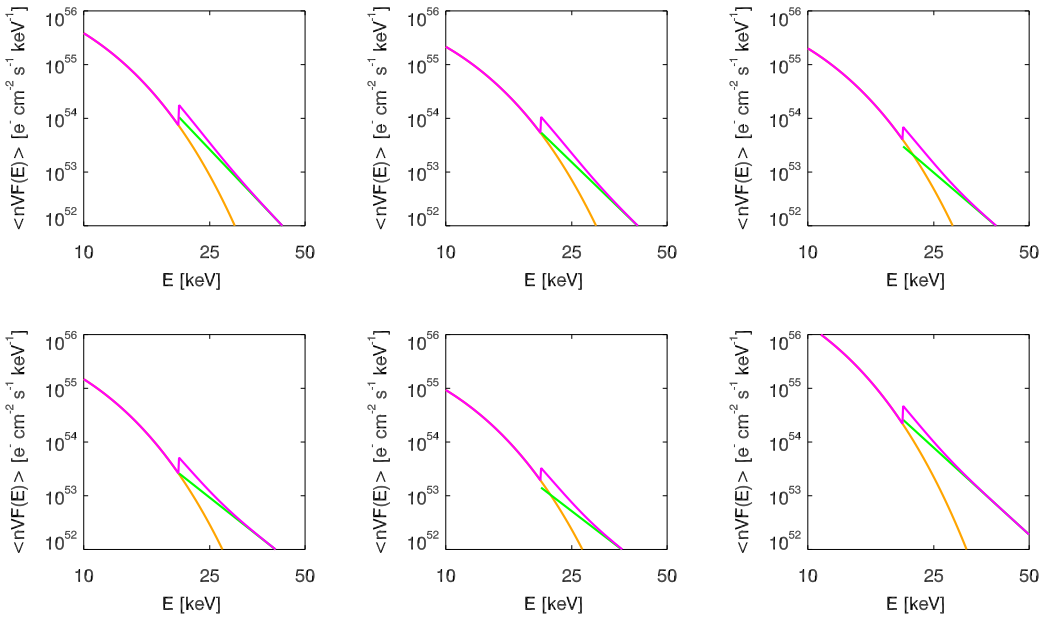

Figure 2.11: Inferred density weighted mean electron flux spectra for the 2005 Aug 23 flare: *Top Left*; Region 0, *Top Middle*; Region 1, *Top Right*; Region 2, *Bottom Left*; Region 3, *Bottom Middle*; Region 4, *Bottom Right*; full-Sun spectrum. The $\langle nVF(E)\rangle$ for the source from $10-50$ keV is shown by the magenta line and is composed of the thermal (orange) and thin-target (green) $\langle nVF(E)\rangle$.

It is important to note here that the discontinuity between the thermal and non-thermal parts of the flux is likely not physical (see e.g. Kašparová & Karlický, 2009, Fig. 2). It is due to the 'hard' boundary imposed by fitting with two separate populations of electrons in the thermal and non-thermal sources. The isothermal function in OSPEX assumes emission via CHIANTI (Dere et al., 1997; Del Zanna et al., 2015) which in-

cludes line and continuum emission from a thermal plasma. The non-thermal spectrum is assumed to purely originate from $e - i$ thin-target bremsstrahlung. In reality within the energy range where there is an overlap of thermal and non-thermal populations there will probably be a smoother transition between the two emission processes.

2.4.2 Imaging Spectroscopy of the 2011 February 24 Flare

Lightcurves

The corrected and uncorrected count rates for the second flare are shown in Figure 2.12. The lightcurves are plotted from 07:20:00 where the counts in the lowest energy bands (6-12 and 12-25 keV) are starting to rise. There then follows a rapid increase of harder X-ray counts from approximately 07:27:00 followed by 2 HXR peaks between the grey dashed lines in the figures (highlighting the limits of the imaging spectroscopy analysis). After this there is another peak in the 25-50 and 50-100 keV bands (around 07:33:00) followed by a gradual decrease back to the background level. The reasons for choosing the observation limits shown by the grey dash lines are twofold: one, it encompasses the HXR double peak structure and, two, it enabled corroboration with the work of Simões & Kontar (2013).

Imaging Spectroscopy

For the flare in question Simões & Kontar (2013) found that a CLEAN beam width of ~ 1.9 produced the best overlap with Pixon imaging of the same flare, so this is what is used here. Figure 2.13 shows the result, the looptop and footpoint regions being chosen so as to avoid overlap and thus cross contamination of the respective spectra. The looptop, footpoint and full-Sun spectra are shown in Figure 2.14. The spectrum is fit with a single power-law from thin-target bremmstrahlung (thin2) where the low energy cutoff is kept constant at $E_c = 20$ keV for all fits. The footpoint spectrum would normally be fit with the emission from thick-target bremmstrahlung due to the electrons losing all their energy as they impact upon the chromosphere. For the purposes of comparing the density weighted mean electron flux however, it is only

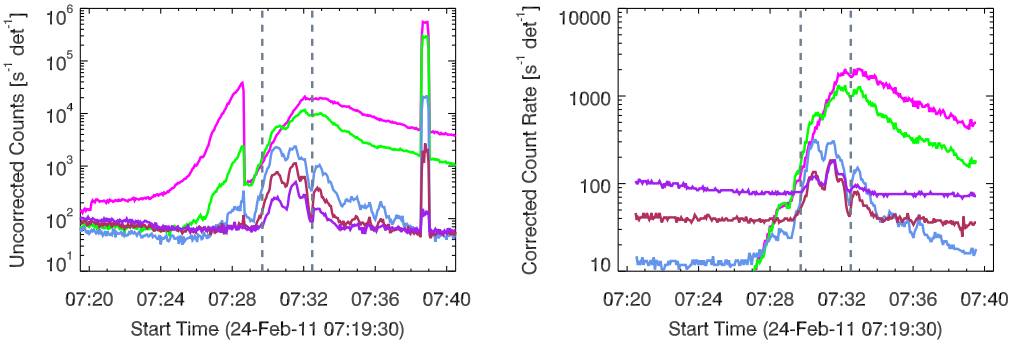

Figure 2.12: Uncorrected (left) and corrected (right) count rate for the 2011 February 24 flare for energy bands: 6-12 keV (magenta), 12-25 keV (green), 25-50 keV (light blue), 50-100 keV (maroon) and 100-300 keV (purple). The time frame of interest is bounded by the two vertical grey lines. In the uncorrected counts the drop in count rate just after 07:28:00 UT is due to the switch to attenuator state one, the sudden jump in count rate at ∼07:39:00 is due to a quick removal of shutters to check low energy counts.

important to ensure the same bremmstrahlung cross-section, as discussed in Chapter 1 Section 1.5.1. To this end, fitting the non-thermal energies with thin-target emission throughout avoids over-complication.

The looptop source is best fit by an emission measure $EM = 0.12 \pm 0.04 \times 10^{49}$ cm^{-3} and a temperature 23 MK, shown in Figure 2.14 (left top). The flux of non-thermal particles is $\langle nVF_0(E)\rangle_{\rm LT} = 0.62 \pm 0.15 \times 10^{55}$ cm^{-2} s^{-1} and the spectral index is $\delta_{\rm LT} = 2.91 \pm 0.43$. The footpoint sources, seen in the right top panel in Figure 2.14, are best fit by a flux of $\langle nVF_0(E)\rangle_{\rm FP} = 1.08 \pm 0.06 \times 10^{55}$ cm^{-2} s^{-1} and a spectral index of $\delta_{\rm FP} = 2.11 \pm 0.04$. The imaging spectroscopy results are consistent with the full-Sun spectrum seen in the bottom panel in Figure 2.14 ($EM = 0.20 \pm 0.01 \times 10^{49}$ cm^{-3}, $T =$ 21 MK, $\langle nVF_0(E)\rangle = 1.65 \pm 0.02 \times 10^{55}$ cm^{-2} s^{-1} and $\delta = 2.27 \pm 0.01$). Furthermore, the fits agree well with previous studies of the flare, such as that in Simões & Kontar (2013).

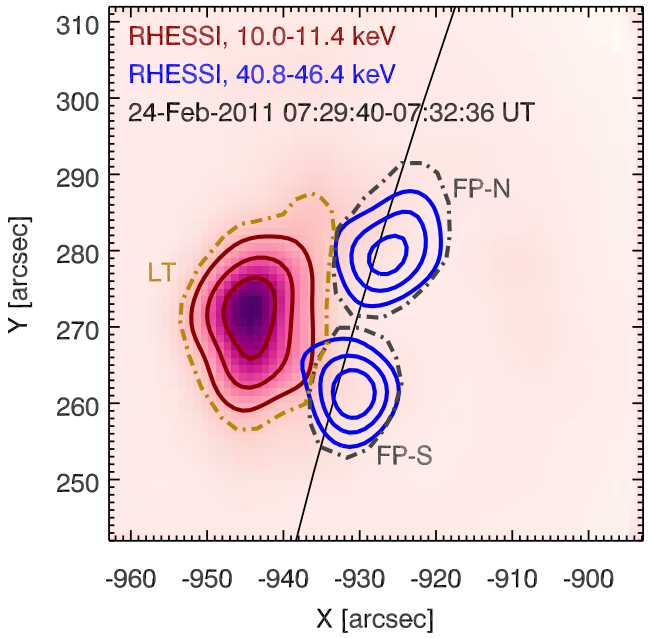

Figure 2.13: CLEAN image of the 2011 Feb 24 flare. The dot-dash lines show the looptop (LT) and footpoint (FP-N, FP-S) regions used to produce spectra. The red contours show the looptop emission in the $10.0 - 11.4$ keV (30%, 50% and 75%) energy band overplotted over the clean image in the same range. The footpoint emission at $40.8 - 46.4$ keV is shown by the blue contours (30%, 50% and 75%).

Density Weighted Mean Electron Flux

The density weighted mean electron flux for the 2011 Feb 24 flare is shown in Figure 2.15. Again note the discontinuity caused by imposing a hard boundary between the emission processes. This effect is particularly clear for the footpoint source (middle panel) probably due to the fact that the emission here is mostly that from the non-thermal particles escaping from the looptop and not heating.

Obtaining Solar Flare Parameters from a RHESSI CLEAN Image

The main parameters used when calculating density and volume from a CLEAN image are shown in the sketch in Figure 2.16. The cross-sectional area of the loop is assumed to be $A = \pi D^2/4$, with diameter, D, being estimated by first identifying the maximum emission in the lowest energy band and then finding the distance bounded by the 50%

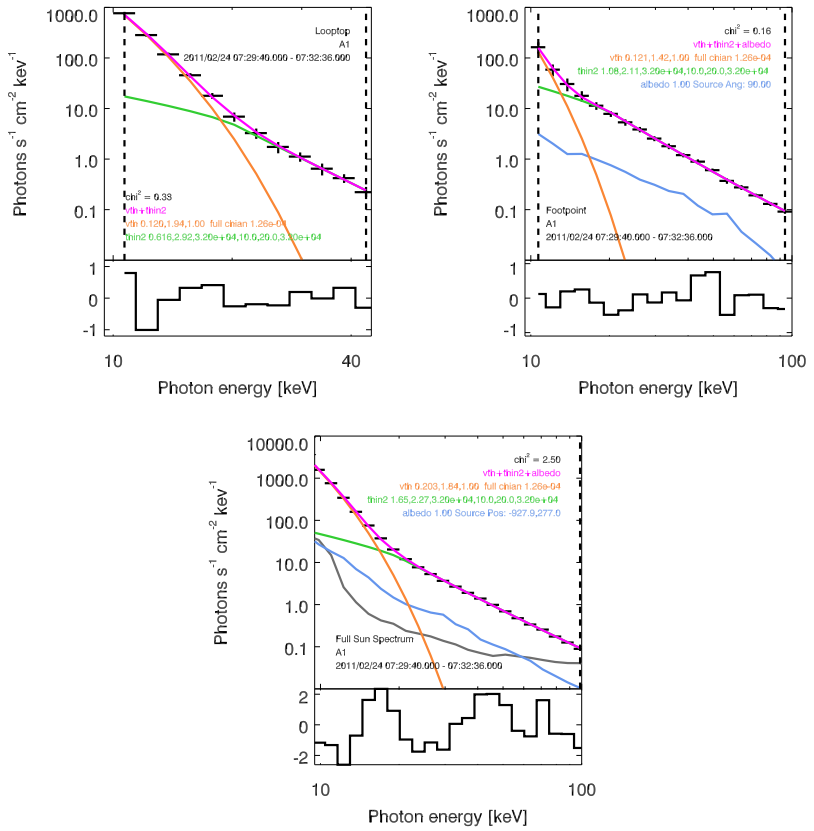

Figure 2.14: Photon X-ray spectra for the 2011 Feb 24 flare: *Left Top*; looptop spectrum, *Right Top*; summed footpoint spectrum and *Bottom*; full-Sun spectrum. HXR spectrum is shown as black data points. Fitting result is shown by the magenta line and is composed of a thermal (orange) and thin-target (green) component, with an albedo correction (blue) for the footpoint and full-Sun spectra. The range fitted for each case is shown by the vertical dashed lines.

contours (red, solid lines) and approximately orthogonal to the loop midline (green dash line). The lowest energy band is used as the emission measure comes from the thermal fit. The thermal volume, $V_{\rm th}$, is then calculated by multiplying the area by the length of the looptop emission, L, which is obtained by approximating the length along the loop midline and again bounded by the 50% contours, i.e. the full width half maximum (FWHM) of the thermal emission. Furthermore, if the source is suitably extended it is possible to split the loop into separate sections in order to examine the emission throughout the source. For example, if the coronal source were split into 5

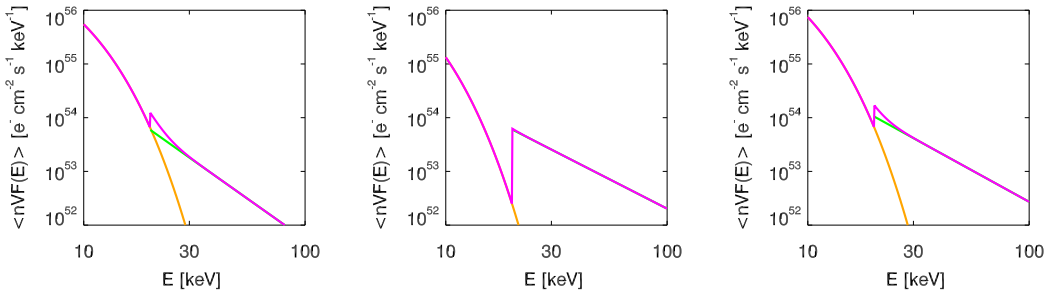

Figure 2.15: Inferred electron density weighted mean electron flux spectra for the 2011 Feb 24 flare: *Left*; looptop flux, *Middle*; summed footpoint flux and *Right*; full-Sun flux. The $\langle nVF(E)\rangle$ for the source from $10-100$ keV is shown by the magenta line and is composed of the thermal (orange) and thin-target (green) $\langle nVF(E)\rangle$.

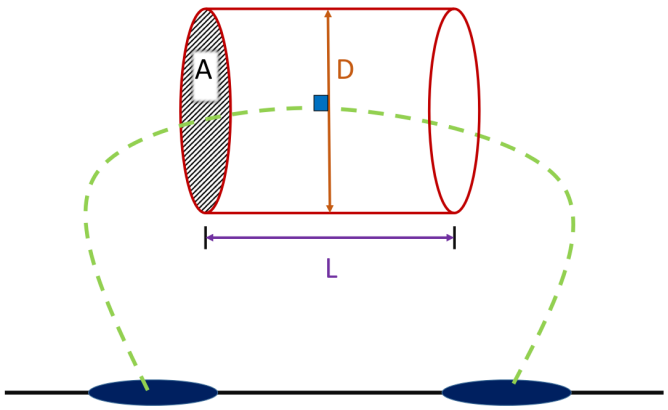

Figure 2.16: Sketch of the important parameters used to calculate $V_{\rm th}$, n_e and L. The chromosphere is shown by the black solid line, with the HXR footpoints shown in blue. The loop midline is shown by the green dashed line. The diameter, D, runs through the maximum emission in the lowest energy band ($10-11.4$ keV for the 2011 Feb 24 flare) and orthogonal to the midline. The length, L, is the distance parallel to the loop midline and bounded by the 50% emission in the lowest energy band, the FWHM of emission in this energy band.

equal length pieces the thermal volume of each piece would be $V_{\rm th}^{\rm sect} = A \times L/5$. This being how the volumes were calculated in Section 2.4.1.

With this approximation to the volume it is possible to obtain an estimate of the mean target proton density, $\bar{n}$, and thus the number density of electrons in the corona, n_e

(assuming $n_{\text{protons}} = n_e$, reasonable for the corona). The thermal fit to the looptop then provides an emission measure, $EM = \bar{n}^2 V$, thus giving $\bar{n} \sim n_e$. This technique is similar to that in Simões & Kontar (2013), except that here the cross sectional area is assumed to be circular and the emission measure from the looptop region is used, not that from the full-Sun spectra. Of course, this calculation assumes that all the plasma within the volume is emitting, i.e. the filling factor is 1. If the filling factor was less than one the inferred density would increase and so any result can be considered a lower limit. The spatial extent of the acceleration region is assumed to be the standard deviation of the full width half maximum as in Xu et al. (2008) and is given by $\sigma = L/2.35$.

The thermal volume is calculated to be $V_{\text{th}} = 6.14 \times 10^{26}$ cm^{-3} which gives a looptop electron density, $n_e = \sqrt{EM/V} = 4.42 \times 10^{10}$ cm^{-3}. The spatial extent of the acceleration region was calculated to be $\sigma = 5.3 \times 10^8$ cm.

2.5 Summary

This Chapter has presented the imaging spectroscopic results of two flares with morphologies applicable to the work of the next two chapters. The results are summarised here:

- *2005 August 23*; the fitted electron distribution changes little throughout the extended source. The looptop density is ∼constant with a value of $\sim 2.5 \times 10^{10}$ cm^{-3}. This agrees well with the inferred density from the full-Sun spectrum (3×10^{10} cm^{-3}) but is a factor of ~ 2 less than that obtained in Jeffrey & Kontar (2013). This could be due to a different estimate of area, the nature of estimating this from CLEAN being inherently more subjective than the same calculations with VisFwdFit. Fitting with a single isothermal function at low energies could also affect the inferred emission measure when compared to the fit in Jeffrey & Kontar (2013) using both emission lines at 6.7 and 8.1 keV. The power-law spectral index is also constant within errors along the length of the loop. There

appears to be a slight trend towards harder spectra at greater distances however, which would be consistent with a core extended acceleration region surrounded by a 'halo' of emission where the escaping high energy particles are collisionally stopped, as postulated by Xu et al. (2008) and Guo et al. (2012).

- *2011 February 24*: This flare has the most commonly observed coronal loop with HXR footpoint morphology. It displays a looptop photon spectrum that is relatively hotter and softer than that from the footpoint. The fits performed are consistent with the full-Sun spectrum and agree well with those in Simões & Kontar (2013). It shows the same behaviour observed in Yohkoh flares (Petrosian et al., 2002) and consequently with RHESSI (see e.g. Emslie et al., 2003; Battaglia & Benz, 2006) where the looptop spectrum is not softer by a factor of 2 which would be expected in the thick-target model (Brown, 1971). This implies some kind of extra trapping during the transport of electrons which would seem to corroborate the work of Kontar et al. (2014) who found the electron rates at the looptop were higher than that needed to explain the observed footpoint emission. This could be due to magnetic turbulence, inferred to explain the scaling of loop widths with energy by Kontar et al. (2011a) and Bian et al. (2011). This causes efficient pitch-angle scattering resulting in electrons being confined to the looptop region for longer.

  The fits to this flare provide initial conditions for the numerical modelling of Chapter 4 by creating a model corona of temperature 23 MK and density, $n_e = 4.42 \times 10^{10}$ cm^{-3}, with an acceleration region extent defined as $\sigma = 5.3 \times 10^{8}$ cm.

In the next chapter the subject of kappa distributions in solar flares will be studied. Specific conditions, like those seen in the 2005 August 23 flare, can create a scenario where a stochastic acceleration model admits a kappa distribution. These distributions are interesting in a solar flare context due to their shape approximating that observed in the HXR range in flares with no need for two separate populations of electrons, or (possibly) artificial low energy cutoffs.

Chapter 3

Kappa Distributions in Solar Flares

This work is part of a collaboration published in Bian et al. (2014), my unique contribution being the numerical modelling

3.1 Introduction to the Chapter

RHESSI has revealed hard X-ray sources, such as the 2005 August 23 flare studied in the previous chapter (Section 2.4.1), where the ambient density within the coronal loop is high enough such that the electrons are collisionally stopped within the loop and the emission is confined to the corona with negligible numbers of electrons escaping to the lower solar atmosphere (Jeffrey & Kontar, 2013). They are seen to have a core acceleration region surrounded by a 'halo' of escaping particles, as discussed by Xu et al. (2008). A major objective of contemporary high-energy solar physics is to understand not just the propagation of particles but also the physics of the acceleration. Events such as that studied in this chapter are particularly interesting in this respect as the coincidence of the acceleration of electrons together with the emission of hard X-ray photons means that they are ideal for determining the length of, and the density within, the acceleration region (Kontar et al., 2011b; Guo et al., 2013). Knowledge of these values can be used to obtain the specific acceleration rate, $\gamma = \dot{N}/N$ [e^- s^{-1} per ambient e^-] (Emslie et al., 2008; Guo et al., 2013), where N is the number of particles

and $\dot{N}$ is the derivative with respect to time. This quantity determines the efficiency of the acceleration process.

As already mentioned, there is growing observational evidence that the accelerated electron distribution is almost isotropic in pitch-angle (Kontar & Brown, 2006). RHESSI imaging spectroscopy also suggests the presence of turbulence, possibly due to fluctuations in the magnetic field, as discussed in Kontar et al. (2011a). This leads to pitch-angle scattering (Kontar et al., 2014) and cross field transport (Bian et al., 2011) of high energy electrons. Further to this, acceleration by DC fields, whether super- or sub-Dreicer, faces serious challenges in terms of the properties of the source in order to avoid large unidirectional currents (Holman, 1985; Emslie & Henoux, 1995). Consideration of the above points would seem to favour a stochastic acceleration process (see Chapter 1 Section 1.2 and Miller et al. (1997); Petrosian (2012); Bian et al. (2012) for reviews). Stochastic acceleration has been applied to flares (Parker & Tidman, 1958; Ramaty, 1979; Miller et al., 1996; Petrosian & Chen, 2010) where the models often share the property that they can be described by the turbulent diffusion coefficient, D_{vv}.

In this chapter, driven by the discussion above, a stochastic model where the acceleration is controlled by a turbulent diffusion coefficient, D_{vv}, in a regime with coulomb collisional effects in an acceleration region that is essentially a coronal thick-target is studied. The shape of any eventual distribution will be governed by the balance of timescales within this system. Each term within the model (the evolution of which is controlled by a Fokker-Planck equation) has an associated timescale over which it has an effect. Within the system put forward here, there are four: the acceleration timescale, $\tau_{\rm acc}(v)$, the collisional deceleration/friction timescale, $\tau_{\rm c}(v)$, the collisional diffusion timescale, $\tau_{\rm diff}(v)$, and the escape timescale, $\tau_{\rm esc}(v)$. In the range of velocity where the acceleration region can be considered a thick-target, escape will have no effect and the shape of the distribution will converge to a steady-state solution governed by the balance of acceleration and collisional effects. If the diffusion coefficient behaves inversely proportional to v, i.e. $D_{vv} \sim 1/v$, then the resulting steady-state form is that of a kappa distribution, transitioning smoothly from a low energy Maxwellian

core to a high energy power-law tail (Tsytovich, 1966; Benz, 1977; Leubner, 2004). Kappa distributions are encouraging in a solar flare context as they approximate the shape of the inferred electron distribution (e.g. Holman et al., 2003) without the need for two populations of electrons and a (possibly artificial) low-energy cutoff. Kappa distributions related to solar flares have been discussed by other authors, for example Kašparová & Karlický (2009); Oka et al. (2013).

The chapter is split as follows: the general acceleration model is described in the next Section (3.2). Section 3.3 shows the steady-state solution when $D_{vv} \sim 1/v$. The solution taking the form of a kappa-distribution which is characterized by a typical velocity scale (e.g. the thermal velocity associated with the Maxwellian core) and the dimensionless ratio of the acceleration and collisional timescales. The evolution to this final, steady state is discussed in Section 3.4, where the acceleration proceeds as a 'wavefront' in velocity space with $\tau_{\rm acc} \sim E^{3/2}$. The approximations used to examine this evolution are corroborated by the numerical results of Section 3.5. The solution in the limit of small escape where the looptop acceleration region is essentially thick-target is shown in Section 3.6. In Section 3.7 a simple model involving the acceleration via large scale coherent electric fields is shown. In the presence of efficient pitch angle scattering leading to the isotropization of the distribution function this acceleration produces an effect akin to stochastic acceleration. The conditions for $D_{vv} \sim 1/v$ are discussed and this imposes constraints on the strength of the accelerating electric field. The chapter is summarized in Section 3.8.

3.2 The Model

The aim here was to develop a model for the three-dimensional (in velocity), isotropic (in pitch angle), electron distribution, $f(\mathbf{v}, t)$ (normalized such that $n_\kappa = \int f 4\pi v^2 dv$ [cm^{-3}]), within a thick-target coronal looptop source. A Fokker-Planck equation is used that includes turbulent acceleration and coulomb collisions within in a dense solar atmo-

sphere,

$$\frac{\partial f}{\partial t} = \frac{1}{v^2}\frac{\partial}{\partial v}\left\{v^2\left[\left(\frac{\Gamma\, v_{\rm te}^2}{2v^3} + D_{\rm turb}(v)\right)\frac{\partial f}{\partial v} + \frac{\Gamma}{v^2}\, f\right]\right\} \quad , \tag{3.1}$$

where the parameters are as defined in Table of Symbols and $D_{\rm turb}(v) \equiv D_{vv}$ is the diffusion coefficient in velocity space with dependence not yet defined, $v_{\rm te}$ is the thermal velocity of background electrons (equation 1.17) and $\Gamma = 4\pi e^4 n_e \ln\Lambda/m_e^2$ is the collisional parameter (equation 1.10 with $Z = 1$ for the corona). It should be noted a simplified version of the collisional operator, valid for the solar flare situation, has been used here (Jeffrey et al., 2014). The electrons are modelled as being in contact with a heat bath at a constant temperature, T. In Chapter 1 there is discussion of the timescales that acceleration, collisions and transport operate on. Following this, the three timescales intrinsic within the above equation are:

- the *acceleration time*, $\tau_{\rm acc}$, which can be obtained by approximating $\partial v \sim v$,

$$\frac{1}{v^2}\frac{\partial}{\partial v}\left\{v^2\left[D_{\rm turb}(v)\frac{\partial f}{\partial v}\right]\right\} \simeq \frac{1}{v^2}\frac{1}{v}v^2 D_{\rm turb}(v)\frac{f}{v} = \frac{f}{\tau_{\rm acc}(v)}, \tag{3.2}$$

  where,

$$\tau_{\rm acc}(v) = \frac{v^2}{D_{\rm turb}(v)}; \tag{3.3}$$

- the *collisional deceleration/friction time*, $\tau_{\rm c}$, defined by,

$$\frac{\Gamma}{v^2}\frac{\partial f}{\partial v} \simeq \frac{f}{\tau_{\rm c}(v)} \quad ; \quad \tau_{\rm c}(v) \simeq \frac{v^3}{\Gamma}, \qquad \text{and;} \tag{3.4}$$

- the *collisional diffusion time*, $\tau_{\rm diff}$, defined by,

$$\frac{1}{v^2}\frac{\partial}{\partial v}\left\{v^2\left[\frac{\Gamma v_{te}^2}{2v^3}\frac{\partial f}{\partial v}\right]\right\} \simeq \frac{f}{\tau_{\rm diff}(v)} \quad ; \quad \tau_{\rm diff}(v) \simeq \frac{2v^5}{\Gamma v_{\rm te}^2}. \tag{3.5}$$

The balance between these three timescales controls the shape of any accelerated electron distribution, as mentioned in Chapter 1 Section 1.4.

Equation (3.1) is recast in the form of Chavanis & Lemou (2005) as it provides a clearer insight into the properties of the distribution,

$$\frac{\partial f}{\partial t} = \frac{1}{v^2}\frac{\partial}{\partial v}\left[v^2 D(v)\left(\frac{\partial f}{\partial v} + f U'(v)\right)\right], \tag{3.6}$$

where grouping together the diffusive terms,

$$D(v) = \frac{\Gamma v_{\rm te}^2}{2v^3} + D_{\rm turb}(v), \tag{3.7}$$

and,

$$U'(v) = \frac{\Gamma}{v^2 D(v)} = \left(\frac{v_{\rm te}^2}{2v} + \frac{v^2 D_{\rm turb}(v)}{\Gamma} \right)^{-1}. \tag{3.8}$$

Observations of solar flares are generally limited by the instrument temporal resolution. For RHESSI this is the time it takes to create a full set of spatial Fourier components of the source (see Chapter 1 Section 1.6.2, Chapter 2 Section 2.2 and Kontar et al. 2011b) which is at least 1 rotation, $\sim$ 4 s. Since typical timescales for acceleration, collisions and escape are less than a second in a typical coronal HXR source (Guo et al., 2013) this means that a steady-state solution to equation (3.6) is pertinent here. The solution to equation (3.6) when $\partial/\partial t = 0$ is (Chavanis & Lemou, 2005),

$$f(v) = A\, \mathrm{e}^{-U(v)}. \tag{3.9}$$

This solution is general enough to find the energetic particle distribution, $f(v)$, in a collisional plasma. The exact shape of this distribution will depend on the choice of $D_{\rm turb}(v)$ or equivalently the function $U(v)$.

3.3 The Kappa Distribution Stationary Solution

Observations of solar flares show that the distribution of particles producing the X-ray spectrum is generally best fit as a thermal core with a power-law (or broken power-law) tail (Lin et al., 1981; Holman et al., 2003; Battaglia & Benz, 2006; Kontar et al., 2011b; Simões & Kontar, 2013). In order to satisfy this constraint on the accelerated electron distribution the turbulent diffusion coefficient is chosen so as to be inversely proportional to v, i.e.

$$D_{\rm turb} = \frac{D_0}{v}, \tag{3.10}$$

where D_0 is a constant approximating the level of turbulence. With this choice of diffusion coefficient the model (equation 3.6) will be shown to produce a kappa distribution steady-state solution, which has the form of a thermal core and power-law

tail. Of course, due to the fact that $D_{\rm turb}$ is inversely proportional to v, this expression diverges for small velocities and as such it may be less accurate for low speeds. It results in an acceleration timescale (equation 3.3),

$$\tau_{\rm acc} = \frac{v^3}{D_0}. \tag{3.11}$$

This is important as it means that at high enough energies both the acceleration timescale and the collisional timescale scale as v^3, meaning that there is no dominant process in the system. Hence, at these energies the distribution is governed by the balance between acceleration and collisions and this is what enables the power-law tail to form. The choice of $D_{\rm turb}$ above allows the definition of the dimensionless constant,

$$\kappa = \frac{\tau_{\rm acc}}{2\tau_{\rm c}} = \frac{\Gamma}{2D_0}, \tag{3.12}$$

(the reasoning for the factor 2 will become clear). This means that the function $U'(v)$ (equation 3.8) can be rewritten,

$$\begin{aligned} U'(v) &= \left(\frac{v_{\rm te}^2}{2v} + \frac{v^2}{\Gamma}\frac{D_0}{v}\right)^{-1}, \\ &= \left(\frac{v_{\rm te}^2}{2v} + \frac{2D_0}{\Gamma}\frac{v}{2}\right)^{-1}, \\ &= \left(\frac{v_{\rm te}^2}{2v} + \frac{1}{\kappa}\frac{v}{2}\right)^{-1}, \\ &= \left[\frac{v_{\rm te}^2}{2v}\left(1 + \frac{1}{\kappa}\frac{v^2}{v_{\rm te}^2}\right)\right]^{-1}, \end{aligned}$$

finally leading to,

$$U'(v) = \frac{2v}{v_{\rm te}^2}\left(1 + \frac{1}{\kappa}\frac{v^2}{v_{\rm te}^2}\right)^{-1}. \tag{3.13}$$

To obtain $U(v)$ the above expression is integrated over v, so,

$$U(v) = \int_0^{v^2/\kappa v_{\rm te}^2} \frac{2v}{v_{\rm te}^2}\left(1 + \frac{1}{\kappa}\frac{v^2}{v_{\rm te}^2}\right)^{-1} dv. \tag{3.14}$$

Making the change of variables $v^2/\kappa v_{\rm te}^2 = g \implies (2v/\kappa v_{\rm te}^2)dv = dg$ and thus $\kappa dg = (2v/v_{\rm te}^2)dv$, giving the integral,

$$U(g) = \int_0^g \kappa\,(1+g)^{-1}\,dg. \tag{3.15}$$

This is a standard integral, which means,

$$U(g) = \kappa \ln(1+g). \tag{3.16}$$

Now, changing variables back to v gives,

$$U(v) = \kappa \ln\left(1 + \frac{v^2}{\kappa v_{\rm te}^2}\right). \tag{3.17}$$

Equation (3.17) can be inserted into equation (3.9) giving, with appropriate choice of normalising factor,

$$f_\kappa(v) = \frac{n_\kappa}{\pi^{3/2} v_{\rm te}^3 \kappa^{3/2}} \frac{\Gamma(\kappa)}{\Gamma(\kappa - 3/2)} \left(1 + \frac{v^2}{\kappa v_{\rm te}^2}\right)^{-\kappa}. \tag{3.18}$$

This distribution is in the form of what is known as a κ distribution of the first kind in the terminology of Livadiotis & McComas (2009) (their equation 9). Kašparová & Karlický (2009) and Oka et al. (2013) study a κ distribution of the second kind (again using nomenclature of Livadiotis & McComas (2009)), it is easily seen that with the simple change of variables,

$$\tilde{\kappa} = \kappa - 1; \quad \theta = \sqrt{\frac{\kappa}{\kappa - 1}} v_{\rm te}, \tag{3.19}$$

the κ distribution of the first kind becomes a κ distribution of the second kind, that is,

$$f_{\tilde{\kappa}}(v) = \frac{n_{\tilde{\kappa}}}{\pi^{3/2} \theta^3 \tilde{\kappa}^{3/2}} \frac{\Gamma(\tilde{\kappa}+1)}{\Gamma(\tilde{\kappa} - 1/2)} \left(1 + \frac{v^2}{\tilde{\kappa}\theta^2}\right)^{-(\tilde{\kappa}+1)}, \tag{3.20}$$

which is equation (10) in Livadiotis & McComas (2009). In Bian et al. (2014) it is argued that the kappa distribution of the first kind is more pertinent in a solar flare context. This is due to the physical nature of the κ obtained. It is the dimensionless ratio of the stochastic acceleration timescale, $\tau_{\rm acc}$, to the collisional deceleration timescale, $\tau_{\rm c}$, or equivalently the collisional parameter, Γ, and the diffusion coefficient, D_0.

Figure 3.1 shows how the kappa distribution, equation (3.18), behaves with different values of κ. If κ has a large value the identity,

$$\lim_{\kappa \to \infty} \left(1 + \frac{x}{\kappa}\right)^{-\kappa} = \exp(-x), \tag{3.21}$$

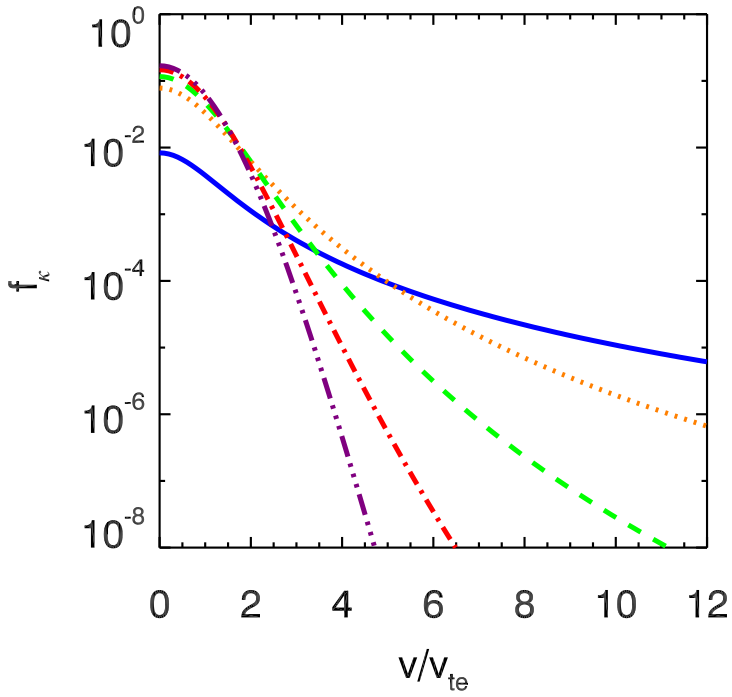

Figure 3.1: The stationary solution kappa distribution, f_κ, for different values of κ, all normalized to a density $n_\kappa = 1$. *Solid blue line;* $\kappa = 1.6$, *dotted orange line;* $\kappa = 3$, *dashed green line;* $\kappa = 5$, *dot-dashed red line;* $\kappa = 10$, *dot-dot-dot-dashed purple line;* $\kappa = 30$. For small values of κ the distribution function has a Maxwellian core and a non-thermal power-law tail, while for large values of κ the distribution is almost indistinguishable from a Maxwellian.

means that the kappa distribution in equation (3.18) approaches the form,

$$f_\kappa(v) \sim \exp\left(-\frac{v^2}{v_{\rm te}^2}\right), \tag{3.22}$$

which is a Maxwellian (see $\kappa = 30$ in figure 3.1).

At low velocities, $v \ll \sqrt{\kappa} v_{\rm te}$, the collisional diffusion term, $f/\tau_{\rm diff} \sim v^{-5}$, is dominant over the turbulent and collisional terms, $f/\tau_{\rm acc} \sim f/\tau_{\rm c} \sim v^{-3}$, which results in the distribution relaxing through diffusion to a Maxwellian form. In this low velocity regime the term in brackets in equation (3.18) can be approximated as,

$$\left(1 + \frac{v^2}{\kappa v_{\rm te}^2}\right)^{-\kappa} \sim \left(1 - \frac{\kappa v^2}{\kappa v_{\rm te}^2}\right) \sim \left(1 - \frac{v^2}{v_{\rm te}^2}\right). \tag{3.23}$$

So the kappa distribution itself approaches the form,

$$f(v) \sim \left(1 - \frac{v^2}{v_{\rm te}^2}\right) \quad \text{as} \quad v \to 0, \tag{3.24}$$

which is the low energy limit of the Maxwellian distribution. In the high velocity limit, $v \gg \sqrt{\kappa} v_{\rm te}$, the collisional diffusion timescale, $\tau_{\rm diff}$ (equation 3.5), is much longer than either the turbulent timescale, $\tau_{\rm acc}$ (equation 3.3), or the collisional deceleration time, $\tau_{\rm c}$ (equation 3.4). As such, at high velocities, the collisional diffusion term is unimportant. Furthermore, because both $\tau_{\rm acc}$ and $\tau_{\rm c}$ have the same dependence on velocity (v^3) there is no longer a characteristic velocity scale in the system. Equation (3.18) again confirms that in the high velocity limit,

$$f \sim \left(1 + \frac{v^2}{\kappa v_{\rm te}^2}\right)^{-\kappa} \sim v^{-2\kappa} \quad \text{as} \quad v \to \infty, \tag{3.25}$$

the stationary solution approaches a power-law.

Thus, at low velocities the distribution has a Maxwellian core and at high velocities the distribution approaches a power-law so the whole particle distribution is kappa in form. Kappa distributions are interesting in a solar flare context as they account for the observed spectral shape, the Maxwellian core and power-law tail, without the need for a (possibly artificial) low energy cutoff, instead smoothly transitioning from the Maxwellian core to the high energy power-law tail. It should be noted that in general a single kappa distribution cannot satisfactorily fit the spatially integrated full-Sun spectra observed by RHESSI as mentioned by Kašparová & Karlický (2009). The authors did find that some coronal sources could be adequately fit by the thin-target emission from a kappa distribution however.

The electron velocity distribution, $f(v)$, used here is related to the mean electron flux, $\bar{F}(E)$ [e$^-$ cm^{-2} s^{-1} per unit energy], by the simple relation $vf(v)d^3v = \bar{F}(E)dE$. For typical photon HXR energies studied here ($\leq$ 100 keV) it can be assumed that $E = m_e v^2/2$ holds as an approximation. Although strictly, as discussed in Chapter 1 Section 1.5.1, relativistic effects should be taken account at energies as low as 30 keV. Now, $vd^3v \sim v^3 dv$ and so $f(v)v^3 dv \sim \bar{F}(E)dE$ which means $f(v)Evdv \sim \bar{F}(E)vdv$ (as $dE = m_e vdv$) which finally leads to the relation $f(v) \sim \bar{F}(E)/E$. The mean electron flux is thus $\bar{F}(E) \sim E^{-\delta}$, with $\delta = \kappa - 1$.

Analysis of the non-thermal spectrum above 20 keV in solar flares has shown that in many cases the photon spectrum is approximately a power-law (Holman et al., 2003),

$I(\epsilon) \sim \epsilon^{-\gamma}$ [photons cm^{-2} s^{-1} keV^{-1}], where ϵ [keV] is the photon energy and γ is the photon spectral index, typically $\simeq 5$. The hard X-ray spectrum was discussed in Chapter 1 and at earth is given by (Brown et al., 2003; Kontar et al., 2011b),

$$I(\epsilon) = \frac{nV}{4\pi R^2} \int_{\epsilon}^{\infty} \bar{F}(E) Q(\epsilon, E) dE, \tag{3.26}$$

where V is the source volume, R is the distance from the source, i.e. 1 A.U. and $Q(\epsilon, E)$ is the bremmstrahlung cross section [cm^2 keV^{-1}] which is differential in photon energy. The simple non-relativistic Kramer's cross section (equation 1.34) can be used as an illustration,

$$Q(\epsilon, E) \sim \frac{1}{\epsilon E}. \tag{3.27}$$

So, substituting in the power law forms and equation (3.27) into equation (3.26) gives,

$$\epsilon^{-\gamma} \sim \int_{\epsilon}^{\infty} \frac{E^{-\delta}}{\epsilon E} dE, \tag{3.28}$$

which integrated gives,

$$\epsilon^{-\gamma} \sim \epsilon^{-(\delta+1)}. \tag{3.29}$$

The relationship between the photon spectral index and the electron spectrum slope is thus $\delta = \gamma - 1$. Of course, integrating a non-relativistic cross section to infinite energy is unrealistic but the argument above also holds for more complicated cross-sections, such as the Bethe-Heitler cross-section used in Brown (1971) and shown in Chapter 1 (equation 1.35). This is due to the fact that $Q(\epsilon, E)$ is still proportional to $1/\epsilon E$ in this case.

From the discussion above $\delta = \kappa - 1 = \gamma - 1$, i.e. the index in the stationary kappa distribution and the photon spectral index are equal,

$$\kappa = \gamma, \tag{3.30}$$

and as such, in a solar flare context a typical value for κ would be 5. Furthermore, the definition of the parameter κ (equation 3.12) provides the relative magnitude of two of the timescales in the system,

$$\tau_{\rm acc} = 10\tau_{\rm c}. \tag{3.31}$$

So in a coronal hard X-ray source, conducive to producing a kappa distribution, the acceleration timescale would be expected to be approximately an order of magnitude larger than the collisional deceleration/friction time.

Due to the dependence of κ on the acceleration timescale, $\tau_{\rm acc}$, this means that a time dependent hardening or softening of the accelerated electron spectrum could be the result of a variation of the turbulent diffusion coefficient, D_0, over a timescale much longer than the relaxation to the steady state. This has been mentioned before by Benz (1977); Grigis & Benz (2006) in order to explain the observed soft-hard-soft, or soft-hard-harder, behaviour of observations of the X-ray spectrum during solar flares.

3.4 Evolution Toward the Steady-State Distribution

To study the evolution towards the final steady state, $f_\kappa(v)$, the function,

$$u(v,t) = \frac{f(v,t)}{f_\kappa(v)}, \tag{3.32}$$

is introduced. By substituting this into equation (3.6) the evolution of the dimensionless function $u(v,t)$ can be examined,

$$\frac{\partial(u(v,t)f_\kappa(v))}{\partial t} = \frac{1}{v^2}\frac{\partial}{\partial v}\left[v^2 D(v)\left(\frac{\partial(u(v,t)f_\kappa(v))}{\partial v} + u(v,t)f_\kappa(v)U'(v)\right)\right]. \tag{3.33}$$

The evolution of $u(v,t)$ can thus be described as,

$$\frac{\partial u}{\partial t} = \frac{1}{v^2}\frac{\partial}{\partial v}\left(v^2 D(v)\frac{\partial u}{\partial v}\right) - D(v)U'(v)\frac{\partial u}{\partial v}. \tag{3.34}$$

The velocity space variable, η, is now introduced via (Chavanis & Lemou, 2005),

$$d\eta = \frac{dv}{\sqrt{D(v)}}, \tag{3.35}$$

thus,

$$\frac{\partial}{\partial v} = \frac{\partial}{\partial \eta}\frac{\partial \eta}{\partial v} = \frac{1}{\sqrt{D(v)}}\frac{\partial}{\partial \eta}. \tag{3.36}$$

So, changing partial derivatives from ∂v to $\partial \eta$ in equation (3.34) gives,

$$\frac{\partial u}{\partial t} = \frac{1}{v^2\sqrt{D(v)}}\frac{\partial}{\partial \eta}\left(v^2\sqrt{D(v)}\frac{\partial u}{\partial \eta}\right) - \sqrt{D(v)}U'(v)\frac{\partial u}{\partial \eta}. \tag{3.37}$$

Differentiating (with respect to η) by the chain rule,

$$\frac{\partial u}{\partial t} = \frac{1}{v^2\sqrt{D(v)}}\left[2v\frac{\partial v}{\partial \eta}\sqrt{D(v)}\frac{\partial u}{\partial \eta} + v^2\frac{D(v)^{-1/2}}{2}\frac{\partial v}{\partial \eta}\frac{\partial D(v)}{\partial v}\frac{\partial u}{\partial \eta} + v^2\sqrt{D(v)}\frac{\partial^2 u}{\partial \eta^2}\right] - \sqrt{D(v)}U'(v)\frac{\partial u}{\partial \eta}. \tag{3.38}$$

Now with some rearranging,

$$\frac{\partial u}{\partial t} = \frac{2}{v}\sqrt{D(v)}\frac{\partial u}{\partial \eta} + \frac{1}{2}\frac{\sqrt{D(v)}}{D(v)}\frac{\partial D(v)}{\partial v}\frac{\partial u}{\partial \eta} + \frac{\partial^2 u}{\partial \eta^2} - \sqrt{D(v)}U'(v)\frac{\partial u}{\partial \eta}. \tag{3.39}$$

Grouping the first order derivatives,

$$\frac{\partial u}{\partial t} = \frac{\partial^2 u}{\partial \eta^2} + \sqrt{D(v)}\left[\frac{2}{v} + \frac{1}{2}\frac{1}{D(v)}\frac{\partial D(v)}{\partial v} - U'(v)\right]\frac{\partial u}{\partial \eta}. \tag{3.40}$$

This means that the equation (3.34) can be recast as an advection-diffusion equation in velocity space,

$$\frac{\partial u}{\partial t} + V(v)\frac{\partial u}{\partial \eta} = \frac{\partial^2 u}{\partial \eta^2}, \tag{3.41}$$

where the advection speed is given by the expression,

$$V(v) = \sqrt{D(v)}\left[U'(v) - \frac{2}{v} - \frac{1}{2}\frac{d\ln D(v)}{dv}\right], \tag{3.42}$$

the logarithmic term coming from the second term within the brackets in equation (3.40). The left hand side of equation (3.41) corresponds to an advection by a velocity field, $V(v)$, and the right hand side corresponds to a diffusion. The acceleration of particles is dependent on the advection speed, and as such those at lower energies will be accelerated first. That is, the relaxation to the final steady-state kappa distribution, f_κ, proceeds such that lower energies approach the asymptotic form first, with the higher energies later. This can be characterised as a 'front' with position $v_\mathrm{f}(t)$ moving towards higher energies in velocity space (MacDonald et al., 1957; Chavanis & Lemou, 2005). In order to estimate the position of this front, the diffusive term in equation (3.41) is neglected, thus,

$$\frac{\partial u}{\partial t} + V(v_\mathrm{f})\frac{\partial u}{\partial \eta} = 0. \tag{3.43}$$

To find the approximate location of the 'front' $u\,(=f/f_\kappa)$ is set to a constant value (arbitrarily choose $u = 0.7$ in Section 3.5). So, the total derivative,

$$\frac{du}{dt} \equiv \frac{\partial u}{\partial t} + \frac{d\eta}{dt}\frac{\partial u}{\partial \eta} = 0. \tag{3.44}$$

It follows that,

$$V(v_\mathrm{f}) = \frac{d\eta}{dt} = \frac{1}{\sqrt{D(v_\mathrm{f})}}\frac{dv_\mathrm{f}}{dt}, \tag{3.45}$$

from equation (3.35). The expression for $V(v_\mathrm{f})$ can now be written explicitly (equation 3.42) so,

$$\frac{dv_\mathrm{f}}{dt} = D(v_\mathrm{f})\left[U'(v_\mathrm{f}) - \frac{2}{v_\mathrm{f}} - \frac{1}{2v_\mathrm{f}}\frac{d\ln D(v_\mathrm{f})}{d\ln v_\mathrm{f}}\right], \tag{3.46}$$

where switching from dv_f to $d\ln v_\mathrm{f}$ results in the requirement of the extra factor v_f in the last term. In the high velocity regime $D(v) \sim D_\mathrm{turb}(v) = D_0/v$ so that $d\ln D(v_\mathrm{f})/d\ln v_\mathrm{f} \sim -1$. Furthermore, from equation (3.17),

$$U'(v) \sim 2v(\kappa^{-1}v^2)^{-1} = \frac{2\kappa}{v}. \tag{3.47}$$

So for $v \gg v_\mathrm{te}$ equation (3.46) becomes,

$$\frac{dv_\mathrm{f}}{dt} = D(v_\mathrm{f})\left[\frac{2\kappa}{v_\mathrm{f}} - \frac{2}{v_\mathrm{f}} + \frac{1}{2v_\mathrm{f}}\right], \tag{3.48}$$

which is, when taking out the common factor $1/v_\mathrm{f}$,

$$\frac{dv_\mathrm{f}}{dt} = \frac{D(v_\mathrm{f})}{v_\mathrm{f}}\left[2\kappa - \frac{3}{2}\right]. \tag{3.49}$$

Now, using equation (3.12) and the fact that in the high velocity regime $D(v_\mathrm{f}) \sim D_0/v_\mathrm{f}$ this gives,

$$\begin{aligned}\frac{dv_\mathrm{f}}{dt} &= \frac{D_0}{v_\mathrm{f}^2}\left[\frac{\Gamma}{D_0} - \frac{3}{2}\right], \\ &= \frac{\Gamma}{v_\mathrm{f}^2}\left[1 - \frac{3D_0}{2\Gamma}\right] \quad \text{and so,} \\ \frac{dv_\mathrm{f}}{dt} &= \Gamma\left[1 - \frac{3}{4\kappa}\right]\frac{1}{v_\mathrm{f}^2}.\end{aligned} \tag{3.50}$$

This is a separable differential equation which means,

$$\int v_\mathrm{f}^2 dv_\mathrm{f} = \int \Gamma\left[1 - \frac{3}{4\kappa}\right] dt. \tag{3.51}$$

If it is assumed that $v_{\rm f}(t=0)=0$, this leads to,

$$v_{\rm f} = \left[1-\frac{3}{4\kappa}\right]^{1/3}(3\Gamma t)^{1/3}. \tag{3.52}$$

Of course, as this is a long time approximation, to talk about the front speed at $t=0$ may seem incongruous. The front structure will not have formed at this time however, and as such can be assumed to be at zero velocity. If $\tau_{\rm c}^{\rm th}=v_{\rm te}^3/\Gamma$ is now defined as the collisional timescale of a thermal electron this means,

$$v_{\rm f} \simeq v_{\rm te}\left(\frac{t}{\tau_{\rm c}^{\rm th}}\right)^{1/3}. \tag{3.53}$$

Now, the thermal collisional timescale can be expressed as,

$$\tau_{\rm c}^{\rm th} = \frac{v_{\rm te}^3}{\Gamma} = \frac{(2k_{\rm b}T)^{3/2}m_{\rm e}^{1/2}}{4\pi e^4 n\ln\Lambda} \simeq 4\times10^{-3}\frac{T^{3/2}}{n}. \tag{3.54}$$

If typical values for a dense flaring loop are $T=2\times10^7$ K and $n=1\times10^{11}$ cm^{-3} then $\tau_{\rm c}^{\rm th}\simeq 3$ ms. A typical hard X-ray producing electron has energy, $E=30$ keV, which is about 15 times the thermal energy in the corona, so from equation (3.53),

$$t=\tau_{\rm c}^{\rm th}\left(\frac{v_{\rm f}}{v_{\rm te}}\right)^3=\tau_{\rm c}^{\rm th}\left(\frac{E_{\rm f}}{E_{\rm te}}\right)^{3/2}, \tag{3.55}$$

where $E_{\rm f}$ is the position of the front in energy space and $E_{\rm te}$ is the thermal energy. This means the average time taken to accelerate an electron to this energy is $t\sim 15^{3/2}\tau_{\rm c}^{\rm th}\simeq 0.2$ s. This is comparable to the hard X-ray rise and decay during solar flare observations. Note that this is not the acceleration timescale as discussed before (equation 3.3), this is the time taken for the 'front' discussed above to reach a typical HXR producing energy. This can be used as an approximation for the average time taken for the model to produce an electron of this energy. Equation (3.3), on the other hand, is the timescale on which the acceleration term effects changes to the particle distribution. The natural question here is whether the electrons can be confined to the acceleration region for long enough to produce the asymptotic steady state distribution, which will be tackled in Section 3.6. Finally, it is again noted that this is a long time approximation, the assumptions above require that enough particles have been accelerated to non-thermal energies to be valid.

3.5 Numerical Solutions

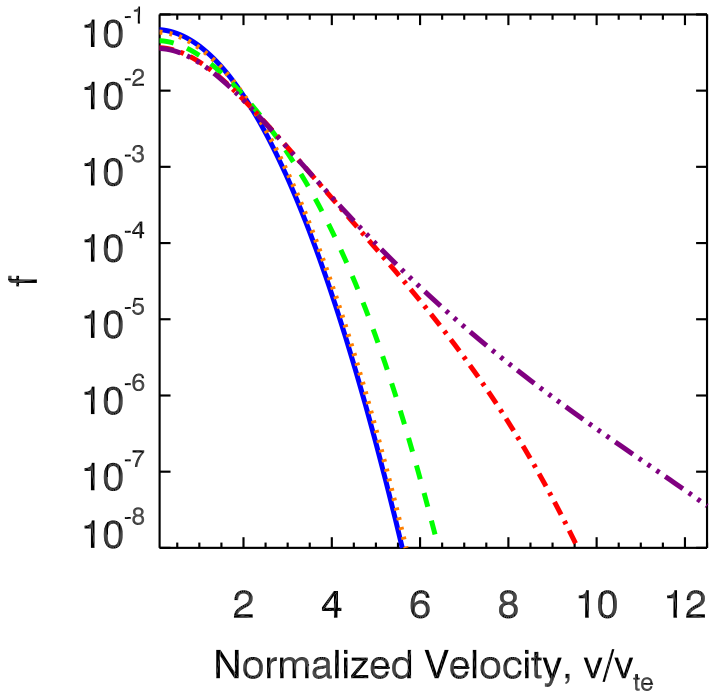

Figure 3.2: Temporal evolution of the electron distribution function, $f(v,t)$, for $\kappa\,(\equiv \Gamma/2D_0) = 5$. The solid blue line shows the initial Maxwellian and then, from left to right, $f(v,t)$ at $t/\tau_c^{\rm th} = 1$ (orange dotted line), $t/\tau_c^{\rm th} = 10$ (green dashed line), $t/\tau_c^{\rm th} = 100$ (red dot-dashed line), and $t/\tau_c^{\rm th} = 1000$ (purple triple dot-dashed line).

A number of numerical solutions of the Fokker-Planck equation (3.1) were performed in order to confirm the analytic expressions obtained in Section 3.4. Using a finite difference code (Kontar, 2001), the evolution of $f(v,t)$ from an originally thermal, Maxwellian distribution was examined with the turbulent diffusion coefficient defined as in equation (3.10). A value of $\kappa = 5$ is chosen as this agrees well with solar flare observations (see discussion in Section 3.3). The choice of kappa will affect the shape of the final distribution but the results will be similar to those here, the parameter κ basically being the relative strength of the acceleration and collisional processes (equation 3.12). The simulations were run until a steady state was reached. In order to ensure the validity of the numerical results two checks were performed: first, as particle

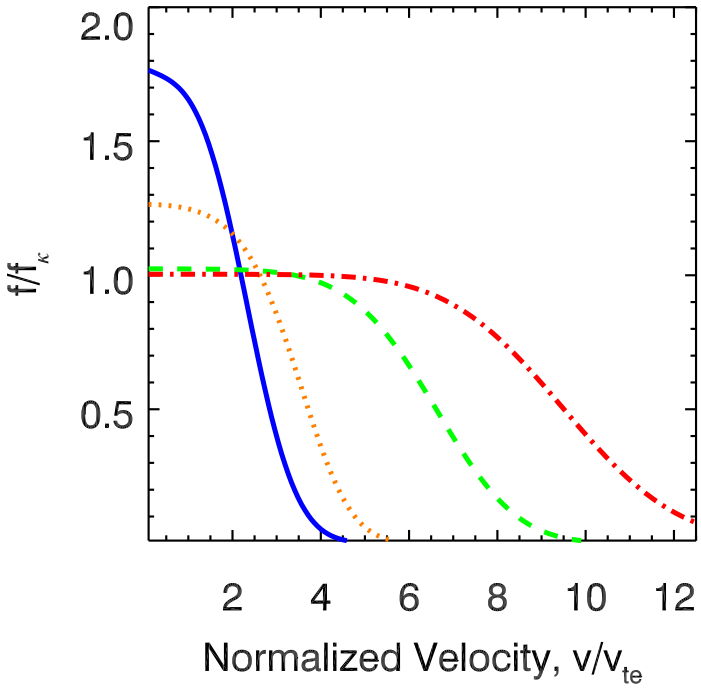

Figure 3.3: Evolution of the normalized distribution, f/f_κ, with time for $\kappa\,(\equiv \Gamma/2D_0) = 5$ as before. The solid blue line shows the injected Maxwellian divided by the final steady state f_κ and then, from left to right: $f(v,t)/f_\kappa$ at $t/\tau_c^{\rm th} = 10$ (orange dotted line), $t/\tau_c^{\rm th} = 100$ (green dashed line), and $t/\tau_c^{\rm th} = 300$ (red dot-dashed line).

loss is not included within the model (equation 3.1) it is imperative that particles were not lost from the numerical system and so particle number was checked at each data output, staying constant for the duration of the simulations and; second, the solution to the steady state equation (see Section 3.3) is known and so the final steady state of the numerical simulations was compared to the kappa stationary solution, f_κ, agreeing well within numerical errors. The distribution is decided to be steady state when it is no longer changing between timesteps. This is tested by subtracting the distribution at the previous timestep from the distribution at the present time. When this is zero for all velocities, the evolution is assumed to have ceased, i.e. a steady state has been reached.

Figure 3.2 shows the evolution of an originally thermal population of electrons towards a final steady state which agrees well with the shape of a kappa distribution (see

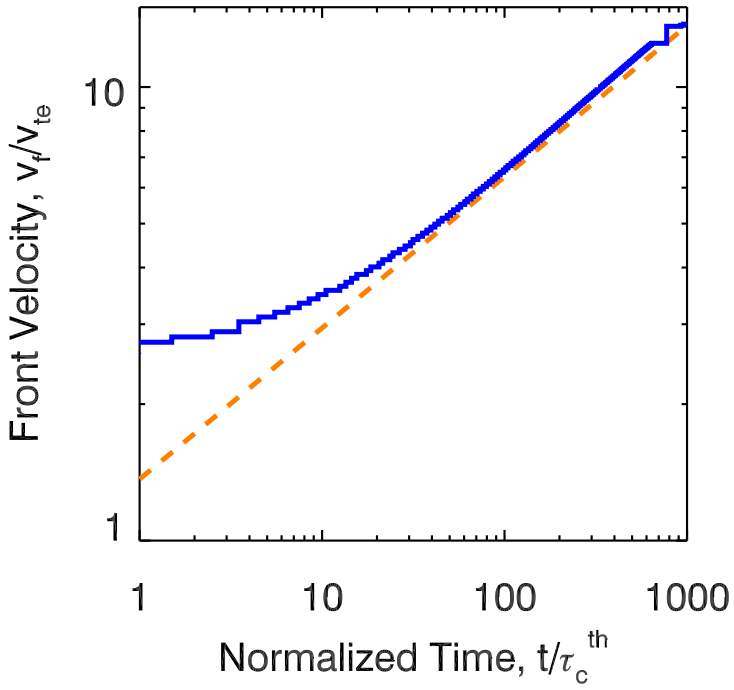

Figure 3.4: Location, v_f, of the front in velocity space (in units of the thermal speed $v_{\rm te}$) versus time (in units of the thermal collisional time $\tau_{\rm c}^{\rm th}$). The analytic approximation for front speed, $v_{\rm f}(t)$ (equation 3.46), is shown by the orange dashed line. The blue line shows the location of the numerical velocity front where $f/f_\kappa = 0.7$.

Figure 3.1). Note that at $t = 100\tau_{\rm c}^{\rm th}$ (the red dot-dash lines) the figure shows that the distribution is close to the final kappa distribution up to around $5v_{\rm te}$, which corresponds to 4 orders of magnitude of the distribution, $f(v,t)$. Therefore for a significant number of particles this distribution is close to a kappa distribution.

The evolution of the normalized distribution, f/f_κ, is shown in Figure 3.3. It is clear there is a 'wavefront' moving towards higher velocity with time, as expected from the advection-diffusion nature of equation (3.41). The normalised distribution is not shown after it has reached a steady-state (at around $t/\tau_{\rm c}^{\rm th} \sim 1000$), as it is constant across the domain. This figure confirms that the distribution is indeed close to the final kappa distribution up to $\simeq 5v_{\rm te}$ for $t = 100\tau_{\rm c}^{\rm th}$. Furthermore, it shows that at $t = 300\tau_{\rm c}^{\rm th}$ the distribution is indistinguishable from a kappa distribution up to $\simeq 7v_{\rm te}$.

Equation (3.46) showed that the location of the velocity front in space should approx-

imately be $v_{\rm f}(t) \sim t^{1/3}$. To assess the validity of this result a value of $u(v,t) = 0.7$ is chosen to approximate the position of the simulation front seen in Figure 3.3. The plot of simulated $v_{\rm f}$ versus t is shown in Figure 3.4 where the analytic solution is also shown. There is little agreement before $t \sim 10\tau_{\rm c}^{\rm th}$, due to the fact that this is a long time approximation, $t \gg \tau_{\rm c}^{\rm th}$, only holding when a significant portion of particles have been accelerated to non-thermal energies. There is also disagreement at $t \gtrsim 700\tau_{\rm c}^{\rm th}$ due to the simulations reaching the upper velocity limit in the numerical box. There is, however, excellent agreement in between these two limits, clearly both numerical and analytical solutions have the same time dependence, that is the power law slope $d\ln v_{\rm f}/d\ln t = 1/3$. Of course, the analytic model implies that the front position would continue moving toward greater and greater velocity. In reality, because this is a relatively slow process, there will be a limit on how long the particles can be confined in the acceleration region and as such there will be a maximum energy (front position) at which the acceleration stops and particles begin to escape (see next section). Note that in Bian et al. (2014) the value of $u(v,t)$ was chosen to be 0.5 as it seemed the most natural choice. There was an offset between the two solutions that was unimportant, merely coming from the subjective nature of choosing $u(v,t) = 0.5$ as an approximation to the position of the front in the simulations. Equally, here it is shown that choosing the value to be 0.7 creates a better overlap, but again the choice is subjective, and purely illustrates that instead of a sharp edge to the front as predicted by the analytic approximation there is, in reality, a smoother drop off to the front, caused by the re-introduction of the diffusive term in the numerics (Chavanis & Lemou, 2005).
In summation, the numerical results show that the velocity space front scenario described in Section 3.4 provides a generally good description of the way particles are accelerated from an originally thermal population of electrons to the kappa distribution.

3.6 Spatial Transport and Escape

The acceleration model considered in this chapter assumes that the electron distribution is close to isotropic in pitch-angle, as it requires efficient pitch-angle scattering within

the acceleration region. In the limit of strong pitch-angle scattering the transport of particles can be thought of as the spatial diffusion parallel to the magnetic field (see e.g. Kontar et al., 2014) over length scales much greater than the electron's mean free path due to turbulence $\lambda(v)$ (equation 1.25).

If the spatial extent of the acceleration region is σ (see e.g. Xu et al., 2008) then the escape of particles can be modelled via a 'leaky-box' model in which case equation (3.1) becomes,

$$\frac{\partial f}{\partial t} = \frac{1}{v^2}\frac{\partial}{\partial v}\left\{v^2\left[\left(\frac{\Gamma v_{\rm te}^2}{2v^3} + D_{\rm turb}(v)\right)\frac{\partial f}{\partial v} + \frac{\Gamma}{v^2}\,f\right]\right\} - \frac{f}{\tau_{\rm esc}}, \tag{3.56}$$

where the escape timescale has been defined,

$$\tau_{\rm esc} = \frac{3\sigma^2}{\lambda(v)v} = \left(\frac{3\sigma}{\lambda(v)}\right)\left(\frac{\sigma}{v}\right), \tag{3.57}$$

taking account of the diffusive nature of the transport (see Chapter 1 Section 1.3.2). The escape term acts to deplete the number of particles within the acceleration region with a characteristic timescale, $\tau_{\rm esc}$. It is easily seen from equation (3.57) that the escape timescale becomes approximately the free-streaming escape time, σ/v (Chapter 1 Section 1.3.2), only when the mean free path due to turbulence, $\lambda \sim \sigma$. Unless some extra source term is introduced to replenish the acceleration region (such as the final term in equation (13) of Petrosian (2012)) the number of particles within it will continuously decrease through time. This would, of course, result in fluctuations in plasma temperature but this is offset by the heat bath assumption mentioned earlier.

Equation (3.56) now has four terms describing: acceleration, collisional deceleration, collisional diffusion and escape, each with their respective timescales (equations 3.3-3.5 and 3.57). Figure 3.5 shows these timescales plotted against velocity. Ignoring, for now, the red dash-dot lines showing escape timescales parameterized by λ/σ, the balance of timescales resulting in the kappa distribution becomes clear. At low velocities $\tau_{\rm diff} \sim v^5$ is the shortest timescale in the system meaning it is dominant over the acceleration timescale, $\tau_{\rm acc}$. This results in the collisionally dominated thermal core seen for $v < \kappa v_{\rm te}$ in Figure 3.1. At higher velocities, $v > \kappa v_{\rm te}$, the collisional diffusion timescale, $\tau_{\rm diff}$, becomes longer than both $\tau_{\rm acc}$, the acceleration timescale, and the collisional

deceleration timescale, τ_c. The shape of distribution at these energies is thus controlled by the balance of τ_{acc} and τ_c but since both scale as v^3 this means there is no dominant process here, resulting in a high energy power-law tail with spectral index $\kappa = \tau_{acc}/2\tau_c$. The turbulent mean free path, $\lambda(v)$, of a particle in the flaring, dense solar corona would be expected to be either constant or increasing with energy. This would mean that the escape timescale, τ_{esc}, would be a decreasing function of energy, easily seen in equation (3.57). Therefore, at high enough velocities τ_{esc} will become the dominant timescale in the system (as the other three are increasing functions of v). An escape timescale, v_{esc}, can be defined as the point, in velocity space, where the 'front' from Section 3.4 reaches a velocity $v_f = v_{esc}$, i.e. from equation (3.54) and (3.55) at a time,

$$t = \frac{v_{te}^3}{3\Gamma}\left(\frac{v_{esc}}{v_{te}}\right)^3 = \frac{v_{esc}^3}{3\Gamma}. \tag{3.58}$$

Equating this to the escape timescale (equation 3.57) gives the expression,

$$\frac{v_{esc}^3}{3\Gamma} = \frac{3\sigma^2}{\lambda(v_{esc})\, v_{esc}}. \tag{3.59}$$

For a general turbulent mean free path, $\lambda = \lambda_0(v/v_0)^\alpha$, the explicit solution for the escape velocity becomes,

$$v_{esc} = \left(\frac{9\Gamma\sigma^2 v_0^\alpha}{\lambda_0}\right)^{1/(4+\alpha)}. \tag{3.60}$$

In Figure 3.5 τ_{esc} is shown for different values of the dimensionless ratio λ/σ (setting the turbulent mean free path, λ, to be constant), a parameter that quantifies the 'strength' of the scattering within the acceleration region. It is obvious that for an acceleration region of the same length a decrease in λ results in a longer escape timescale, resulting in an intersection with τ_{acc} at a higher energy. As an example, consider the case for $\lambda/\sigma = 0.2$, the escape timescale intersects τ_{acc} at a velocity where it is yet to intersect, and is comparable to, the collisional diffusion timescale, τ_{diff}. As such, particle escape would mean the power-law tail would not form and an asymptotic kappa distribution would not result in this case. Alternatively, in the case of $\lambda/\sigma = 0.0001$, the escape timescale intercepts at a much higher velocity. In this case a distribution approaching the asymptotic kappa would form for $v \ll v_{esc}$ with a significant divergence only at high energies, $v \gtrsim v_{esc}$.

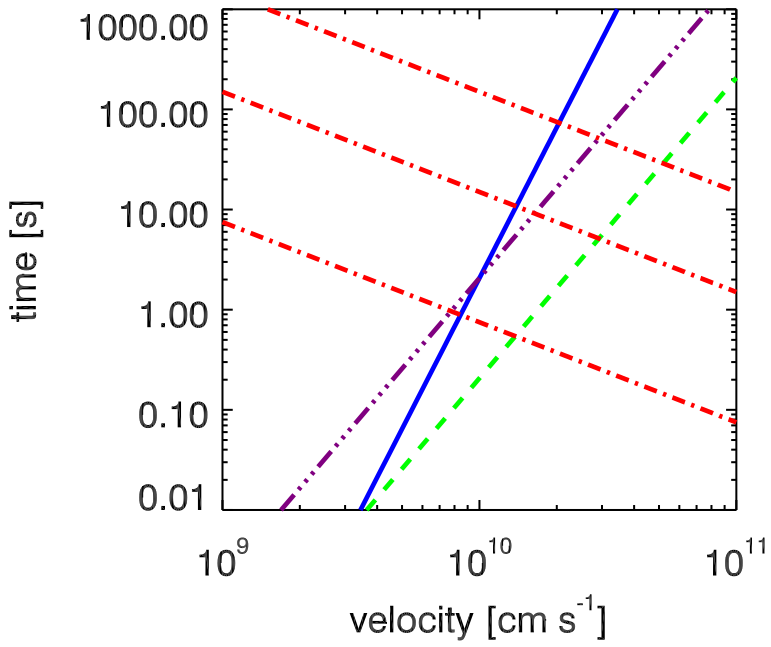

Figure 3.5: Characteristic timescales of the system. The solid blue line represents the collisional diffusion timescale, $\tau_{\rm diff} \propto v^5$ (equation 3.5), the purple triple-dot-dash line the acceleration timescale, $\tau_{\rm acc} \propto v^3$ (equations 3.3 and 3.10), the green dashed line the collisional deceleration timescale, $\tau_{\rm c} \propto v^3$ (equation 3.4), and the red dot-dashed lines the escape time, $\tau_{\rm esc} \propto v^{-1}$ (equation 3.57), for, from bottom to top, $\lambda/\sigma = 0.2$, 0.01 and 0.001.

The 'leaky-box' formulation (equation 3.56) can be solved by considering the situation to be analogous to the pitch-angle loss cone in a magnetic trap. In this case there is a critical pitch-angle below which electrons escape and above which they remain fully trapped. By analogy, electrons that are at velocities less than $v_{\rm esc}$ can be considered trapped and those at energies above the escape velocity can escape. The Fokker-Planck can then be written without the explicit escape term,

$$\frac{\partial f}{\partial t} = \frac{1}{v^2}\frac{\partial}{\partial v}\left\{v^2\left[\left(\frac{\Gamma v_{\rm te}^2}{2v^3} + D_{\rm turb}(v)\right)\frac{\partial f}{\partial v} + \frac{\Gamma}{v^2}\,f\right]\right\}, \tag{3.61}$$

together with a boundary condition that assumes all particles above the escape velocity leave the acceleration region,

$$f(v_{\rm esc}, t) = 0. \tag{3.62}$$

This approximation is valid in the case where the electron escape rate is small and

the acceleration region can be considered to be essentially thick-target. The time-dependent solution can be found by perturbation analysis. A solution of the form,

$$f(v,t) = A\,\mathrm{e}^{\nu t}\,g(v), \tag{3.63}$$

(where $\nu < 0$ is the decay rate) to the Fokker-Planck (equation 3.6) is sought (subject to the boundary condition above). So,

$$A\,\mathrm{e}^{\nu t}\,\nu g(v) = \frac{1}{v^2}\frac{\partial}{\partial v}\left[v^2 D(v)\left(A\,\mathrm{e}^{\nu t}\,\frac{dg(v)}{dv} + A\,\mathrm{e}^{\nu t}\,g(v)U'(v)\right)\right], \tag{3.64}$$

which becomes, after cancelling like terms,

$$\nu g(v) = \frac{1}{v^2}\frac{\partial}{\partial v}\left[v^2 D(v)\left(\frac{dg(v)}{dv} + g(v)\frac{dU(v)}{dv}\right)\right]. \tag{3.65}$$

By moving the v^2 term to the left hand side the first integral of this expression (with respect to v) can be found,

$$\nu\int_0^v w^2 g(w)\;dw = v^2 D(v)\left(\frac{dg(v)}{dv} + g(v)\frac{dU(v)}{dv}\right), \tag{3.66}$$

where w is just a dummy velocity variable introduced for clarity. This can be rearranged as,

$$\frac{dg(v)}{dv} + g(v)\frac{dU(v)}{dv} = \frac{\nu}{v^2 D(v)}\int_0^v w^2 g(w)\;dw. \tag{3.67}$$

The solution to this equation can be written as an expansion of the decay rate ν (King, 1965; Lemou & Chavanis, 2010),

$$g(v) = g_0(v) + \nu g_1(v) + \ldots. \tag{3.68}$$

It is okay to consider only the zeroth and first order terms here as the escape rate is for the limit of small escape. It is again noted that the particles escape above some critical velocity, v_{esc}, and under this they stay trapped. If the kappa distribution (or equivalently the HXR producing electron spectrum) itself is considered it is easy to see that with the small number of particles at higher energies for a typical value of $\kappa = 5$ (Figure 3.1) that the distribution is dominated by lower energies. Consider setting the escape speed at $v_{\mathrm{esc}} = 5v_{\mathrm{te}}$, the number of particles here is ~ 5 orders of magnitude less

than at the low energy core. Thus the number of particles escaping is low compared to the distribution as a whole, so the decay rate $|\nu| \ll 1$ and the assumption above holds. The zero order equation is,

$$\frac{dg_0(v)}{dv} + g_0(v)\frac{dU(v)}{dv} = 0. \tag{3.69}$$

This has the same general solution as equation (3.9) repeated here,

$$g_0(v) = A\,\mathrm{e}^{-U(v)}, \tag{3.70}$$

where A is a normalization factor. The first order equation is,

$$\frac{dg_1(v)}{dv} + g_1(v)\frac{dU(v)}{dv} = \frac{A}{v^2 D(v)}\int_0^v w^2\,\mathrm{e}^{-U(w)}\;dw. \tag{3.71}$$

Multiplying through by integrating factor $\mathrm{e}^{U(v)}$ this gives,

$$\mathrm{e}^{U(v)}\frac{dg_1(v)}{dv} + \mathrm{e}^{U(v)}\,g_1(v)\frac{dU(v)}{dv} = \frac{A\,\mathrm{e}^{U(v)}}{v^2 D(v)}\int_0^v w^2\,\mathrm{e}^{-U(w)}\;dw. \tag{3.72}$$

Now defining,

$$\chi'(v) = \frac{\mathrm{e}^{U(v)}}{v^2 D(v)}\int_0^v w^2\,\mathrm{e}^{-U(w)}\;dw, \tag{3.73}$$

equation (3.72) becomes,

$$\frac{d}{dv}\left[\mathrm{e}^{U(v)}\,g_1(v)\right] = A\chi'(v), \tag{3.74}$$

which integrated gives the final expression for $g_1(v)$,

$$g_1(v) = A\,\mathrm{e}^{-U(v)}\,\chi(v). \tag{3.75}$$

Substituting equations (3.70) and (3.75) into equation (3.68) gives the distribution to the first order in ν,

$$f(v,t) = A\,\mathrm{e}^{-U(v)}\,\mathrm{e}^{\nu t}\left[1 + \nu\chi(v)\right]. \tag{3.76}$$

Subbing in the boundary condition (3.62) then,

$$f(v_{\mathrm{esc}},t) = 0 = A\,\mathrm{e}^{-U(v_{\mathrm{esc}})}\,\mathrm{e}^{\nu t}\left[1 + \nu\chi(v_{\mathrm{esc}})\right], \tag{3.77}$$

which in turn gives the decay rate,

$$\nu = -\frac{1}{\chi(v_{\mathrm{esc}})}. \tag{3.78}$$

This is the escape rate in the limit of high escape velocity. Setting $D_{\rm turb} = D_0/v$ again (equation 3.10),

$$D(v) = \frac{\Gamma v_{\rm te}^2}{v^3} + \frac{D_0}{v}, \tag{3.79}$$

means that (equation 3.17),

$$U(v) = \kappa \ln\left(1 + \frac{v^2}{\kappa v_{\rm te}^2}\right). \tag{3.80}$$

So, substituting equations (3.78) and (3.80) into (3.76) gives the solution in the limit of high escape velocity,

$$f(v,t) = \frac{n\,\mathrm{e}^{-t/\chi(v_{\rm esc})}}{\pi^{3/2} v_{\rm te}^3 \kappa^{3/2}} \frac{\Gamma(\kappa)}{\Gamma(\kappa - 3/2)} \left(1 + \frac{v^2}{\kappa v_{\rm te}^2}\right)^{-\kappa} \left[1 - \frac{\chi(v)}{\chi(v_{\rm esc})}\right], \tag{3.81}$$

where the final term here describes the deviation of this distribution from the kappa distribution (equation 3.18). The loss of particles from the system is accounted for by the term,

$$n(t) = n\,\mathrm{e}^{-t/\chi(v_{\rm esc})}, \tag{3.82}$$

which can be thought of as the number of particles in the system at a time, t. These terms arise from allowing escape in the system. Both equation (3.82) and the final term in the brackets of equation (3.81) depend on the function $\chi(v)$ which is determined from equations (3.10), (3.17) and (3.73),

$$\chi'(v) = \frac{\exp\left\{\kappa \ln\left(1 + \frac{v^2}{\kappa v_{\rm te}^2}\right)\right\}}{v^2\left(\frac{\Gamma v_{\rm te}^2}{v^3} + \frac{D_0}{v}\right)} \int_0^v w^2 \exp\left\{-\kappa \ln\left(1 + \frac{w^2}{\kappa v_{\rm te}^2}\right)\right\} dw, \tag{3.83}$$

which becomes,

$$\chi'(v) = \frac{\left(1 + \frac{v^2}{\kappa v_{\rm te}^2}\right)^{\kappa}}{v^2 \frac{v_{\rm te}^2 D_0}{v^3}\left(\frac{\Gamma}{2D_0} + \frac{v^2}{v_{\rm te}^2}\right)} \int_0^v w^2 \left(1 + \frac{w^2}{\kappa v_{\rm te}^2}\right)^{-\kappa} dw. \tag{3.84}$$

Now, remembering the definition of the dimensionless parameter κ (equation 3.12) and with some more algebraic manipulation this becomes,

$$\chi'(v) = \frac{v}{\kappa v_{\rm te}^2 D_0} \times \frac{\left(1 + \frac{v^2}{\kappa v_{\rm te}^2}\right)^{\kappa}}{\left(1 + \frac{v^2}{\kappa v_{\rm te}^2}\right)} \int_0^v w^2 \left(1 + \frac{w^2}{\kappa v_{\rm te}^2}\right)^{-\kappa} dw, \tag{3.85}$$

which is of course,

$$\chi'(v) = \frac{v}{\kappa v_{\rm te}^2 D_0}\left(1+\frac{v^2}{\kappa v_{\rm te}^2}\right)^{\kappa-1}\int_0^v w^2\left(1+\frac{w^2}{\kappa v_{\rm te}^2}\right)^{-\kappa} dw. \tag{3.86}$$

It is pertinent here to remember that the solution (equation 3.81) is only valid in the case where escape velocity is sufficiently high and the decay rate $|\nu| \ll 1$, i.e. where the acceleration region is essentially thick target. Benz (1977) found the stationary solution of a similar leaky-box equation where they had no collisional diffusion but did have a source term of particles.

3.7 Stochastic Acceleration by a Large-scale Electric Field with Strong Pitch-angle Scattering

As mentioned before, the main energy release mechanism in solar flares involves the reconnection of magnetic fields resulting in the formation of electric fields. Various authors have tackled this problem, either with large scale sub-Dreicer (Benka & Holman, 1994) or super-Dreicer (Litvinenko, 1996) electric fields. How does the role of pitch-angle scattering affect the analysis of large scale coherent electric fields? A main objective of the work in the final section of Bian et al. (2014) was to highlight that efficient pitch-angle scattering of particles in a region of constant electric field could result in an effect resembling stochastic acceleration. The interest of this chapter is the formation of kappa distributions, so the requirements for the diffusion coefficient $D_{\rm turb} \sim 1/v$ are discussed.

In the presence of an acceleration region with an electric field of constant magnitude, $E_{||}$ [statvolt cm^{-1}], parallel to the ambient magnetic field, $\mathbf{B}$ (aligned along x), in a regime with efficient pitch angle scattering operating on a turbulent mean free path, $\lambda(v)$, the evolution of the electron distribution, $f(x,\mu,v,t)$, can be described by the one-dimensional form of the Fokker-Planck equation,

$$\frac{\partial f}{\partial t} + v\mu\,\frac{\partial f}{\partial x} + \frac{eE_{||}}{m_e}\mu\,\frac{\partial f}{\partial v} + \frac{eE_{||}}{m_e}\frac{(1-\mu^2)}{v}\,\frac{\partial f}{\partial \mu} = \frac{v}{\lambda(v)}\,\frac{\partial}{\partial \mu}\left[(1-\mu^2)\,\frac{\partial f}{\partial \mu}\right], \tag{3.87}$$

where all other parameters are listed in the Table of Symbols. This is the same form as the model studied in Kruskal & Bernstein (1964) but in their case $\lambda \sim v^4$. The final term on the right hand side describes the pitch-angle diffusion within the system. In general, this acts to isotropize the distribution on a pitch-angle diffusion timescale given by,

$$\tau_{\rm pa} = \frac{\lambda(v)}{v}, \tag{3.88}$$

where in most cases the turbulent mean free path could be expected to be a function of v (See Kontar et al., 2014, Appendix).

The acceleration within the system is controlled by the coefficient in front of the $\partial f/\partial v$ term, i.e.

$$\frac{\partial v}{\partial t} = \frac{eE_{||}}{m_e}\mu, \tag{3.89}$$

which shows that v and μ are interlinked in this formalism. The isotropizing effect of the pitch-angle scattering comes into effect whenever $\tau_{\rm pa}$ is a decreasing function of v. In fact, if $\lambda \sim v^\alpha$ then $\tau_{\rm pa} \sim v^{\alpha-1}$ and it can be shown that for $\alpha < 1$ the particle distribution is close to isotropic even in the presence of a constant electric force (Piasecki, 1981; Chernov & Dolgopyat, 2007). In these cases there is no runaway acceleration of particles, the runaway phenomenon being the uninhibited growth in particle velocities as $t \to \infty$ (Benka & Holman, 1994). The combined effects of efficient pitch-angle diffusion and a constant electric field produces an isotropic diffusive acceleration and an unlimited growth in their kinetic energy in the absence of collisional energy losses. The turbulent diffusion coefficient can be calculated from the Taylor (1922) formula,

$$D_{\rm turb}(v) = \frac{e^2E_{||}^2}{m_e^2}\int_0^\infty \langle\mu(0)\mu(t)\rangle dt = \frac{e^2E_{||}^2}{m_e^2}\frac{\lambda(v)}{v}. \tag{3.90}$$

For the case where there is a constant turbulent mean free path then,

$$D_{\rm turb}(v) = \frac{D_0}{v}, \tag{3.91}$$

with,

$$D_0 = \frac{e^2E_{||}^2\lambda}{m_e^2}. \tag{3.92}$$

In Section 3.4 it was shown that in the case where the turbulent diffusion coefficient $\propto 1/v$, as above in equation (3.91), results in an acceleration timescale, $\tau_{\rm acc} \sim v^3/D_0$ (equation 3.3), meaning that it has the same velocity dependence as the collisional deceleration/friction time, $\tau_{\rm c}$ (equation 3.4). Now, since $D_{\rm turb} \propto \lambda/v \sim 1/v$ and (from equation 3.3),

$$\tau_{\rm acc} = \frac{v^2}{D_{\rm turb}(v)}, \tag{3.93}$$

the acceleration of a particle at speed v can be expressed,

$$\frac{dv}{dt} \sim \frac{v}{\tau_{\rm acc}} \sim \frac{1}{v^2}, \tag{3.94}$$

which means that,

$$\frac{dE}{dt} \equiv m_e v \frac{dv}{dt} \sim \frac{1}{v} \sim E^{-1/2}. \tag{3.95}$$

This expression can be integrated leading to $E^{3/2} \sim t$, and thus,

$$E \propto t^{2/3}, \tag{3.96}$$

(see also equation 3.52). The role of collisions is to allow the slow convergence to the final steady state kappa distribution given in equation (3.18) due to the balance between turbulent acceleration and collisional friction.

There are a few drawbacks to the above model. In reality there is a maximum energy gain available, bounded by the finite electric potential drop due to the finite size of the acceleration region, which is ignored here. Furthermore, the approximation of escape in Section 3.6 is not valid for the case of a stationary electric field. The maximum energy gained from a temporally varying electric field in a finite acceleration region depends on the escape timescale, whereas the maximum energy gained when in the presence of a constant electric field is independent of the confinement time. Moreover, only particles travelling parallel to the applied electromotive force, $eE_{||}$, gain energy here. Particles moving in the opposite direction will in fact lose energy. This means that there is a spatial asymmetry in the model, even with the strong isotropization of the particle distribution. This is undesirable in a solar flare context due to, for example, the presence of at least two HXR footpoints in almost all flares. Therefore, this model

requires fragmentation of the electric field, such as opposite electric fields on different magnetic field lines (Holman, 1985; Emslie & Henoux, 1995; Bian & Browning, 2008; Cargill et al., 2012; Gordovskyy et al., 2013) to be invoked.

The parameter κ, given by equation (3.12), is the ratio between Γ and D_0. Therefore in a model in which the acceleration results from a direct electric field studied here, it relates the ambient density, n_e, to the square of the accelerating electric field, $E_{||}$. The shape of any resulting distribution will thus constrain either one, or both, of n_e and $E_{||}$.

Using equations (3.12) and (3.92) means κ can be expressed as,

$$\kappa = \frac{3}{2}\frac{m_e^2}{e^2 E_{||}^2 \lambda}\Gamma. \tag{3.97}$$

Now, defining the collisional mean free path,

$$\lambda_{\rm c} = \frac{(k_{\rm B}T)^2}{4\pi n_e e^4 \ln\Lambda}, \tag{3.98}$$

and the Dreicer-field (the field strength required to accelerate an electron to the thermal energy over a distance equal to its collisional mean free path),

$$E_{\rm D} = \frac{k_{\rm B}T}{e\lambda_{\rm c}}, \tag{3.99}$$

means that κ becomes,

$$\kappa = \frac{3}{2}\left(\frac{\lambda_{\rm c}}{\lambda}\right)\left(\frac{E_{\rm D}}{E_{||}}\right)^2. \tag{3.100}$$

As discussed previously in this chapter, the typical value for κ in a solar flare context is ~ 5 and so,

$$E_{||} = \left(\frac{3}{10}\frac{\lambda_{\rm c}}{\lambda}\right)^{1/2} E_{\rm D}. \tag{3.101}$$

Furthermore, due to the normalization factor in equation (3.18) there is the additional constraint that $\kappa > 3/2$ and therefore,

$$E_{||} < \left(\frac{\lambda_{\rm c}}{\lambda}\right)^{1/2} E_{\rm D}. \tag{3.102}$$

For a typical dense hard X-ray coronal source, a density, $n_e \sim 10^{11}$ cm^{-3}, and temperature, $T \sim 2\times10^7$ K, may be expected. This would produce a collisional mean

free path, $\lambda_c = 5 \times 10^6$ cm, and a dreicer field, $E_D = 3 \times 10^{-4}$ V cm^{-1}. Furthermore, Kontar et al. (2014) show that in order to be consistent with the observed variation in source size with energy, the turbulent mean free path must be in the range $10^8 - 10^9$ cm. The above analysis shows that even the simple model outlined above could provide constraints on the accelerating electric field strength, $E_{||}$, depending on the spectral index, κ, obtained.

3.8 Conclusions to the Chapter

Driven by RHESSI observations of coronal hard X-ray sources where there is little or no footpoint emission, a model in which there is cospatial acceleration, collisional deceleration, thermalization and HXR bremsstrahlung emission was considered. Choosing the diffusion coefficient to be inversely proportional to velocity and with no particle escape, the electron distribution was shown to approach an asymptotic kappa form. The reason for this particular choice of diffusive coefficient is clear when considering the standard fitting method for RHESSI observations, the kappa distribution giving a smooth transition between a thermal like core and a power-law tail with no need for a (possibly artificial) low energy cutoff. Here the main results from the chapter are summarized:

- Unlike previous studies of kappa distributions in solar flares (Kašparová & Karlický, 2009; Oka et al., 2013) the parameter κ obtained in this chapter has an immediate physical significance. It is the dimensionless ratio between the acceleration timescale, τ_{acc}, and the collisional deceleration/friction time, τ_c, or, equivalently, the collisional parameter, Γ, to the turbulent diffusion coefficient parameter, D_0. This means that the index of the kappa distribution obtained from this model provides information on the relative strength of these two effects within the system.

- The approach toward the final steady state kappa distribution (from an originally thermal, Maxwellian distribution) has been shown to proceed as a 'wavefront' in

velocity space with position given by $v_f(t) \sim t^{1/3}$. This can be thought of as the distribution relaxing to the final steady state kappa distribution at low velocities first followed by higher velocities later. This is corroborated by the numerical results of Section 3.5.

- At high velocities, the time taken to approach the final stationary state kappa is long enough that escape will have an effect. The solution in the limit of small escape where the acceleration region is essentially thick-target is shown in Section 3.6 where the shape of the distribution with respect to the timescales involved is discussed.

The quality of the HXR observations from RHESSI enables the determination of the X-ray emitting electron spectrum to a high accuracy. With analysis of coronal HXR sources the model could be tested; quantitative analysis of where the observed spectrum agrees/disagrees with the asymptotic, escape free, kappa distribution could provide information on physical parameters, such as the acceleration region length, σ, and the diffusion coefficient parameter, D_0. If the acceleration is by a direct electric field this further reveals something about the accelerating electric field, $E_{||}$, as $D_0 \propto E_{||}^2$.
In this chapter, spatially independent acceleration and transport has been examined due to the cospatial nature of the acceleration and energy loss in the regime considered. As well as being the driving force of the work here, coronal HXR sources such as the 2005 August 23 flare (Chapter 2 Section 2.4.1) have also revealed that the acceleration of particles in solar flares is consistent with an extended acceleration region within the loop which is spatially inhomogeneous (e.g. Xu et al., 2008). The effects of this on the acceleration and transport of electrons in solar flares is discussed in the next chapter.

Chapter 4

Spatially Inhomogeneous Acceleration of Electrons in Solar Flares

The work in this Chapter can be found in Stackhouse & Kontar (2017)

4.1 Introduction to the Chapter

In the previous chapter a model in which spatial dependence is neglected was studied. In this chapter the effects of the intrinsic spatial variation within solar flares is fully taken into account. This work was driven by the observations of Xu et al. (2008), Kontar et al. (2011a) and Guo et al. (2012) showing that the acceleration region must be extended and within the looptop region to be consistent with observations.

As discussed in Chapter 1 Section 1.2, acceleration in the coronal plasma can be split into two broad regimes; whether the process behind it is systematic or stochastic in nature. Observational evidence (Kontar & Brown, 2006) points toward an accelerated electron population that is isotropic, favouring a stochastic acceleration mechanism. Furthermore, systematic acceleration regimes often have large scale electrodynamic issues intrinsic within them (Emslie & Henoux, 1995). Stochastic acceleration has

also been shown to produce acceleration efficiencies consistent with HXR observations (Emslie et al., 2008). The actual process of stochastically accelerating electrons can happen in a variety of ways (Bian et al., 2012) but the acceleration itself is most often well described by a turbulent velocity diffusion coefficient, D_{vv} (see discussion in Chapter 1 Section 1.2.3).

Transporting electrons of tens of keV in solar flares could be expected to fall into one of two categories, scatter-free (no pitch-angle scattering) or diffusive (efficient pitch-angle scattering). If the transport is scatter-free in nature the accelerated electrons experience negligible pitch-angle scattering and hence for sufficiently high velocities deposit most of their energy in the dense chromospheric footpoints. As discussed in Chapter 1 Section 1.3.2, there is mounting evidence that the transport of electrons should involve scattering: firstly, there is a lack of anisotropy evident from hard X-ray observations (Kontar et al., 2011b, as a review); secondly, albedo diagnostics (Kontar & Brown, 2006; Dickson & Kontar, 2013), as well as stereoscopic measurements (Kane et al., 1998), are inconsistent with strong downward beaming below $\sim$ 100 keV; thirdly, the majority of stochastic acceleration models developed for solar flares require strong pitch-angle scattering (Sturrock, 1966; Melrose, 1968; Benz & Smith, 1987; Petrosian & Donaghy, 1999); finally, the accelerated electrons will propagate in a turbulent or beam-generated turbulent media.

As already mentioned, RHESSI imaging spectroscopy has revealed that the acceleration region in the hard X-ray coronal sources occupy a noticeable fraction of the loop (Xu et al., 2008). So far however, the modelling and comparison with observations has been limited to spatially averaged or single-point acceleration/injection. Current modelling, for example the leaky-box approximation, accounts for transport implicitly by introducing an escape term (Chen & Petrosian, 2013). This allows the study of the acceleration term without complications arising from transport. While the energy distribution can be studied, the spatial distribution observed in flares cannot. An alternative simplifying approach is to inject an already accelerated power-law electron distribution and examine transport effects (Bai, 1982; Emslie, 1983; McTiernan & Petrosian, 1990; Ryan & Lee, 1991; Jeffrey et al., 2014), but this does not account for

the effects of acceleration on the transport process. Evidently, such a split between acceleration and transport is not justified and inadequate to model recent RHESSI observations.

In this chapter a model is presented that accounts simultaneously for transport and acceleration of electrons in an extended acceleration region of solar corona. The effects of a spatially varying, extended acceleration region are examined during the evolution of the electron spectrum from an initial Maxwellian distribution. The introduction of an extended, inhomogeneous, acceleration region results in a softer spectrum for both scatter-free and diffusive transport when comparing to the spectral index expected from the analytic leaky-box solution. The work shows spatial effects should be taken account of explicitly when modelling acceleration and transport in solar flares.

Section 4.2 introduces the model describing the acceleration and parallel transport in solar flares as well as showing the simplified analytic leaky-box model not dependent on space. Chapter 2 Section 2.4.2 discussed how to infer model parameters from the 2011 February 24 flare. These input parameters are used in the numerical solution of the model in Section 4.4. The results of the numerical simulations are compared to the leaky-box solution with the imaging spectroscopy results also shown for context. Section 4.5 discusses the implications of this work.

4.2 Acceleration and Transport of Energetic Electrons in Solar Flares

The evolution of the electron distribution, $f(v, x, t)$ (one-dimensional in velocity space) or $f(\mathbf{v}, x, t)$ (three-dimensional in velocity space), parallel to the magnetic field, $\mathbf{B}_0$ (aligned in the x-direction), can be described by the Fokker-Planck equation.

In the next two subsections the two transport regimes considered are outlined.

4.2.1 Scatter-free transport

If the electric field accelerating electrons is parallel to the background magnetic field, then the electron dynamics can be approximated as one-dimensional. In this case stochastic acceleration will only act to accelerate electrons parallel to the field and so the evolution of the electron distribution, $f(v,x,t)$, is described by the one-dimensional Fokker-Planck equation,

$$\frac{\partial f}{\partial t} + v\frac{\partial f}{\partial x} = \frac{\partial}{\partial v}\left[D(v,x) + \frac{\Gamma(x)v_{\rm te}^2}{v^3}\right]\frac{\partial f}{\partial v} + \Gamma(x)\frac{\partial}{\partial v}\left(\frac{f}{v^2}\right), \tag{4.1}$$

where the collisional parameter is $\Gamma = 4\pi e^4 \ln\Lambda n(x)/m_{\rm e}^2$ (equation 1.10 with $Z=1$), $n(x)$ [cm^{-3}] is the density and all other terms are listed in the Table of Symbols. The distribution is normalised so that $n_e = \int f dv$. The second term on the left hand side of equation (4.1) describes the scatter-free transport in the system, while the second term inside the brackets on the right is the diffusion due to collisions and the final term on the right hand side describes the energy loss due to Coulomb collisions. $D(v,x)$ [cm^2 s^{-3}] is the 1-dimensional turbulent diffusion coefficient discussed in Section 4.2.3.

4.2.2 Diffusive Transport

In the case of strong pitch-angle scattering, where the mean free path due to scattering is less than characteristic acceleration region length, the angle averaged three-dimensional (in velocity space) form of the Fokker-Planck equation, assuming an isotropic pitch-angle distribution, can be used. The evolution of the electron distribution, $f(\mathbf{v},x,t)$, is then,

$$\frac{\partial f}{\partial t} - D_{\rm xx}\frac{\partial^2 f}{\partial x^2} = \frac{1}{v^2}\frac{\partial}{\partial v}\left[v^2 D(v,x) + \frac{\Gamma(x)v_{\rm te}^2}{v}\right]\frac{\partial f}{\partial v} + \frac{\Gamma(x)}{v^2}\frac{\partial f}{\partial v}, \tag{4.2}$$

where terms are analogous to those in equation (4.1), but the distribution is now normalized as $n_e = \int f 4\pi v^2 dv$ (this is of course assuming the electrons are still 'tied' to the field, i.e. there is negligible cross field diffusion of particles). The spatial diffusion coefficient is as discussed in Chapter 1, and is given by equation (1.27), $D_{\rm xx} = \lambda(v)v/3$. Note that as $D_{\rm xx}$ is independent of x it can be taken outside the partial derivative here.

In Chapter 1 Section 1.3.2 diffusive transport was introduced. In this chapter one case is examined; λ constant for all velocities. For this case $\lambda = 5 \times 10^8$ cm was taken, as it is the midpoint in the limits found for 30 keV electrons in Kontar et al. (2014).

As an aside, the mean free path may be expected to be velocity dependent in reality. In this case $\lambda(v)$ can be obtained from integrating over μ in equation (1.25) to obtain (see Appendix in Kontar et al., 2014),

$$\lambda(v) = \frac{3v}{8}\left(\frac{2}{b}\left[1 - \frac{a^2}{b^2}\right]\ln\left[\frac{a+b}{b}\right] - \frac{b-2a}{b^2}\right). \tag{4.3}$$

The quantities a and b are defined as,

$$a = \frac{(1+\bar{Z}^2)Kn(x)}{m_e^2 v^3} \quad \text{and} \quad b = \frac{1}{2}\left(\frac{\delta B}{B_0}\right)^2 \frac{v}{\lambda_B}, \tag{4.4}$$

where $\bar{Z}^2$ is the mean square atomic number, $K = 2\pi e^4 \ln\Lambda$ is the collisional parameter, $\delta B/B_0$ is the strength of magnetic field fluctuations and λ_B [cm] is the parallel correlation length for magnetic field fluctuations. The quantities a and b parameterize the strength of the collisional and non-collisional scattering respectively. If both these effects operated on similar scales then $a \sim b$. The expression for strong non-collisional scattering ($b \gg a$) is found in Kontar et al. (2014, Appendix). Equation (4.3) can be re-written in terms of a scattering timescale, $\tau(v)$, so,

$$\lambda(v) = \frac{3v}{8}\tau(v). \tag{4.5}$$

To obtain an order of magnitude estimate for the scattering timescale, the limits obtained in Kontar et al. (2014) can be used. Setting $\lambda = 5 \times 10^8$ cm at 30 keV this gives a scattering timescale of $\tau \simeq 0.18$ s.

As velocity dependence of the mean free path might be expected in reality this will hopefully be examined in future. The numerical solutions to equations (4.1) and (4.2) are shown in Section 4.4.

4.2.3 Spatially Dependent Diffusion Coefficient

As already mentioned, imaging spectroscopy with RHESSI has revealed the extended nature of the acceleration region in the HXR looptop source (e.g. Xu et al., 2008;

Guo et al., 2012). In order to examine the effects of a spatially dependent, extended acceleration region in a regime with simultaneous transport a spatially non-uniform velocity diffusion coefficient is introduced,

$$D(v,x) = \frac{v_{\rm te}^2}{\tau_{\rm acc}} \left(\frac{v}{v_{\rm te}}\right)^{\alpha} {\rm e}^{-x^2/2\sigma^2}, \tag{4.6}$$

where $\tau_{\rm acc}$ [s] is the acceleration timescale (assumed to be constant in velocity in this study), σ [cm] is the spatial extent of the acceleration region and α is a constant that controls the strength of the velocity dependance. It is easy to see that with this choice, the acceleration is confined to a region in space, akin to an extended looptop acceleration region. It is assumed that the acceleration efficiency within this region is most effective at $x = 0$, the top of the loop, and that there is a drop off with distance that is gaussian in nature, the exponential term above. A gaussian distribution is chosen due to the structure noted in Xu et al. (2008) and Jeffrey & Kontar (2013) implying a more efficient acceleration mechanism in a core with a halo of escaping particles (as discussed in Chapter 2). The method to obtain the length of the acceleration region, the density and temperature from RHESSI imaging spectroscopy has been discussed in Chapter 2 Section 2.4.2. The diffusion coefficient is shown in Figure 4.1 for a specific choice of acceleration timescale, spatial extent, σ, and thermal velocity, $v_{\rm te}$, obtained from imaging spectroscopy. It is easy to see that there is a drop off in $D(v,x)$, and hence efficiency of acceleration, the further a particle is from the apex of the loop.

4.2.4 The Leaky-Box Fokker-Planck Approximation

At this point it is instructive to examine the leaky-box Fokker-Planck approximation (e.g. Chen & Petrosian, 2013). The equation for the spatially-averaged distribution function, $\langle f(v,t)\rangle$, is,

$$\frac{\partial\langle f\rangle}{\partial t} = \frac{\partial}{\partial v}\langle D(v)\rangle\frac{\partial\langle f\rangle}{\partial v} - \frac{\langle f\rangle}{\tau_{\rm esc}(v)}. \tag{4.7}$$

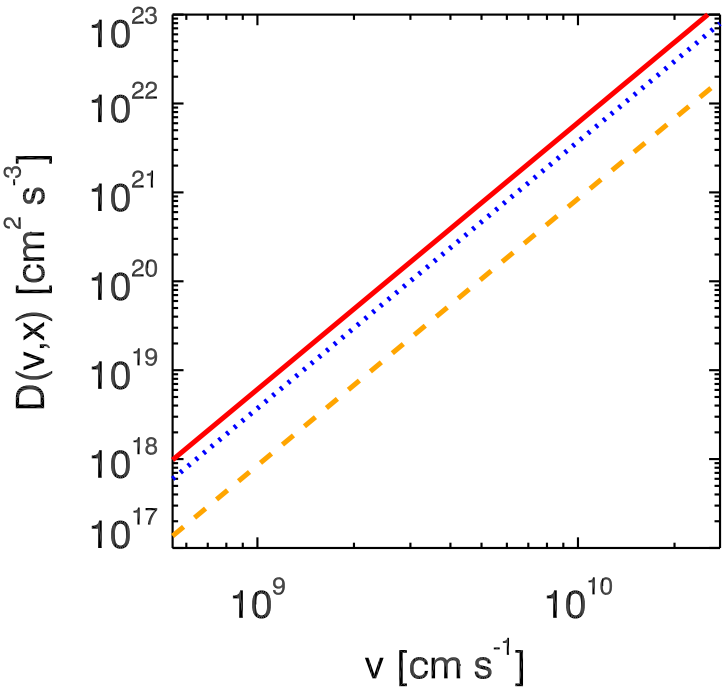

Figure 4.1: Diffusion coefficient versus velocity for $\tau_{\rm acc} = 10\tau_{\rm c}^{\rm th}$ for three different points in space: *Red, solid line*; $D(v, x = 0)$, *Blue, dot line*; $D(v, x = \sigma)$ and *Orange, dash line*; $D(v, x = 2\sigma)$.

Where $\langle \ldots \rangle$ denotes spatial averaging over the FWHM, $L = 2.35\sigma$. It should be noted here that while averaging it is assumed that,

$$\left\langle \frac{\partial}{\partial v} D(v) \frac{\partial f}{\partial v} \right\rangle \simeq \frac{\partial}{\partial v} \langle D(v) \rangle \frac{\partial \langle f \rangle}{\partial v}. \tag{4.8}$$

The spatially averaged diffusion coefficient is the average of equation (4.6), i.e.

$$\langle D(v) \rangle = \frac{1}{\sqrt{2\pi L^2}} \int_{-L}^{L} D(v, x) = \frac{1}{\sqrt{2\pi L^2}} \int_{-L}^{L} \frac{v_{\rm te}^2}{\tau_{\rm acc}} \left(\frac{v}{v_{\rm te}} \right)^{\alpha} {\rm e}^{-x^2/2\sigma^2}. \tag{4.9}$$

Now the expression $(1/\sqrt{2\pi L^2}) \int_{-L}^{L} {\rm e}^{-x^2/2\sigma^2} \simeq 1$ and so the spatially averaged diffusion coefficient is found to be,

$$\langle D(v) \rangle = \frac{v_{\rm te}^2}{\tau_{\rm acc}} \left(\frac{v}{v_{\rm te}} \right)^{\alpha}. \tag{4.10}$$

It is also important to note that, as with acceleration, the spatial dependence of transport in equation (4.1) is also neglected, i.e.

$$v \frac{\partial f}{\partial x} \rightarrow \frac{\langle f \rangle}{\tau_{\rm esc}}, \tag{4.11}$$

where the exact form of $\tau_{\rm esc}$ depends on the transport regime being studied.

Equation (4.7) is instructive and simple to use, but ignores the essential spatial dependencies in acceleration and transport. The stationary solution as $t \rightarrow \infty$ can be readily obtained from the following equation,

$$0 = \frac{\partial}{\partial v}\langle D(v)\rangle \frac{\partial \langle f\rangle}{\partial v} - \frac{\langle f\rangle}{\tau_{\rm esc}(v)}. \tag{4.12}$$

Since the X-ray producing electron spectrum is close to a power-law (Holman et al., 2003), a stationary solution of equation (4.12) in the form $\langle f\rangle \sim v^{-\delta_1}$ is assumed. Substituting the power-law solution of $\langle f\rangle$ gives,

$$\frac{\partial}{\partial v}\frac{v_{\rm te}^2}{\tau_{\rm acc}}\left(\frac{v}{v_{\rm te}}\right)^{\alpha}\frac{\partial v^{-\delta_1}}{\partial v} - \frac{v^{-\delta_1}}{\tau_{\rm esc}(v)} = 0. \tag{4.13}$$

Differentiating this expression and rearranging,

$$\delta_1^2 + (1-\alpha)\delta_1 - \frac{\tau_{\rm acc}}{\tau_{\rm esc}(v)}\left(\frac{v_{\rm te}}{v}\right)^{\alpha-2} = 0. \tag{4.14}$$

Using the quadratic formula and taking the root required to be consistent with $\delta > 0$ (the spectral index inferred for solar flares is positive) means,

$$\delta_1 = \frac{1}{2}\left[\alpha - 1 + \left((1-\alpha)^2 + 4\frac{\tau_{\rm acc}}{\tau_{\rm esc}(v)}\left(\frac{v_{\rm te}}{v}\right)^{\alpha-2}\right)^{1/2}\right], \tag{4.15}$$

obtaining a spectral index which is dependent upon $\tau_{\rm acc}$ and $\tau_{\rm esc}$.

For scatter-free transport the escape timescale is equal to the free streaming timescale, $\tau_{\rm esc} = \sigma/v$. Therefore, the spectral index is,

$$\delta_1 = \frac{1}{2}\left[\alpha - 1 + \left((1-\alpha)^2 + 4\frac{\tau_{\rm acc} v_{\rm te}^{\alpha-2}}{\sigma} v^{3-\alpha}\right)^{1/2}\right], \tag{4.16}$$

and it is easily seen that a spectral index independent of v can be obtained only for $\alpha = 3$, e.g.

$$\delta_1 = \frac{1}{2}\left[2 + \left(4 + 4\frac{v_{\rm te}}{\sigma}\tau_{\rm acc}\right)^{1/2}\right], \tag{4.17}$$

where δ_1 *must* be independent of v for the differentiation above between equations (4.13) and (4.14) to be valid. Of course, in order to put the results here, and those of the numerical simulations, in the context of the imaging spectroscopy results of the

2011 February 24 flare (Chapter 2) the index actually needed is that of the density weighted mean electron flux $\langle nVF(E)\rangle$ [electrons cm^{-2} s^{-1} keV^{-1}]. Using the fact that $\langle nVF(E)\rangle \sim \langle f\rangle/m_{\rm e}$ in one dimension this means that,

$$\langle nVF(E)\rangle^{\rm 1d}_{\rm LT} \sim v^{-\delta_1} \sim E^{-\delta_1/2}, \tag{4.18}$$

where the superscript makes clear this is the one-dimensional scatter-free expression and the subscript shows that this is the expected $\langle nVF(E)\rangle$ from the looptop.

Similarly, the three-dimensional Fokker-Planck (equation 4.2) gives the power law index,

$$\delta_2 = \frac{1}{2}\left[\alpha + 1 + \left((\alpha+1)^2 + 4\frac{\tau_{\rm acc}}{\tau_{\rm esc}}\left(\frac{v_{\rm te}}{v}\right)^{\alpha-2}\right)^{1/2}\right], \tag{4.19}$$

where $\tau_{\rm esc} = 3\sigma^2/\lambda(v)v$ (e.g. Bian et al., 2014) and λ is the mean free path of an electron due to pitch angle scattering. For constant λ, velocity independence again requires $\alpha = 3$,

$$\delta_2 = \frac{1}{2}\left[4 + \left(16 + 4\frac{\lambda v_{\rm te}}{3\sigma^2}\tau_{\rm acc}\right)^{1/2}\right]. \tag{4.20}$$

Again, for comparison, the energy index of $\langle nVF(E)\rangle$ is needed and so, as before, but for the three-dimensional case, $\langle nVF(E)\rangle \sim v^2 f(v)/m_{\rm e}$ and,

$$\langle nVF(E)\rangle^{\rm 3d}_{\rm LT} \sim Ef(v) = Ev^{\delta_2} = E^{-\delta_2/2+1}, \tag{4.21}$$

where the superscript illustrates that this is the looptop spectrum for the three-dimensional Fokker-Planck.

So, the above arguments give the looptop spectral index predicted by the leaky-box Fokker-Planck solution, $\langle nVF(E)\rangle^{\rm 1d}_{\rm LT} \sim E^{-\delta_1/2}$ or $\langle nVF(E)\rangle^{\rm 3d}_{\rm LT} \sim E^{-\delta_2/2+1}$, depending on whether there is negligible or strong pitch-angle scattering respectively. In order to find the footpoint spectrum predicted in both cases, one needs the electron precipitation rate escaping from the looptop source, $\dot{N}(E)$ [e$^-$ s^{-1} per unit energy]. The number of particles per second per unit speed, $\dot{N}(v)$ [e$^-$ s^{-1} (cm s^{-1})$^{-1}$], is the flux multiplied by the volume, i.e.

$$\dot{N}(v) = \frac{\langle f\rangle_{\rm LT}}{\tau_{\rm esc}}V. \tag{4.22}$$

For the 1-dimensional Fokker-Planck the total number is $n_e = \int f dv$, this means that $\dot{N}(E)\ dE = \dot{N}(v)\ dv$ and so,

$$\dot{N}^{1\mathrm{d}}(E) = \frac{1}{m_e v}\frac{\langle f\rangle_{LT}}{\tau_{\mathrm{esc}}}V. \tag{4.23}$$

For the three-dimensional case the total number is $n_e = \int f 4\pi v^2 dv$, so $\dot{N}(E)\ dE = \dot{N}(v)\ 4\pi v^2 dv$ and,

$$\dot{N}^{3\mathrm{d}}(E) = \frac{4\pi v}{m_e}\frac{\langle f\rangle_{LT}}{\tau_{\mathrm{esc}}}V. \tag{4.24}$$

The density weighted mean electron flux at the footpoint is given by (see e.g. Kontar et al., 2011b),

$$\langle nVF(E)\rangle_{\mathrm{FP}} = \frac{E}{K}\int_E^\infty \dot{N}(E)dE. \tag{4.25}$$

For the scatter-free case this gives,

$$\langle nVF(E)\rangle_{\mathrm{FP}}^{1\mathrm{d}} = \frac{V}{m_e K\sigma}E\int_E^\infty \frac{1}{v}\langle f\rangle_{LT} v dE, \tag{4.26}$$

which means,

$$\langle nVF(E)\rangle_{\mathrm{FP}}^{1\mathrm{d}} \propto E\int_E^\infty E^{-\delta_1/2}dE \sim E^{-\delta_1/2+2}. \tag{4.27}$$

A similar argument leads to,

$$\langle nVF(E)\rangle_{\mathrm{FP}}^{3\mathrm{d}} \propto E^{-\delta_2/2+3}, \tag{4.28}$$

for the three-dimensional case.

In both cases the power-law spectral index depends on the value of τ_{acc}. If there was point like acceleration at the apex of the loop with this configuration, one might expect a spectral index close to δ_1 or δ_2 to form. However, the spatial non-uniformity of the acceleration region will result local acceleration times given by,

$$\tau_{\mathrm{eff}}(x) = \tau_{\mathrm{acc}}\exp\left(\frac{x^2}{2\sigma^2}\right), \tag{4.29}$$

due to x dependency of $D(x, v)$ (Equation 4.6), and hence a different local electron distribution function. Therefore, a spatially dependent acceleration region will create different spectral indices at each point in space. The resulting distribution function from the entire acceleration region is controlled by the transport between various spatial

locations. The resulting spectral index (if a power-law forms) could be different from that predicted by the leaky-box solution.

These results are compared to numerical simulations with spatially inhomogeneous acceleration and transport. They show the importance of including the spatial dependence clearly in Sections 4.4.1 and 4.4.2.

4.3 Solar Flare Parameters from RHESSI

In Chapter 2 the method for obtaining electron density, n_e, and acceleration region extent, σ, from a solar flare looptop source was discussed. For reference, the results are stated again here; a density of $n_e = 4.42 \times 10^{10}$ cm^{-3} was inferred within a coronal looptop with an acceleration region of spatial extent $\sigma = 5.3 \times 10^8$ cm. Allied to the temperature obtained directly from the thermal fit (T = 23 MK) and the fact that α has to equal 3 to enable comparison with the results of the forgoing section, this leaves one free parameter in the models (equations 4.1 and 4.2), the acceleration timescale, $\tau_{\rm acc}$.

4.4 Numerical Solutions of the Fokker-Planck Equation

A model corona with an originally Maxwellian distribution of particles at temperature, T, was created,

$$f = \sqrt{\frac{1}{2\pi v_{\rm te}^2}} \exp\left(-\frac{v^2}{2v_{\rm te}^2}\right). \tag{4.30}$$

The density, $n(x)$, increases exponentially at the chromosphere with scale height, $H =$ 220 km, following a hydrostatic model consistent with RHESSI observations (Battaglia & Kontar, 2012),

$$n(x) = \begin{cases} n_e; & -5'' \leq x < 15'' \\ n_{\rm final} \exp\left(-\frac{|x - x_{\rm max}|}{H}\right) + n_e; & 15'' \leq x \leq 20'' \end{cases}, \tag{4.31}$$

where $x_{\rm max}$ is the end of the numerical box (20″ in this case) and $n_{\rm final}$ is chosen so as the 'footpoint' resembles a thick-target. The density profile is shown in Figure 4.2. The acceleration is controlled by the term $D(v,x)$ (equation 4.6), into which the σ obtained from observations is substituted and α is set to 3 for the reasons discussed in Section 4.2.4. The parameter $\tau_{\rm acc}$ and how it affects the *mean* spectral index resulting from the simulations is examined. The mean index is used because of the fact that equations (4.1) and (4.2) will never produce a pure power-law. This is due to the extended, and spatially varying, nature of the acceleration region, there can be no balance between $\tau_{\rm acc}$ and $\tau_{\rm esc}$ as in the leaky-box formulation of Section 4.2.4. The simulated looptop and footpoint indices are compared to those predicted by the leaky-box solution (equations 4.18, 4.21, 4.27 and 4.28) valid for each transport regime to see how the introduction of a spatially varying, extended acceleration region affects the distribution of the energized particles. The timescales examined were $\tau_{\rm acc} = 10, 15, 20, 30, 40, 50, 100, 180, 270, 360, 540, 720, 900\ \tau_{\rm c}^{\rm th}$, where $\tau_{\rm c}^{\rm th} = v_{\rm te}^3/\Gamma$ is the collisional timescale of a thermal electron, approximately 0.01 s for the event in question ($\Gamma = 4\pi e^4 \ln\Lambda n_e/m_{\rm e}^2$ is the coronal collisional parameter here, independent of x). The Fokker-Planck equations were solved numerically by the method of finite differences (Kontar, 2001). The code itself is the same as that used in Chapter 3, the only difference being the introduction of spatial effects, and as such the tests discussed in Chapter 3 Section 3.5 still apply. The footpoint was tested by comparison to the thick-target model (Brown, 1971) and was found to agree with the analytic result within numerical errors. The results are discussed in the subsequent Sections, 4.4.1 and 4.4.2, but first the rest of this section will describe how to obtain $\langle nVF(E)\rangle$, and specifically the power law index, δ, from the simulations.

The electron velocity distribution, $f(v,x)$, used in the simulations is directly related to the observed mean flux spectrum, so that the electron flux spectrum is $F(E) = f(v)/m_{\rm e}$ [electrons cm^{-2} s^{-1} keV^{-1}] in the one-dimensional case and $F(E) = v^2 f(v)/m_{\rm e}$ for the three-dimensional velocity distribution of electrons. The density weighted mean

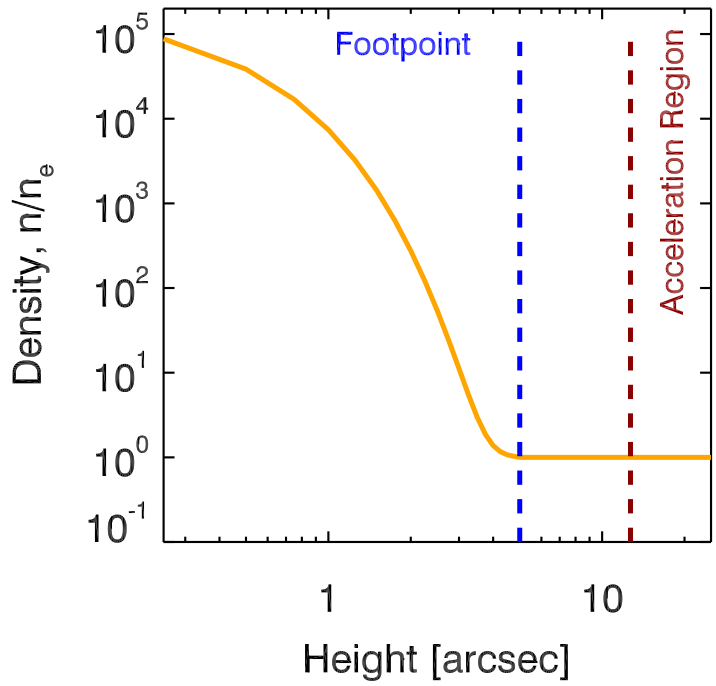

Figure 4.2: The density of the simulated corona, $n(x)/n_e$, as a function of height above the photosphere in arcseconds. With vertical lines showing the spatial extent of the acceleration region, σ, and the start of the footpoint.

electron flux is,

$$\langle nVF(E)\rangle = \int_V F(E,x)n(x)dV. \tag{4.32}$$

So,

$$\langle nVF(E)^{\mathrm{CS}}\rangle = A_{\mathrm{LT}}n_e \int_{-5''}^{15''} F(E,x)dx, \tag{4.33}$$

where A_{LT} is the cross-sectional area of the loop (found during the calculation of volume, V, in Chapter 2). The limits are the estimation of the distance from the maximum emission in $10-11.4$ keV to one of the footpoints, calculated from the CLEAN image (Figure 2.13). The footpoint has a steeply increasing density (Figure 4.2) over the last 5 arcseconds of the simulation domain and so the density weighted mean electron flux from the model footpoint is,

$$\langle nVF(E)^{\mathrm{FP}}\rangle = A_{\mathrm{LT}} \int_{15''}^{20''} F(E,x)n(x)dx. \tag{4.34}$$

The power-law index of either the simulated looptop or footpoint source can then be

found as,

$$\delta(E) = -\frac{d\ln\langle nVF(E)\rangle}{d\ln E}, \tag{4.35}$$

where the E dependence of δ is to make clear that the simulated spectral index *will not be* constant with E. The mean value of $\delta(E)$ for the energy range $20 - 100$ keV ($\sim$ average range fitted for non-thermal electrons in a RHESSI spectrum) for each $\tau_{\rm acc}$ will be compared to the equivalent leaky-box solution with differences highlighted.

4.4.1 Scatter-free Transport

Figure 4.3 shows the simulated density weighted mean electron flux, $\langle nVF(E)\rangle$. This graph clearly shows the dependence of both the spectral index, and non-thermal flux, on the acceleration timescale, $\tau_{\rm acc}$. The longer the acceleration timescale, the less particles are accelerated to non-thermal energies and the steeper the spectrum.

The simulated spectral index is shown in Figure 4.4. The fitted spectral index, with confidence bands, is overplotted for context and the leaky-box Fokker-Planck solution (equations 4.18 and 4.27) is shown by the blue diamonds. There is a clear difference between the spatially independent leaky-box solution and the spatially inhomogeneous model given by equation (4.1). For the looptop and footpoint sources both the numerical and leaky-box solutions display a similar behaviour with $\tau_{\rm acc}$ with the greatest difference between the two models at longer times. Furthermore, the spatially dependent model produces, for the most part, a softer spectral index for all acceleration timescales than that predicted by the leaky-box solution for both the footpoint and looptop sources. For the footpoint source the larger difference at short acceleration times ($\leq 200\tau_{\rm c}^{\rm th}$) can be considered non-physical due to the leaky-box solution predicting negative spectral indices here. This is a result of the simulated footpoint index 'saturating' at these short acceleration timescales, the reasoning for which is unclear (see discussion below).

The introduction of spatially inhomogeneous acceleration and transport therefore reduces the acceleration efficiency compared to the spatially independent leaky-box formulation. As a result, any acceleration timescale inferred from the latter could be an

overestimate of the actual acceleration timescale in the flare. As an example, consider the simulated looptop spectral index at $\tau_{\rm acc} = 360\tau_{\rm c}^{\rm th}$, this produces a δ that is closer in value to that predicted at $\tau_{\rm acc} = 720\tau_{\rm c}^{\rm th}$ by the leaky-box solution.

The spectral index difference, $\delta_{\rm LT} - \delta_{\rm FP}$, between the simulated looptop and footpoint sources is shown in Figure 4.5. Superficially, it appears that scatter-free transport can produce spectral indices less than 2, as observed often in solar flares. However, comparing with Figures 4.3 and 4.4 it is easy to see that this decrease in difference is somewhat artificial. It appears that for short acceleration timescales ($\leq 100\tau_{\rm c}^{\rm th}$) that the simulated model footpoint saturates, meaning that it will not produce negative spectral indices and as such while the analytic leaky-box Fokker-Planck formulation continues to get harder, the simulated footpoint spectrum becomes almost constant around zero. This has the effect of decreasing the spectral index difference but for timescales $\geq 200\tau_{\rm c}^{\rm th}$ the spectral index difference returns to around 2, which would be expected here, due to the model footpoint being designed as a thick-target (Brown, 1971). The 'saturation' can be thought of as a test for the validity of the footpoint in the code; there is no reason why the model (equation 4.1) should not produce negative indices. In fact, as the footpoint is designed as a thick-target the spectral index difference should remain 2. The reason why the code will not produce negative indices is unclear (the footpoint still stops the non-thermal particles here), but it is important to note that the spectral indices produced are unphysical in any case. As mentioned in Chapter 3, a standard value of γ for a coronal looptop source may be ~ 5 which for thin-target bremmstrahlung would require an electron spectrum with $\delta_{\rm LT} = 4$. The looptop spectral index is not above 4 until $\tau_{\rm acc} = 900\tau_{\rm c}^{\rm th}$ at which point the spectral index difference is ~ 2 again. Furthermore, footpoint indices are rarely observed with indices $\delta_{\rm FP} < 2$, which again the code doesn't predict until a similar acceleration time. The legitimacy of the footpoint in the code does not affect the analysis of the looptop spectrum either, which can be assumed valid across the domain. A study of longer acceleration times, and thus more realistic δ, will be undertaken in Stackhouse & Kontar (2017).

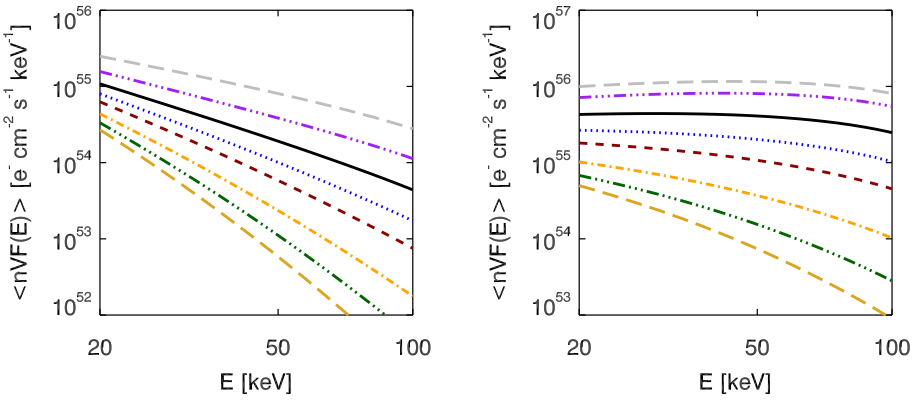

Figure 4.3: Simulated $\langle nVF(E)\rangle$ for the scatter-free transport case for coronal source (left) and footpoint source (right) for acceleration timescales: $\tau_{\rm acc} = 10\tau_{\rm c}^{\rm th}$ (grey dash line), $\tau_{\rm acc} = 100\tau_{\rm c}^{\rm th}$ (purple triple dot-dash line), $\tau_{\rm acc} = 180\tau_{\rm c}^{\rm th}$ (black solid line), $\tau_{\rm acc} = 270\tau_{\rm c}^{\rm th}$ (blue dot line), $\tau_{\rm acc} = 360\tau_{\rm c}^{\rm th}$ (maroon dash line), $\tau_{\rm acc} = 540\tau_{\rm c}^{\rm th}$ (orange dash-dot line), $\tau_{\rm acc} = 720\tau_{\rm c}^{\rm th}$ (green dash-triple dot line) and $\tau_{\rm acc} = 900\tau_{\rm c}^{\rm th}$ (yellow long dash line).

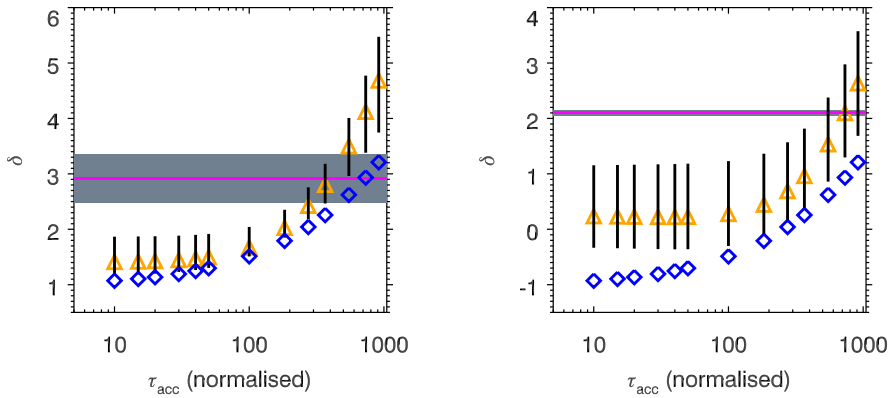

Figure 4.4: Simulated δ shown for looptop (left) and footpoint (right). The magenta line shows the observed $\delta^{\rm obs}$ with the grey confidence strip showing the possible range of $\delta^{\rm obs}$ for the fit ($\delta^{\rm obs}_{\rm LT} = 2.91 \pm 0.43$ and $\delta^{\rm obs}_{\rm FP} = 2.11 \pm 0.04$). Orange triangles are mean simulated δ for $20 - 100$ keV with error bars showing the maximum and minimum δ within that range. The blue diamonds show the predicted spectral index from the leaky-box approximation.

4.4.2 Diffusive Transport with $\lambda = 5 \times 10^8$ cm

Figure 4.6 shows the $\langle nVF(E)\rangle$ for diffusive transport with a constant mean free path. Like Figure 4.3 it is clear to see the relationship between the flux of non-thermal

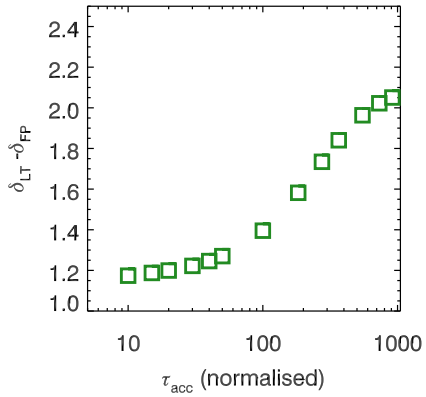

Figure 4.5: For the scatter-free transport case, mean simulated spectral index difference between the looptop and the footpoint across the energy range studied.

particles, the spectral index and the acceleration timescale.

The simulated spectral index is compared to that predicted from the leaky-box Fokker-Planck approximation (equations 4.21 and 4.28) and the imaging spectroscopy results from the 2011 February 24 flare in Figure 4.7. There is again a similar behaviour with both the spatially independent and inhomogeneous models with respect to the acceleration timescale. Concentrating solely on the looptop spectrum, as the leaky-box approximation to the footpoint (equation 4.28) predicts negative indices for all the timescales covered, while the numerical code again produces 'saturation' around zero across the domain, it is clear that the introduction of spatially inhomogeneous acceleration results in a softer spectral index than spatially independent acceleration and transport, with the largest discrepancy at longer times.

Again it is easily seen that using the spatially independent leaky-box Fokker-Planck approximation could result in the overestimation of the acceleration timescale when modelling stochastic acceleration in solar flares.

The simulated spectral index difference is shown in Figure 4.8. For the acceleration timescales studied the fact that this is less than 2 can be attributed to the same reason as the scatter-free transport case. The fact that the difference between the looptop and footpoint indices is not two can again be thought of as a validity check for the simulated footpoint spectrum.

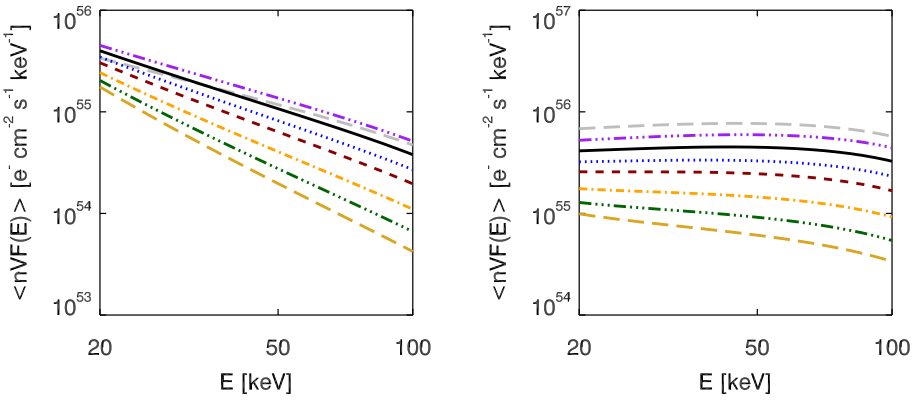

Figure 4.6: Same as Figure 4.3 but for diffusive transport with constant mean free path in velocity, $\lambda = 5 \times 10^8$ cm.

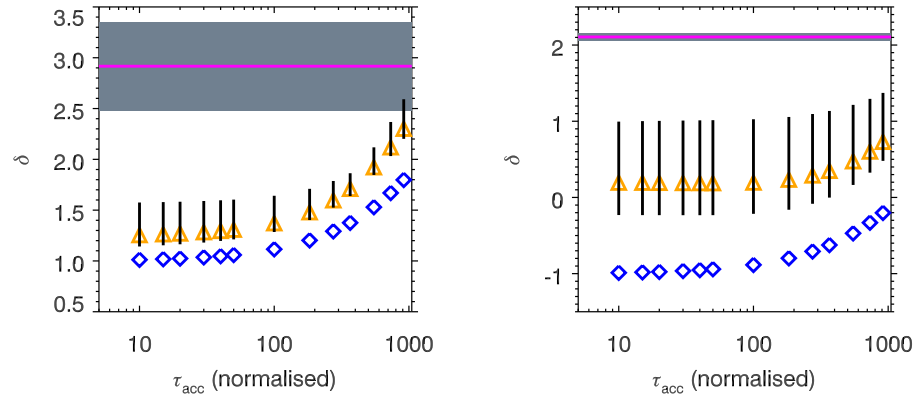

Figure 4.7: Same as Figure 4.4 but for diffusive transport with constant mean free path in velocity, $\lambda = 5 \times 10^8$ cm.

4.5 Conclusions

In this chapter a model accounting for the intrinsic spatial variation in solar flares (Xu et al., 2008; Kontar et al., 2011a; Guo et al., 2012) was studied. By using the imaging spectroscopy of the 2011 February 24 flare (Chapter 2) the density, temperature and spatial extent of the acceleration were inferred and used as input parameters to the model. This was solved numerically, and compared to the spatially invariant leaky-box approximation, commonly used when studying stochastic acceleration in solar flares. The results are summarized as follows:

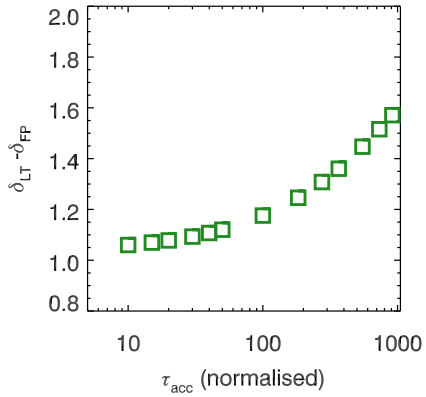

Figure 4.8: Same as Figure 4.5 but for diffusive transport with constant mean free path in velocity, $\lambda = 5 \times 10^8$ cm.

- *Scatter-free transport*; the introduction of a spatially inhomogeneous acceleration region while explicitly accounting for transport results in acceleration that is less efficient than the spatially independent leaky-box formulation. The resulting spectral index, for both looptop and footpoint sources, is softer than that when spatial effects are not taken into account.

- *Diffusive transport with* $\lambda = 5 \times 10^8$ *cm*; the same behaviour is seen for the diffusive transport case; the introduction of a spatially extended, inhomogeneous, acceleration region results in a softer spectrum than that predicted by the leaky-box solution.

Overall, for both transport regimes studied it is clear that the intrinsic spatial dependency evident in solar flares (Xu et al., 2008; Guo et al., 2012) changes the electron spectrum when compared to the spatially independent leaky-box Fokker-Planck approximation (Chen & Petrosian, 2013). It acts to reduce the acceleration efficiency and thus produces a softer spectrum. This means that the acceleration timescales inferred when using a leaky-box model applied to a solar flare may be an overestimation. These timescales can thus be considered an upper limit of the time taken to produce an observed spectral index. Thus, the intrinsic spatial dependence should be taken into account when modelling stochastic acceleration in solar flares.

In the next chapter, the work of this thesis is summarised and placed in the context of present and future work.

Chapter 5

Conclusions

The overarching theme of this thesis has been to examine the effects of acceleration and transport of electrons in solar flares and the resulting influence on the hard X-ray spectrum they produce. The work has been achieved by a mixture of analytical and numerical modelling, together with observations from RHESSI.

Chapter 2 introduced the two distinct flare morphologies that informed the models studied in the rest of the thesis. The first event studied was an example of what is known as a coronal thick-target source (Veronig & Brown, 2004; Jeffrey & Kontar, 2013) where the ambient density of the loop is high enough that electrons are collisionally stopped in the corona before they precipitate to the chromosphere. Sources such as these are very interesting in the sense that they enable detailed examination of the coronal source with minimal contamination from the footpoints. Studies of the spatial properties of these HXR events (Xu et al., 2008; Guo et al., 2012) has shown that the increase in loop length with energy is consistent with an initial acceleration occurring in an extended region within the loop plus an additional length proportional to the photon energy squared. This extra length being due to the higher energy electrons moving further through the loop before being stopped. This extended region was the subject of the work in Chapter 4. Further to this increase in length, Kontar et al. (2011a) found that coronal thick-target loops exhibited an increase in width with energy as well. This

is harder to explain, due to the fact that particles should be tied to field lines. The authors, and another study by Bian et al. (2011), suggested that this increase in width was due to magnetic turbulence, which is a prerequisite of the stochastic acceleration studied in this thesis. The analysis of this flare focussed on it being an example of the scenario considered in Chapter 3, and furthermore, to show the capabilities of imaging spectroscopy with RHESSI. The looptop structure was split into five parts, to enable examination of the spectral changes with distance from the looptop. The results are consistent with the analysis of Jeffrey & Kontar (2013) with a constant density along the loop, and the trend toward slightly harder spectra with distance consistent with an extended acceleration region with a halo of escaping particles shown in Xu et al. (2008) and Guo et al. (2012). Most solar flares do not have just a coronal source however, displaying X-ray sources in both the corona and the chromosphere. Generally in these cases most of the hard X-ray emission comes from the footpoints, due to the enhanced density compared to the corona, with the looptop emission a combination of thermal, soft and hard X-ray emission depending on the precise properties of the loop. The 2011 February 24 flare (the work on which will be published in Stackhouse & Kontar 2017) was chosen due to it being a limb flare, and thus enabling easy selection of the looptop and footpoint sources. This flare was previously studied by Simões & Kontar (2013), where the electron rates at the looptop were found to be less than was required to explain the footpoint emission. In Kontar et al. (2014) they showed that this could be explained by introducing a turbulent mean free path, λ, in a diffusive transport regime, which was studied in Chapter 4. The fits to the looptop and footpoint spectra are consistent with those in Simões & Kontar (2013), and using a technique similar to that study the electron density, n_e, was obtained. Together with an estimate of acceleration region extent from the CLEAN image and the temperature from the fit, these were used as the starting parameters of the model in Chapter 4.

Coronal thick-target sources enable the examination of the acceleration region in solar flares, allowing the precise measurement of the density and length of the region (Xu

et al., 2008) and thus the specific acceleration rate (Emslie et al., 2008; Guo et al., 2013), a quantity that describes the efficiency of the acceleration process. In Chapter 3, and in Bian et al. (2014), a model was shown in which the stochastic acceleration, collisional stopping, thermalisation and hard X-ray emission are all included in a representation of a coronal thick-target source. With a specific choice of turbulent diffusion coefficient, $D_{\rm turb} = D_0/v$, the model was shown to admit a steady-state kappa distribution solution. Kappa distributions are interesting in a solar flare context due to the fact that they reproduce the observed spectral shape, thermal core and power-law tail (Holman et al., 2003), without the need for two separate populations of electrons or, possibly artificial, low energy cutoffs. They transition smoothly from a Maxwellian form at low energies to a power-law with index κ at high energies. Kappa distributions in solar flares have been discussed by Kašparová & Karlický (2009) and Oka et al. (2013) showing that for most flares the emission from a single kappa distribution cannot reproduce the whole spectrum. Kašparová & Karlický (2009) however, found that the thin-target emission from a kappa distribution of electrons could provide an adequate fit to some looptop sources. The difference between these models and the one studied in Chapter 3 is the immediate physical significance of the parameter $\kappa\,(=\tau_{\rm acc}/2\tau_{\rm c} = \Gamma/2D_0)$, meaning that the spectral index fitted could provide information on the relative strength of acceleration to collisions. It follows that a temporal hardening/softening of the photon distribution in solar flares could be accounted for by a decrease/increase in the acceleration timescale respectively. This has been discussed before by Benz (1977) and Grigis & Benz (2006) to explain the observed soft-hard-soft and soft-hard-harder behaviour of the X-ray spectrum in solar flares. The evolution of an originally thermal distribution of electrons to this final steady-state kappa distribution was studied. It was found that this takes the form of a wavefront in velocity space, with position $v_{\rm f}(t)$, meaning that the distribution approximates the final, asymptotic form at low energies first. Numerical simulations were performed to establish the validity of of these analytic approximations showing clearly the wavefront as expected, with a front position given by $v_{\rm f} \sim t^{1/3}$. Due to the slow convergence towards the final steady-state solution, the natural question was whether the electrons could be confined

long enough within the acceleration region for a kappa distribution to form. Solving the governing equations in the limit of small escape it was found that the model would still approximate a kappa distribution up to some critical escape velocity whereafter escape would dominate. The exact value of the escape velocity was shown to depend on the dimensionless ratio between the turbulent mean free path, λ, and the acceleration region spatial extent, σ. In the final section of Chapter 3 a model with a constant electric field and efficient pitch angle scattering was examined focussing on the requirements for a kappa distribution to form. The turbulent diffusion coefficient was found to depend on the square of the accelerating field, $D_0 \propto E_{||}^2$. As such, in this situation, the spectral index, κ, could reveal information about the accelerating electric field. The quality of the hard X-ray observations from RHESSI enables close examination of the underlying electron distribution producing the bremmstrahlung emission. Comparing the emission from the steady-state kappa electron distribution to the photon spectrum would reveal information about the acceleration region. Difference and agreement between the spectra allowing one to infer the length of the region and strength of the accelerating field. It would be possible, and useful, to integrate the steady-state kappa distribution solution into OSPEX (Schwartz et al., 2002) in order to undertake a systematic analysis of coronal thick-target sources. However, the lack of events with this specific morphology, especially since the launch of SDO/AIA for comparison images, means that a large scale study may be difficult with the present X-ray images. The advent of more spatially resolved X-ray imaging in future will hopefully allow the application of the model to such sources on a greater scale.

Of course, the application of a model which is spatially independent is only possible due to the fact that the electrons are accelerated and stopped in the same volume. In reality, solar flares are spatially inhomogeneous. As mentioned before, the observations of Xu et al. (2008) and Guo et al. (2012) showed that to be consistent with observations the acceleration region must be extended and within the loop. Current modelling, for example the leaky-box Fokker-Planck approximation, deals with trans-

port implicitly, via an escape timescale (Chen & Petrosian, 2013). This allows the examination of the acceleration term without complications arising from transport. Another simplifying approximation is to inject an already accelerated distribution and study transport effects (e.g. Petrosian & Donaghy, 1999), but this does not account for the effects of acceleration on transport. Evidently such a split between acceleration and transport is not justified in light of these recent observations. In Chapter 4, and Stackhouse & Kontar (2017), a model which introduces an inhomogeneous extended acceleration region and explicitly accounts for the effects on acceleration and transport was presented. Two transport regimes were studied: scatter-free, where the particles experience no pitch-angle scattering, and diffusive transport, with a turbulent mean free path $\lambda = 5 \times 10^8$ cm accounting for the effects of pitch-angle diffusion. The spatially dependent diffusion coefficient was chosen to have a gaussian profile in space, with spatial extent σ found as in Chapter 2. This was due to the structure noted in Xu et al. (2008) and Jeffrey & Kontar (2013) of a core acceleration region surrounded by a halo of escaping particles. The governing equations were solved numerically by the method of finite differences and the spectral index obtained was compared to that found from the spatially independent leaky-box solution to the same model. For scatter-free transport there was a clear difference in the spectral index obtained. Explicitly accounting for the spatial effects on acceleration and transport resulted in a spectral index that was softer than that produced by the spatially independent leaky-box solution. That is to say that the introduction of a spatially inhomogeneous acceleration region resulted in the less efficient acceleration of electrons. This could result in the acceleration timescales found via the leaky box model (e.g. Chen & Petrosian, 2013) being an overestimation of the actual acceleration time required to produce the observed spectral index. For the diffusive transport case the same behaviour was found, taking account of the spatial effects explicitly resulted in a softer spectral index than the leaky-box solution. Therefore, in both cases, the introduction of a spatially dependent, extended acceleration region while accounting for the effects of this on acceleration and transport explicitly results in a less efficient acceleration than that in the spatially independent leaky-box solution. As such, an acceleration timescale obtained via the leaky-box method should

be considered an upper limit of the timescale actually required to produce the observed spectrum. It is suggested that the intrinsic spatial dependencies of solar flares are taken into account explicitly in future modelling. Further to the simulations shown here, it is intended that another scenario of interest will be examined in future; the case where the turbulent mean free path is velocity dependent, as mentioned briefly in Chapter 4. This would affect the α (velocity dependence of the diffusion coefficient) required by the leaky-box solution and the simulations would need to be re-run for the new $D(v, x)$. It would seem logical for some form of velocity dependence to exist in reality.

It is important to note that the numerical simulations in Chapters 3 and 4 do not account for all the effects on the electron distribution in a flare. In particular, there is no feedback to the surrounding plasma, such as an increase in temperature as the particles lose energy during collisions. There is also no creation of langmuir waves as the electrons move through the plasma. However, the code could relatively easily be updated to include these effects, and any others a user might want to add to the governing Fokker-Planck. In the interests of transparency, a copy of the finite difference code used is included in the Appendix A.

All of the work presented in this thesis has been driven by the excellent imaging spectroscopy of RHESSI. However, as mentioned, there is a paucity of observations of certain types of flares, such as coronal thick-targets. The next generation of solar instruments such as Solar Orbiter (mission: http://sci.esa.int/solar-orbiter/, instruments: http://sci.esa.int/solar-orbiter/51217-instruments/) and Solar Probe Plus (mission: http://solarprobe.gsfc.nasa.gov/ instruments: http://solarprobe.jhuapl.edu/spacecraft/instruments.php) will observe solar flares from closer to the Sun than ever before. Of particular interest will be the observations of in-situ energetic particles and magnetic fields at a distance of $\sim 3R_{\odot}$ by Solar Probe Plus, which will provide information on the acceleration mechanisms present in the corona. The X-ray spectrometer (STIX) onboard Solar Orbiter will provide detailed

spectral, temporal and spatial information on solar flares. It is hoped that better spatial resolution of X-ray imaging will be achieved and that it will provide new insight. Specifically, it will help to constrain the parameters of the acceleration region, and also shed light on the structure within it. Moreover, it is hoped that the work of this thesis can help the development of future solar X-ray imagers, as well as the analysis of the data obtained by them.

Bibliography

Anastasiadis, A. 2002, Journal of Atmospheric and Solar-Terrestrial Physics, 64, 481

Anastasiadis, A., & Vlahos, L. 1991, Astronomy and Astrophysics, 245, 271

—. 1994, Astrophysical Journal, 428, 819

Antonucci, E., & Dennis, B. R. 1983, Solar Physics, 86, 67

Antonucci, E., Gabriel, A. H., Acton, L. W., et al. 1982, Solar Physics, 78, 107

Aschwanden, M. 1996, in Astronomical Society of the Pacific Conference Series, Vol. 111, Astronomical Society of the Pacific Conference Series, ed. R. D. Bentley & J. T. Mariska, 216–221

Aschwanden, M. J. 2002, Space Science Reviews, 101, 1

—. 2004, Physics of the Solar Corona. An Introduction (Praxis Publishing Ltd)

Bai, T. 1982, Astrophysical Journal, 259, 341

Bai, T., Hudson, H. S., Pelling, R. M., et al. 1983, Astrophysical Journal, 267, 433

Bai, T., & Ramaty, R. 1978, Astrophysical Journal, 219, 705

Battaglia, M., & Benz, A. O. 2006, Astronomy and Astrophysics, 456, 751

—. 2007, Astronomy and Astrophysics, 466, 713

Battaglia, M., & Kontar, E. P. 2012, Astrophysical Journal, 760, 142

—. 2013, Astrophysical Journal, 779, 107

Benka, S. G., & Holman, G. D. 1994, Astrophysical Journal, 435, 469

Benz, A. O. 1977, Astrophysical Journal, 211, 270

Benz, A. O., & Smith, D. F. 1987, Solar Physics, 107, 299

Bian, N., Emslie, A. G., & Kontar, E. P. 2012, Astrophysical Journal, 754, 103

Bian, N. H., & Browning, P. K. 2008, Astrophysical Journal, Letters, 687, L111

Bian, N. H., Emslie, A. G., Stackhouse, D. J., & Kontar, E. P. 2014, Astrophysical Journal, 796, 142

Bian, N. H., Kontar, E. P., & MacKinnon, A. L. 2011, Astronomy and Astrophysics, 535, A18

Brown, J. C. 1971, Solar Physics, 18, 489

Brown, J. C., Aschwanden, M. J., & Kontar, E. P. 2002, Solar Physics, 210, 373

Brown, J. C., & Emslie, A. G. 1988, Astrophysical Journal, 331, 554

Brown, J. C., Emslie, A. G., Holman, G. D., et al. 2006, Astrophysical Journal, 643, 523

Brown, J. C., Emslie, A. G., & Kontar, E. P. 2003, Astrophysical Journal, Letters, 595, L115

Brown, J. C., & Hoyng, P. 1975, Astrophysical Journal, 200, 734

Brown, J. C., & Melrose, D. B. 1977, Solar Physics, 52, 117

Cargill, P. J. 1991, Astrophysical Journal, 376, 771

Cargill, P. J., Goodrich, C. C., & Vlahos, L. 1988, Astronomy and Astrophysics, 189, 254

Cargill, P. J., Vlahos, L., Baumann, G., Drake, J. F., & Nordlund, Å. 2012, Space Science Reviews, 173, 223

Chavanis, P.-H., & Lemou, M. 2005, Physical Review E, 72, 061106

Chen, Q., & Petrosian, V. 2013, Astrophysical Journal, 777, 33

Chernov, N., & Dolgopyat, D. 2007, Physical Review Letters, 99, 030601

Dalla, S., & Browning, P. K. 2005, Astronomy and Astrophysics, 436, 1103

—. 2006, Astrophysical Journal, Letters, 640, L99

—. 2008, Astronomy and Astrophysics, 491, 289

Decker, R. B. 1988, Space Science Reviews, 48, 195

Decker, R. B., & Vlahos, L. 1986, Astrophysical Journal, 306, 710

Del Zanna, G., Dere, K. P., Young, P. R., Landi, E., & Mason, H. E. 2015, Astronomy and Astrophysics, 582, A56

Dennis, B. R., & Pernak, R. L. 2009, Astrophysical Journal, 698, 2131

Dere, K. P., Landi, E., Mason, H. E., Monsignori Fossi, B. C., & Young, P. R. 1997, Astronomy and Astrophysics, Supplement, 125, doi:10.1051/aas:1997368

Dickson, E. C. M., & Kontar, E. P. 2013, Solar Physics, 284, 405

Ellison, D. C., & Ramaty, R. 1985, Astrophysical Journal, 298, 400

Elwert, G. 1939, Annalen der Physik, 426, 178

Emslie, A. G. 1983, Solar Physics, 86, 133

Emslie, A. G., & Henoux, J.-C. 1995, Astrophysical Journal, 446, 371

Emslie, A. G., Hurford, G. J., Kontar, E. P., et al. 2008, in American Institute of Physics Conference Series, Vol. 1039, American Institute of Physics Conference Series, ed. G. Li, Q. Hu, O. Verkhoglyadova, G. P. Zank, R. P. Lin, & J. Luhmann, 3–10

Emslie, A. G., Kontar, E. P., Krucker, S., & Lin, R. P. 2003, Astrophysical Journal, Letters, 595, L107

Emslie, A. G., Dennis, B. R., Shih, A. Y., et al. 2012, Astrophysical Journal, 759, 71

Fermi, E. 1949, Physical Review, 75, 1169

Fleishman, G. D., Kontar, E. P., Nita, G. M., & Gary, D. E. 2011, Astrophysical Journal, Letters, 731, L19

Fleishman, G. D., & Toptygin, I. N. 2013, Monthly Notices of the Royal Astronomical Society, 429, 2515

Fletcher, L., Dennis, B. R., Hudson, H. S., et al. 2011, Space Science Reviews, 159, 19

Furth, H. P., Killeen, J., & Rosenbluth, M. N. 1963, Physics of Fluids, 6, 459

Galloway, R. K., Helander, P., & MacKinnon, A. L. 2006, Astrophysical Journal, 646, 615

Gary, G. A. 2001, Solar Physics, 203, 71

Gordovskyy, M., Browning, P. K., Kontar, E. P., & Bian, N. H. 2013, Solar Physics, 284, 489

Grigis, P. C., & Benz, A. O. 2006, Astronomy and Astrophysics, 458, 641

Guo, J., Emslie, A. G., Kontar, E. P., et al. 2012, Astronomy and Astrophysics, 543, A53

Guo, J., Emslie, A. G., & Piana, M. 2013, Astrophysical Journal, 766, 28

Guo, X., Sironi, L., & Narayan, R. 2014, Astrophysical Journal, 794, 153

Hamilton, R. J., & Petrosian, V. 1992, Astrophysical Journal, 398, 350

Hannah, I. G., Fletcher, L., & Hendry, M. A. 2002, in ESA Special Publication, Vol. 506, Solar Variability: From Core to Outer Frontiers, ed. A. Wilson, 295–298

Hannah, I. G., & Kontar, E. P. 2011, Astronomy and Astrophysics, 529, A109

Hannah, I. G., Grefenstette, B. W., Smith, D. M., et al. 2016, Astrophysical Journal, Letters, 820, L14

Harrison, F. A., Craig, W. W., Christensen, F. E., et al. 2013, Astrophysical Journal, 770, 103

Haug, E. 1997, Astronomy and Astrophysics, 326, 417

Högbom, J. A. 1974, Astronomy and Astrophysics, Supplement, 15, 417

Holman, G. D. 1985, Astrophysical Journal, 293, 584

Holman, G. D., & Pesses, M. E. 1983, Astrophysical Journal, 267, 837

Holman, G. D., Sui, L., Schwartz, R. A., & Emslie, A. G. 2003, Astrophysical Journal, Letters, 595, L97

Holman, G. D., Aschwanden, M. J., Aurass, H., et al. 2011, Space Science Reviews, 159, 107

Hoyng, P., Duijveman, A., Machado, M. E., et al. 1981, Astrophysical Journal, Letters, 246, L155

Hudson, H. S. 1972, Solar Physics, 24, 414

Hurford, G. J., Schmahl, E. J., Schwartz, R. A., et al. 2002, Solar Physics, 210, 61

Jeffrey, N. L. S. 2014, PhD thesis, University of Glasgow

Jeffrey, N. L. S., & Kontar, E. P. 2011, Astronomy and Astrophysics, 536, A93

—. 2013, Astrophysical Journal, 766, 75

Jeffrey, N. L. S., Kontar, E. P., Bian, N. H., & Emslie, A. G. 2014, Astrophysical Journal, 787, 86

Johns, C. M., & Lin, R. P. 1992, Solar Physics, 137, 121

Jokipii, J. R. 1966, Astrophysical Journal, 146, 480

Jones, F. C. 1994, Astrophysical Journal, Supplement, 90, 561

Kane, S. R., Hurley, K., McTiernan, J. M., et al. 1998, Astrophysical Journal, 500, 1003

Karney, C. F. F. 1986, Computer Physics Reports, 4, 183

Kašparová, J., & Karlický, M. 2009, Astronomy and Astrophysics, 497, L13

King, I. R. 1965, Astronomical Journal, 70, 376

Kliem, B. 1994, Astrophysical Journal, Supplement, 90, 719

Kliem, B., Karlický, M., & Benz, A. O. 2000, Astronomy and Astrophysics, 360, 715

Koch, H. W., & Motz, J. W. 1959, Reviews of Modern Physics, 31, 920

Kontar, E. P. 2001, Computer Physics Communications, 138, 222

Kontar, E. P., Bian, N. H., Emslie, A. G., & Vilmer, N. 2014, Astrophysical Journal, 780, 176

Kontar, E. P., & Brown, J. C. 2006, Astrophysical Journal, Letters, 653, L149

Kontar, E. P., Hannah, I. G., & Bian, N. H. 2011a, Astrophysical Journal, Letters, 730, L22

Kontar, E. P., MacKinnon, A. L., Schwartz, R. A., & Brown, J. C. 2006, Astronomy and Astrophysics, 446, 1157

Kontar, E. P., Piana, M., Massone, A. M., Emslie, A. G., & Brown, J. C. 2004, Solar Physics, 225, 293

Kontar, E. P., Brown, J. C., Emslie, A. G., et al. 2011b, Space Science Reviews, 159, 301

Korchak, A. A. 1967, Soviet Astronomy, 11, 258

Kosugi, T., Makishima, K., Murakami, T., et al. 1991, Solar Physics, 136, 17

Kretzschmar, M. 2011, Astronomy and Astrophysics, 530, A84

Krucker, S., & Battaglia, M. 2014, Astrophysical Journal, 780, 107

Krucker, S., Christe, S., Glesener, L., et al. 2014, Astrophysical Journal, Letters, 793, L32

Kruskal, M. D., & Bernstein, I. B. 1964, Physics of Fluids, 7, 407

LaRosa, T. N., Moore, R. L., Miller, J. A., & Shore, S. N. 1996, Astrophysical Journal, 467, 454

LaRosa, T. N., Moore, R. L., & Shore, S. N. 1994, Astrophysical Journal, 425, 856

Lemou, M., & Chavanis, P.-H. 2010, Physica A Statistical Mechanics and its Applications, 389, 1021

Leubner, M. P. 2004, Physics of Plasmas, 11, 1308

Li, Y. P., & Gan, W. Q. 2005, Astrophysical Journal, Letters, 629, L137

Lifshitz, E. M., & Pitaevskii, L. P. 1981, Physical kinetics

Lin, R. P. 1970, Solar Physics, 15, 453

—. 2006, Space Science Reviews, 124, 233

Lin, R. P., & Hudson, H. S. 1976, Solar Physics, 50, 153

Lin, R. P., & Schwartz, R. A. 1987, Astrophysical Journal, 312, 462

Lin, R. P., Schwartz, R. A., Pelling, R. M., & Hurley, K. C. 1981, Astrophysical Journal, Letters, 251, L109

Lin, R. P., Dennis, B. R., Hurford, G. J., et al. 2002, Solar Physics, 210, 3

Litvinenko, Y. E. 1996, Astrophysical Journal, 462, 997

Liu, R., Wang, H., & Alexander, D. 2009, Astrophysical Journal, 696, 121

Liu, W., Petrosian, V., Dennis, B. R., & Jiang, Y. W. 2008, Astrophysical Journal, 676, 704

Livadiotis, G., & McComas, D. J. 2009, Journal of Geophysical Research (Space Physics), 114, A11105

Longair, M. S. 1981, High energy astrophysics

MacDonald, W. M., Rosenbluth, M. N., & Chuck, W. 1957, Physical Review, 107, 350

Mann, G., Aurass, H., & Warmuth, A. 2006, Astronomy and Astrophysics, 454, 969

Massone, A. M., Emslie, A. G., Hurford, G. J., et al. 2009, Astrophysical Journal, 703, 2004

Masuda, S., Kosugi, T., Hara, H., Tsuneta, S., & Ogawara, Y. 1994, Nature, 371, 495

McTiernan, J. M., & Petrosian, V. 1990, Astrophysical Journal, 359, 524

Melrose, D. B. 1968, Astrophysics and Space Science, 2, 171

—. 1969, Astrophysics and Space Science, 4, 143

—. 1980a, Plasma astrophysics: Nonthermal processes in diffuse magnetized plasmas. Volume 1 - The emission, absorption and transfer of waves in plasmas

—. 1980b, Plasma astrophysics: Nonthermal processes in diffuse magnetized plasmas. Volume 2 - Astrophysical applications

Mertz, L. N., Nakano, G. H., & Kilner, J. R. 1986, Journal of the Optical Society of America A, 3, 2167

Metcalf, T. R., Hudson, H. S., Kosugi, T., Puetter, R. C., & Pina, R. K. 1996, Astrophysical Journal, 466, 585

Miller, J. A., Larosa, T. N., & Moore, R. L. 1996, Astrophysical Journal, 461, 445

Miller, J. A., & Reames, D. V. 1996, in American Institute of Physics Conference Series, Vol. 374, American Institute of Physics Conference Series, ed. R. Ramaty, N. Mandzhavidze, & X.-M. Hua, 450–460

Miller, J. A., Cargill, P. J., Emslie, A. G., et al. 1997, Journal of Geophysics Research, 102, 14631

Milligan, R. O., Gallagher, P. T., Mathioudakis, M., et al. 2006, Astrophysical Journal, Letters, 638, L117

Neupert, W. M. 1968, Astrophysical Journal, Letters, 153, L59

Oka, M., Ishikawa, S., Saint-Hilaire, P., Krucker, S., & Lin, R. P. 2013, Astrophysical Journal, 764, 6

Park, J., Workman, J. C., Blackman, E. G., Ren, C., & Siller, R. 2012, Physics of Plasmas, 19, 062904

Parker, E. N., & Tidman, D. A. 1958, Physical Review, 111, 1206

Parnell, C. E., & De Moortel, I. 2012, Philosophical Transactions of the Royal Society of London Series A, 370, 3217

Peterson, L. E., & Winckler, J. R. 1959, Journal of Geophysics Research, 64, 697

Petkaki, P., & MacKinnon, A. L. 1997, Solar Physics, 172, 279

—. 2007, Astronomy and Astrophysics, 472, 623

Petrosian, V. 2012, Space Science Reviews, 173, 535

Petrosian, V., & Chen, Q. 2010, Astrophysical Journal, Letters, 712, L131

Petrosian, V., & Donaghy, T. Q. 1999, Astrophysical Journal, 527, 945

Petrosian, V., Donaghy, T. Q., & McTiernan, J. M. 2002, Astrophysical Journal, 569, 459

Petrosian, V., Yan, H., & Lazarian, A. 2006, Astrophysical Journal, 644, 603

Phillips, K. J. H., & Dennis, B. R. 2012, Astrophysical Journal, 748, 52

Piana, M., Massone, A. M., Kontar, E. P., et al. 2003, Astrophysical Journal, Letters, 595, L127

Piasecki, J. 1981, Journal of Statistical Physics, 24, 45

Pina, R. K., & Puetter, R. C. 1993, Publications of the ASP, 105, 630

Priest, E., & Forbes, T. 2000, Magnetic Reconnection, 612

Priest, E. R. 1985, Reports on Progress in Physics, 48, 955

Priest, E. R., & Titov, V. S. 1996, Philosophical Transactions of the Royal Society of London Series A, 354, 2951

Pryadko, J. M., & Petrosian, V. 1997, Astrophysical Journal, 482, 774

Ramaty, R. 1979, in American Institute of Physics Conference Series, Vol. 56, Particle Acceleration Mechanisms in Astrophysics, ed. J. Arons, C. McKee, & C. Max, 135–154

Ramaty, R., Kozlovsky, B., & Lingenfelter, R. E. 1979, Astrophysical Journal, Supplement, 40, 487

Ratcliffe, H., Bian, N. H., & Kontar, E. P. 2012, Astrophysical Journal, 761, 176

Ryan, J. M., & Lee, M. A. 1991, Astrophysical Journal, 368, 316

Saint-Hilaire, P., Krucker, S., & Lin, R. P. 2008, Solar Physics, 250, 53

Sakao, T., Kosugi, T., Masuda, S., et al. 1996, Advances in Space Research, 17, doi:10.1016/0273-1177(95)00544-O

Schlickeiser, R. 1989, Astrophysical Journal, 336, 243

Schlickeiser, R., & Miller, J. A. 1998, Astrophysical Journal, 492, 352

Schmahl, E. J., Pernak, R. L., Hurford, G. J., Lee, J., & Bong, S. 2007, Solar Physics, 240, 241

Schwartz, R. A., Csillaghy, A., Tolbert, A. K., et al. 2002, Solar Physics, 210, 165

Simões, P. J. A., & Kontar, E. P. 2013, Astronomy and Astrophysics, 551, A135

Smith, D. M., Lin, R. P., Turin, P., et al. 2002, Solar Physics, 210, 33

Somov, B. V., & Kosugi, T. 1997, Astrophysical Journal, 485, 859

Spicer, D. S. 1977, Solar Physics, 53, 305

Stackhouse, D. J., & Kontar, E. P. 2017, In Prep

Stix, M. 2004, The sun : an introduction

Sturrock, P. A. 1966, Physical Review, 141, 186

Sui, L., & Holman, G. D. 2003, Astrophysical Journal, Letters, 596, L251

Sweet, P. A. 1969, Annual Review of Astronomy and Astrophysics, 7, 149

Takakura, T., Ohki, K., Shibuya, N., et al. 1971, Solar Physics, 16, 454

Tanaka, Y. 1983, Solar Physics, 86, 3

Taylor, G. I. 1922, Proceedings of the Royal Society of London Series A, 102, 180

Tsuneta, S. 1995, Publications of the ASJ, 47, 691

Tsuneta, S., & Naito, T. 1998, Astrophysical Journal, Letters, 495, L67

Tsytovich, V. N. 1966, Soviet Physics Uspekhi, 9, 370

van Beek, H. F., Hoyng, P., Lafleur, B., & Simnett, G. M. 1980, Solar Physics, 65, 39

Vandas, M., & Karlický, M. 2016, Astronomy and Astrophysics, 591, A127

Veronig, A. M., & Brown, J. C. 2004, Astrophysical Journal, Letters, 603, L117

Vilmer, N., MacKinnon, A. L., & Hurford, G. J. 2011, Space Science Reviews, 159, 167

Warmuth, A., Mann, G., & Aurass, H. 2007, Central European Astrophysical Bulletin, 31

—. 2009, Astronomy and Astrophysics, 494, 677

Wood, P., & Neukirch, T. 2005, Solar Physics, 226, 73

Woods, T. N., Kopp, G., & Chamberlin, P. C. 2006, Journal of Geophysical Research (Space Physics), 111, A10S14

Wu, C. S. 1984, Journal of Geophysics Research, 89, 8857

Xu, Y., Emslie, A. G., & Hurford, G. J. 2008, Astrophysical Journal, 673, 576

Zharkova, V. V., & Gordovskyy, M. 2005, Space Science Reviews, 121, 165

Zharkova, V. V., Arzner, K., Benz, A. O., et al. 2011, Space Science Reviews, 159, 357

Appendix A

Finite Difference Code for the Isotropic Fokker-Planck with Diffusive Transport

There is a problem with the repeatability of results in science in general, especially computational work done with code written from scratch. As such, the finite difference code for the isotropic Fokker-Planck with diffusive transport stated above in Chapter 4 equation (4.2) is included. It is also my intention to upload all the codes, including analysis files, used for this thesis onto an online repository https://github.com/duncanstackhouse/Physics that is open access.

First, the normalisation of equation (4.2) is described. This is needed so that the code does not have to deal with excessively large or small numbers which tends to cause problems. Thus, if anyone does wish to use the code below they can retrieve the actual values of the parameters.

The time, t, velocity, v, and space, x, are normalised as so,

$$\tilde{t} = \frac{t}{\tau_{\mathrm{c}}^{\mathrm{th}}} \quad ; \quad \tilde{v} = \frac{v}{v_{\mathrm{te}}} \quad ; \quad \tilde{x} = \frac{x}{d}, \tag{A.1}$$

where $\tau_{\mathrm{c}}^{\mathrm{th}}$ and v_{te} are as defined in the main text and $d = 7.25 \times 10^7$ cm (1 arcsecond). The electron phase space distribution is normalised as $\int \tilde{f} d^3\tilde{v} = 1$. Equation 4.2 then

becomes,

$$\frac{1}{\tau_{\rm c}^{\rm th}}\frac{\partial \tilde{f}}{\partial \tilde{t}} - \frac{\lambda v_{\rm te}}{3d^2}\tilde{v}\frac{\partial^2 \tilde{f}}{\partial \tilde{x}^2} = \frac{1}{\tilde{v}^2 v_{\rm te}^3}\frac{\partial}{\partial \tilde{v}}\left[\tilde{v}^2\frac{v_{\rm te}^4}{\tau_{\rm acc}}\tilde{v}^{\alpha}\,{\rm e}^{-x^2/2\sigma^2} + \frac{\tilde{\Gamma}(x)\Gamma v_{\rm te}^2}{\tilde{v}v_{\rm te}}\right]\frac{\partial \tilde{f}}{\partial \tilde{v}}\frac{1}{v_{\rm te}} + \frac{\tilde{\Gamma}(x)\Gamma}{\tilde{v}^2 v_{\rm te}^3}\frac{\partial \tilde{f}}{\partial \tilde{v}}, \tag{A.2}$$

having expressed $D_{\rm xx}$ and $D(v,x)$ explicitly and defined $\tilde{\Gamma}(x) = \Gamma(x)/\Gamma$, where $\Gamma = 4\pi e^4 \ln\Lambda n_e/m_{\rm e}^2$ is the coronal collisional parameter. This is further simplified by realising that $\tilde{\Gamma}(x) = n(x)/n_e = \tilde{n}(x)$. With some more manipulation this eventually becomes,

$$\frac{\partial \tilde{f}}{\partial \tilde{t}} - \frac{\lambda v_{\rm te}^4}{3\Gamma d^2}\tilde{v}\frac{\partial^2 \tilde{f}}{\partial \tilde{x}^2} = \frac{1}{\tilde{v}^2}\frac{\partial}{\partial \tilde{v}}\left[\tilde{v}^2\frac{\tilde{v}^{\alpha}}{\tau_{\rm acc}}\,{\rm e}^{-x^2/2\sigma^2} + \frac{\tilde{n}(x)}{\tilde{v}}\right]\frac{\partial \tilde{f}}{\partial \tilde{v}} + \frac{\tilde{n}(x)}{\tilde{v}^2}\frac{\partial \tilde{f}}{\partial \tilde{v}}. \tag{A.3}$$

The factor in front of the spatial term is dimensionless and is the parameter B below. This is the equation solved by the method of finite differences (Kontar, 2001) in the code.

```
pro best_idl_accel

;
; Name: best_idl_accel.pro
; Author: Duncan James Stackhouse
; Date: 11 Nov 2015
;
; Description: Explicit Finite difference code to solve the isotropic
;              Fokker-Planck with spatially dependent diffusion
;              coefficient and diffusive transport.
;

  ; Universal Constants
```

```
kb = 1.38d-16
; Boltzmann's constant, erg K^-1

kb_keV = 8.62d-8
; Boltzmann's constant, keV K^-1

m_e = 9.1d-28
; Electron mass, g

charge = 4.8d-10
; Electron charge, ergs

lnlambda = 20.
; coulomb logarithm, standard for solar flares

d_norm = 7.25d7
; Spatial normalisation, 1 arcsec (cm)

keV = 1.6d-9
; Conversion from keV to erg

scale_height = 2.2d7
; Density scaleheight for the footpoint, cm (Battaglia+Kontar 2012)

scaleheight = scale_height/d_norm
; Normalised for the code

mfp = 5.0d8
; Mean free path (cm), Kontar et. al. 2014
```

```
  norm_mfp = mfp/d_norm
  ; Normalised mean free path

  save, kb, kb_keV, m_e, charge, lnlambda, d_norm, $
  keV, scale_height, scaleheight, mfp, $
  filename='universal_parameters.sav'

; Parameters from Imaging, looptop values in ROI2, temperature
; density, and acceleration region extent, L, (see diffusion
; coefficient) can be input by hand if preferred.

  restore,'volumes.sav'
  restore,'fitting_params_bestfit.sav'
  restore,'densities.sav'

  Temp = kt2/kb_keV     ; Temp in kelvin, from kt in OSPEX
  n_cor = n_real[0]     ; Density in cm^-3

; Constants obtained from Image parameters

  vte=sqrt(kb*Temp/m_e)
  ; Thermal Velocity cm s^-1

  Gamma_cor = 4*!pi*charge*charge/m_e*charge*charge/$
              m_e*n_cor*lnlambda
  ; Collision parameter

  B = vte*vte*vte*vte/Gamma_cor*mfp/d_norm/d_norm/3.
  ; Constant in front of the spatial diffusion term
```

```
  Tau_c = vte*vte*vte/Gamma_cor
  ; Collisional time of a thermal electron

; Print the standard parameters to check

  print, ' vte = ',vte,' Gamma = ', Gamma_cor,' B = ',B
  print, ' Tau_c = ', Tau_c,' T = ', Temp
  print, ' n_cor = ', n_cor,' delta = ', delta
  print, ' mfp = ', norm_mfp

; Initialise time

  t=0.

; Number of velocity and space points

  nv = 51
  nx = 101

; Make velocity array and add a small amount so we don't divide
; by zero, v from 0-15vte as this gives more than enough
; coverage for the energy range of interest (20-100keV)

  v = dindgen(nv)*15./nv
  deltaV = v[1]-v[0]
  v = v+deltaV
  minv=v[0]
  maxv=v[nv-1]

; Make a 2d array for finite differencing, this
```

```
; is purely so we can use matrix operations and
; avoid for loops in finite differences

  vv = dblarr(nv,nx)
  for j=0,nx-1 do begin
     vv[*,j] = v
  end

; Make the x array, from -5 so acceleration region
; is fully accounted for.

  deltax = 0.25
  x = -5. + dindgen(nx)*deltax
  xmin=x[0]
  xmax=x[nx-1]

; Define our normalised density, ne=1

  fp_start = 15.
  ; We define the start of our footpoint at 15d

  n_final = 200000.
  ; Final density to make sure fp resembles thick-target

  n=dblarr(nx)+1.
  nn=dblarr(nv,nx)+1.
  n[where(x gt fp_start, /null)] = n_final$
  *exp(-abs(x[where(x gt fp_start, /null)]$
  -xmax)/scaleheight)+1.
  ; Density model from Battaglia + Kontar 2012
```

```
; A 2d array for finite differencing, same reason as v

  for i=0,nv-1 do begin
     nn[i,*] = n
  end


; We want an originally maxwellian distribution of particles
; in velocity space

  Finj = dblarr(nv,nx)
  for i = 0, nv-1 ,1 do begin
     for j=0, nx-1, 1 do begin
        Finj[i,j] = sqrt(1.0/2./!pi)$
                    *exp(-v[i]*v[i]/2.)
     endfor
  endfor

; Now we define our diffusive elements,
; acceleration and collisional

  alpha = 3.
  ; Turbulent diffusion velocity index

  L = L2/d_norm/2.35
  ; Spatial width of the acceleration region
  ; from I.S. but can define by hand if wanted

  tau_acc=10.
```

```
  ; Acceleration timescale

  DT = v^alpha/Tau_acc
  ; Turbulent diffusion coefficient, controls
  ; the strength of the acceleration

  D = dblarr(nv,nx)      ; Empty array for D

  for i = 0, nv-1, 1 do begin
    for j = 0, nx-1, 1 do begin
       D[i,j] = v[i]^2 * DT[i] $
       * exp(-abs(x[j]^2/(2. * L^2)))$
       + n[i]/v[i]
    endfor
  endfor
  ; Here we have joined turbulent and coll
  ; diffusion together to make finite difference
  ; easier.

; Save starting parameters for use in plotting

  save, x, v, vv, temp, n_cor, Finj, n, $
  vte, Gamma_cor, Tau_c, tau_acc, L, $
  alpha, filename='starting_parameters.sav'

; Set F to it's initial condition

  F = Finj
  Fnew = F
  ; service variable for finite differencing
```

```
; Set our final time

  t_final = 1000.

; Time to print the results and save counters

  tprint = 0.01
  lastprint = 0.0
  screenprint = 0.1
  timeprint = 0.0
  sav_file_counter=0

; stability condition for timestep

  deltaT = deltav * min(v)^2. /max(n)/1.1
  print, 'deltaT = ', deltaT
  ;print to check sensible

; Set up the Finite difference service variables

  v_sq_inv = 1./(v^2)
  vv_sq_inv = 1./(vv^2)
  dt_ov_dv = deltaT/deltaV
  dt_ov_dvsq = deltaT/deltav/deltav
  dt_ov_dxsq = deltaT/deltax/deltax


;;;;;;;;;;;;;;;;;;;;;;;;;;;;;;;;;;;;;;;;;;;;;;;;;;;;;;;;;;;;;;;;;;;;;;;;
;;;;;;;;;;;;;;;;;; FINITE DIFFERENCE LOOP  ;;;;;;;;;;;;;
```

```
;;;;;;;;;;;;;;;;;;;;;;;;;;;;;;;;;;;;;;;;;;;;;;;;;;;;;;;;;;

 while (t lt t_final) do begin



 Fdiff2=F
 ; the fact it’s called Fdiff2 is just a relic, could
 ; be called anything

 ; Velocity finite differencing, coulomb collisions
 ; and diffusive terms

     ; 1/v^2 d/dv(f)...

     Fdiff2[0:nv-2,*]=Fdiff2[0:nv-2,*] + dt_ov_dv * nn[0:nv-2,*] $
                     * ( Fdiff2[1:nv-1,*] - Fdiff2[0:nv-2,*])$
                     *vv_sq_inv[0:nv-2,*]

     ; 1/v^2 d/dv D df/dv

     Fdiff2[1:nv-2,*] = Fdiff2[1:nv-2,*] + dt_ov_dvsq * $
                         ( D[1:nv-2,*] * ( Fdiff2[2:nv-1,*] $
                         - Fdiff2[1:nv-2,*])-D[0:nv-3,*] * $
                         ( Fdiff2[1:nv-2,*] - Fdiff2[0:nv-3,*]))$
                         * vv_sq_inv[1:nv-2,*]

 ; Assimilate this before movement

     Fnew = Fdiff2
```

```
; Now for the spatial term

    Fnew[*,1:nx-2] = Fnew[*,1:nx-2]+B*vv[*,1:nx-2]*( F[*,2:nx-1]$
                   - 2*F[*,1:nx-2] + F[*,0:nx-3])*dt_ov_dxsq

; Boundary condition, keep LH boundary same through time

    Fnew[*,0] = Finj[*,0]
    Fnew[0,*] = Finj[0,*]
    F = Fnew

; Saving f and t, use your favourite plotting routine to check
; progress here...

    if((t-lastprint) ge tprint) then begin

        lastprint = 1.5*tprint*FLOOR(t/tprint)
        ; so we don't save every timestep, logarthmically to
        ; base 1.5

        print, 'next print = ', lastprint
        ;print to see when the next save is

        save, F, t, filename ='F_'+string(sav_file_counter, $
                format='(I5.5)')+'.sav'
        ;save the file

        print, 'counter @', sav_file_counter
        ; print save counter
```

```
            sav_file_counter = sav_file_counter+1
            ; update counter

        end

        if((t-timeprint) ge screenprint) then begin

            print, 't = ', t,' collisional times'
            timeprint = screenprint*FLOOR(t/screenprint)
            ;print at each value of screenprint to see time

        end

        t=t+deltaT

    end


end
```